Obscuration and X-ray Variability of Active Galactic Nuclei

James C. Manners

Doctor of Philosophy

The University of Edinburgh

2002

Obscuration and X-ray Variability of Active Galactic Nuclei

This thesis is my own composition except where indicated in the text.

December 11, 2002

Abstract

In this thesis I present a study of the properties of AGN populations based on X-ray surveys with ROSAT and Chandra.

I have studied the short timescale X-ray variability properties of a sample of 156 radio-quiet quasars taken from the ROSAT PSPC archive covering a redshift range $0.1 < z < 4.1$. I use a maximum likelihood method to constrain the amplitude of variability, and combine light curves in ensembles in order to identify correlations with luminosity and with redshift. Variability amplitude is found to be anti-correlated with luminosity for quasars out to redshifts of ~ 2, in good agreement with the relation found for local AGN ($z < 0.1$). There is tentative evidence for an increase in X-ray variability amplitude towards high redshifts ($z > 2$) in the sense that quasars of the same X-ray luminosity are more variable at $z > 2$. I have discussed possible explanations for this effect. The simplest explanation may be that high redshift quasars are accreting more efficiently than local AGN.

The spectral shape of the hard X-ray background may be produced by the cumulative emission of a large population of obscured AGN. Comastri *et al.* (1995) have predicted the ratios of objects with X-ray column densities necessary to provide a fit to the X-ray background. Using these ratios together with the observed broad band spectral energy distributions of quasars, I have estimated the characteristics such a population would exhibit from submillimetre to ultraviolet wavelengths. Predictions for the contribution of these obscured AGN to mid-infrared surveys are a good fit to the observed number counts of sources displaying both 15μm and X-ray emission.

Finally, I have analysed X-ray source properties and statistics in two deep Chandra observations of the ELAIS fields N1 & N2. I present a comprehensive source catalogue of 233 point sources. In addition, 2 extended sources are detected and found to be

associated with galaxy clusters. An overdensity of sources is found in region N1 with 30% more sources than N2. Number count relations reveal a greater fraction of hard spectrum sources towards fainter X-ray fluxes. The fraction of sources with galaxy-like optical counterparts similarly increases towards faint fluxes. A possible explanation is that obscuration is causing intrinsically bright, softer-spectrum AGN to appear as faint, hard X-ray sources with galaxy-like optical counterparts.

Acknowledgements

Thanks to Andy Lawrence and Omar Almaini (for the science), Ali, Michael, Lou and Olivia (for the encouragement), Maggie (for... never you mind), the crew of the Orion Star (for my life), my brother Rob (remember I am still a civilian and you do not salute me), Mum, Lorna and the lads (for putting your hands up), all my friends, especially Sam & Andy (for auld lang syne), UV, Nichola, Gwyn, Jo & Liz (for the craic) and most importantly my Dad who would have read it all.

Contents

List of Figures

List of Tables

Chapter 1

Introduction

This thesis aims to shed light on the nature of Active Galactic Nuclei (AGN) by studying their behaviour as a group. All AGN are not equal. They display a variety of properties that at first led them to be classified as separate astronomical phenomena. However, many of the differences may be due to the direction from which these objects are observed, their rate of fuelling and their stage of evolution (e.g. Dopita 1997). The extent to which these factors play a part is at present a matter of debate.

Emission from AGN is considered to be driven by accretion onto a supermassive black hole. The current paradigm describes an accretion disc composed of optically-thick plasma. A radial temperature gradient gives rise to thermal radiation from infrared through to ultra-violet wavelengths and perhaps even soft X-rays. In the inner regions, a hot optically-thin plasma in a corona surrounding the disc produces emission in the medium to hard X-ray band. Surrounding the core, fast moving gas clouds give rise to Doppler-broadened line emission. From certain viewpoints these are obscured by dust which thermally radiates in the infrared. Further out, slow moving gas ionised by the central source produces narrow emission lines. In a small minority of cases, highly relativistic bipolar outflows of energetic particles lead to extended radio emission.

This picture has been built up through the study of AGN in two ways. Firstly, by the

in-depth study of individual AGN in the local universe, and secondly, through studying statistical samples that cover a range of redshift and luminosity as well as other properties. AGN surveys are able to determine the relationships between the various properties of these objects and interpret their importance.

In this thesis I have used samples of AGN to observe short-timescale X-ray variability characteristics at the highest redshifts yet studied. Tentative evidence has emerged that AGN may behave differently at high redshift. This work can be found in chapter 2. In chapter 3 I have developed models to determine the impact of a large population of obscured AGN on the cosmic background emission. The shape of the X-ray background can be accounted for by the combined emission of a population of AGN whose soft X-ray flux has been attenuated by columns of gas. These objects may not previously have been identified as AGN if their optical emission is also obscured by dust. The existence of these hard X-ray sources is now coming to light with the recent deep surveys of Chandra and XMM. In chapters 4 & 5 I detail my work on the ELAIS Deep X-ray Survey. This involves the identification of X-ray sources in deep Chandra images, compilation of the source catalogue, and an analysis of the statistical properties of the sources. The Chandra data also allows some comparisons with the theoretical models described in chapter 3.

To begin, I will give a brief background into the aspects of AGN that are covered in this thesis, namely, the characteristics of AGN continuum spectra, the nature of obscuration, and the properties of AGN X-ray variability.

1.1 AGN continuum spectra

AGN exhibit significant emission in nearly all wavebands studied to date. Their spectra span hard X-rays to the far infrared with almost equal power per decade of frequency. Closer inspection reveals a number of features such as dips and bumps that consistently recur from one AGN to the next. These features are illustrated in figure 1.1 which is loosely based on the mean spectrum of a sample of predominantly 'UV excess' selected

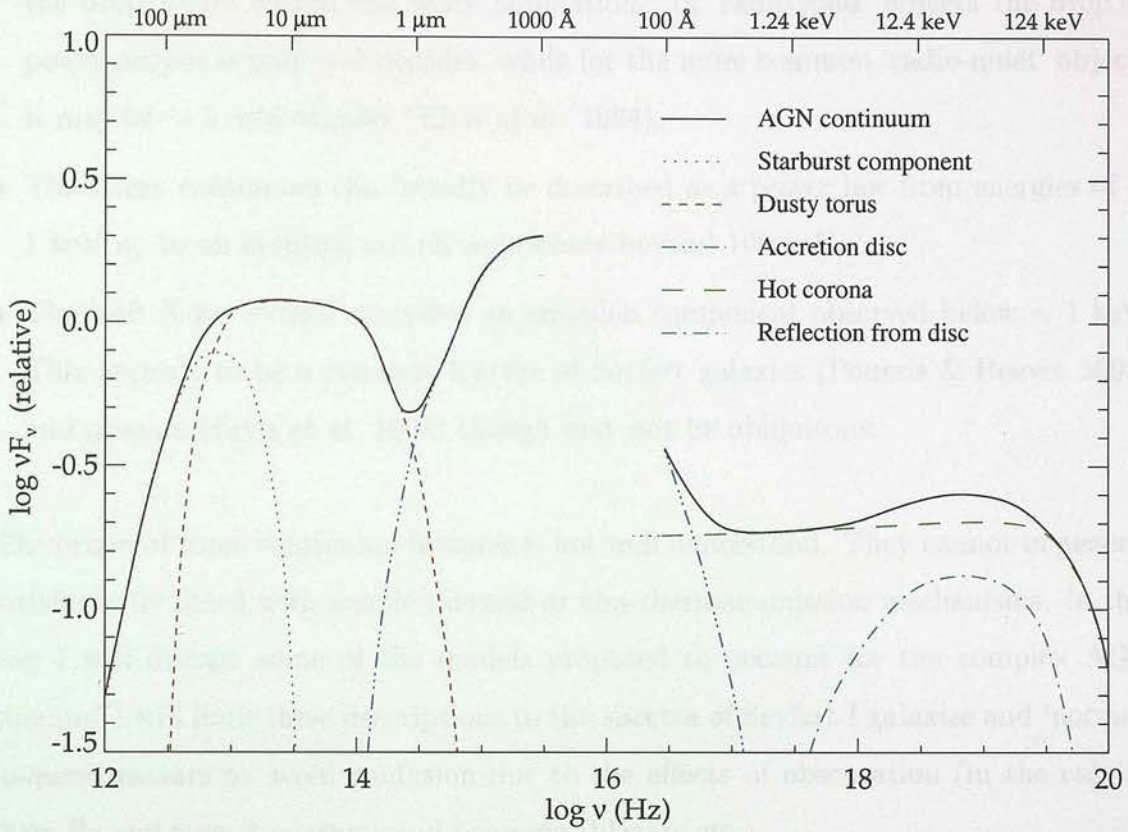

Figure 1.1: Schematic representation of an AGN continuum spectrum including a possible source for each emission component.

quasars from Elvis *et al.* (1994). The most notable features include the following:

- The 'big blue bump' covers the wavelength range from $\sim$ 4000 Å to at least 1000 Å. Whether this feature extends further into the EUV is unclear. Our galaxy becomes virtually opaque at wavelengths between 912 Å and $\sim$ 100 Å due to absorption by neutral hydrogen.
- The 'near-infrared inflection' appears as a dip between 1 μm and 1.5 μm. This is practically the only continuum feature with a well defined wavelength (Neugebauer *et al.* 1987).
- The 'infrared bump' is a broad feature longward of the 1 μm inflection.
- The 'submillimetre break' marks a sharp drop in emission and is the strongest feature seen in normal quasar continua. The exact location of this feature and the size of

the drop varies within the AGN population. In 'radio-loud' objects the drop in power output is only $\sim$ 2 decades, while for the more common 'radio-quiet' objects it may be $\sim$ 5 or 6 decades (Elvis *et al.* 1994).

- The X-ray continuum can broadly be described as a power law from energies of $\sim$ 1 keV up to an eventual cut-off somewhere beyond 100 keV.
- The 'soft X-ray excess' describes an emission component observed below $\sim$ 1 keV. This appears to be a common feature of Seyfert galaxies (Pounds & Reeves 2002) and quasars (Elvis *et al.* 1994) though may not be ubiquitous.

The origin of these continuum features is not well understood. They cannot in general be satisfactorily fitted with simple thermal or non-thermal emission mechanisms. In this section I will discuss some of the models proposed to account for the complex AGN continuum. I will limit these descriptions to the spectra of Seyfert I galaxies and 'normal' radio-quiet quasars to avoid confusion due to the effects of obscuration (in the case of Seyferts IIs and type 2 quasars) and beaming (blazars etc.).

1.1.1 X-ray spectra

To first order, the X-ray spectra of AGN are power laws of the form $S_\nu \propto \nu^{-\alpha}$ with $\alpha \sim 0.7$, modified by photoelectric absorption at soft energies (Mushotzky 1980, Halpern 1982, Rothschild *et al.* 1983). ROSAT and Ginga, sensitive in the ranges 0.1 - 2 and 2 - 30 keV respectively, revealed a more complicated structure with a softer underlying power law of $\alpha \sim 0.9$. Superimposed on this continuum are a number of features illustrated in figure 1.2. A strong emission line is seen at a rest frame energy of $\sim$ 6.4 keV (e.g. Pounds *et al.* 1990). This is interpreted as fluorescent Fe K emission, but with an equivalent width too great to be the result of absorbing material in the line of sight (Makishima 1986). The spectra are seen to harden beyond this feature to form a bump peaking at $\sim$ 30 keV. This can be explained by a reprocessing (Compton scattering or 'reflection') of the X-ray power law within optically thick material (e.g. George & Fabian 1991). The

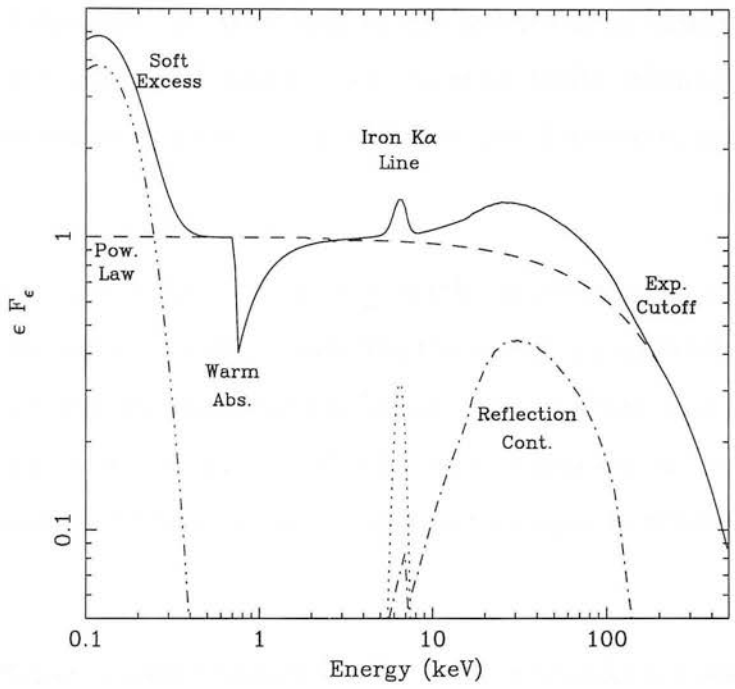

Figure 1.2: Schematic diagram displaying the key features of a Seyfert 1 X-ray spectrum (from Fabian 1998b).

intensity of this component is consistent with the reflector subtending a solid angle of 2π (Nandra *et al.* 1991), most likely the accretion disc itself. Photoelectric absorption by elements within the disc result in Compton reflection only becoming dominant beyond the absorption edge of iron. Beyond the peak at $\sim$ 30 keV the spectrum steepens due to the effects of energy loss to electron recoil and reduction in the scattering cross-section.

At soft X-ray energies, the power law continuum is often absorbed by ionised material in the line of sight. This is known as the 'warm absorber' and is generally characterised by the K-shell absorption edges of ionised oxygen which fall within the ROSAT and ASCA bandpasses. Absorption by cold material is also seen in some objects although these are usually classified as obscured AGN (see section 1.2). Photoelectric absorption may often mask the presence of the 'soft excess'. Identification of this feature is also hampered by its position at the bottom of the bandpass for most X-ray telescopes. However, recent XMM-Newton spectra of a sample of 6 Seyfert I galaxies reveals an excess soft emission component in each case (Pounds & Reeves 2002).

A final important aspect of AGN high energy spectra is an exponential cut-off at $\sim$ 200 keV (e.g. Seyfert I galaxy IC 4329a, Madejski *et al.* 1995). Although the exact energy of this cut-off is uncertain, no radio-quiet AGN has been detected beyond several hundred keV.

Models for the X-ray spectra of AGN generally attempt to explain the underlying power law and high energy cut-off, considering the remaining spectral features to be due to the effects of reprocessing. The majority ascribe the power law to the inverse Compton scattering of soft photons in a bath of 'hot' electrons. Variations in this model depend on the energy distribution of these electrons and their location in relation to the accretion disc.

In the 'non-thermal' model (Zdziarski *et al.* 1990, Zdziarski & Coppi 1991), electrons are accelerated to relativistic energies, perhaps due to magnetic reconnection events. Collisions with photons and other electrons cause a 'pair cascade' which then Comptonise UV and optical photons from the disc. The pairs then thermalise to temperatures of a few keV resulting in further upscattering of UV photons to form the soft excess. A major problem with this model is that the pairs should eventually annihilate to produce a strong emission line at 511 keV. This line has never been observed. It is therefore thought likely that the scattering electrons have a thermal ('Maxwellian') energy distribution. This would predict a high energy cut-off (E_c) at $E_c/1.6 \simeq kT_{plasma}$ for a Comptonising plasma at temperature T_{plasma} (e.g. Pietrini & Krolik 1995).

The geometry of this Comptonising plasma remains uncertain. A simple 'sandwich' model describes a cool, optically thick accretion disc covered by a hot optically thin layer (e.g. Maraschi & Haardt 1996). A certain fraction (f) of the gravitational energy is dissipated in the hot corona, with the remainder (1-f) dissipated in the disc. Isotropic Comptonisation results in half the emission escaping directly from the corona. Of the half which impinges on the disc, 10 - 20% is reflected to produce the Compton reflection bump and the Fe K fluorescence line. The remaining 80 - 90% is photoelectrically absorbed and eventually reemitted as thermal radiation in the 'big blue bump'.

Problems with this model geometry arise on attempting to fit the slope of the X-ray spectra. It is found the fraction, f, needs to be $\simeq 1$ or too many soft 'seed' photons will be produced. This would require the entire optical-UV bump to be reprocessed emission. In reality UV luminosities appear to be larger than bolometrically corrected X-ray luminosities for Seyfert galaxies (Walter & Fink 1993). An alternative geometry consists of the 'patchy corona' model. Here the magnetic field releases energy into the corona in discrete active, or flaring regions (Galeev, Rosner & Vaiana 1979). In these regions $f \simeq 1$ while elsewhere on the disc $f \simeq 0$ and the primary UV emission is relatively unimpeded. This model is supported by observations of continuum variability. The reprocessed contribution to the UV bump would be expected to vary simultaneously with the X-ray, while the primary thermal disc emission would vary much more slowly. Variations in the optical-UV and medium X-ray on timescales of weeks to months, have been observed to be well correlated in a number of AGN (NGC 4151: Warwick *et al.* 1996, NGC 5548: Tagliaferri *et al.* 1996). The UV and X-ray variations are, however, not perfectly correlated as required by the 'sandwich' model geometry.

These models still do not explain the source of the soft X-ray excess. The emission process is poorly constrained due to the large gap in the data between the UV and soft X-ray. An early candidate was the tail end of a multi-temperature thermal accretion disc spectrum, the cool end of which is the 'big blue bump'. However this requires an extremely high temperature which appears unlikely, even for the inner edge of the disc. In the case of NGC 5548 at least, the soft excess requires an entirely separate spectral component in order to fit the data (Magdziarz *et al.* 1998). Other models include blended soft X-ray line emission (e.g. Turner *et al.* 1991), or reprocessed Comptonised emission from the surface layers of the disc. However, none of these models is completely satisfactory. In particular, recent evidence that variations in the soft excess may *lead* variations in the medium X-ray band (Chiang *et al.* 2000) causes major problems for the reprocessing scenario.

A feature of AGN X-ray spectra that appears to manifest well beyond the accretion disc is the signature of the 'warm absorber'. Absorption edges of O VII at 739 eV and O VIII at 870 eV are found in at least half of all Seyfert Is and a few quasars (Mathur

et al. 1994). In the same objects, UV and optical absorption features are also typically found although the warm absorber has a higher ionisation state (Crenshaw *et al.* 1999). In all cases, absorption features are blue shifted indicating an outflow of material. For the X-ray absorption lines typical velocities are hundreds to several thousand km s^{-1} (e.g. Kaastra *et al.* 2000, Kaspi *et al.* 2001, Collinge *et al.* 2001), considerably slower than the broad-line region clouds. The warm absorber is thought to be an ionised wind, (perhaps evaporated off the inner edge of a dusty torus, Krolik & Kriss 2001) which may also be responsible for scattering the nuclear light in obscured AGN.

1.1.2 Optical - UV continuum

Dominating the optical - UV spectra of AGN is the broad continuum feature known as the 'big blue bump'. The exact shape of this feature is confused by a large number of broad and blended lines thought to be emitted from fast moving ionised clouds near the centre of the AGN. In particular, superimposed on the continuum between $\sim$ 2000 Å and 4000 Å is a feature known as the 'small blue bump', made up of the Balmer continuum and blended Balmer and Fe II line emission. Figure 1.3 displays these features in a composite quasar spectrum. At wavelengths redward of Lyα the composite uses quasars from the Sloan Digital Sky Survey selected on the basis of their optical colours (Vanden Berk *et al.* 2001). The slope of the optical continuum generally varies between $\alpha_\nu \sim -1$ to 0, from AGN to AGN. For this sample the median slope is $\alpha_\nu = -0.46$. The continuum blueward of the Lyman edge is rarely observed. However Zheng *et al.* (1997), compiled a spectrum from a sample of redshift $\sim$ 1 quasars with relatively low line-of-sight column densities for intergalactic absorption. The composite HST/FOS spectrum is displayed blueward of Lyα in figure 1.3. There appears to be a break in the continuum slope at $\sim$ 1050 Å with $\alpha_\nu \sim -1.8$ in the far ultra-violet. It should be noted that there are a number of difficulties in measuring the true spectral slope in optical-UV data due to absorption and emission in intervening material. Host galaxy contamination can play a major role in low luminosity AGN, especially in the case of a nuclear starburst that can rarely be

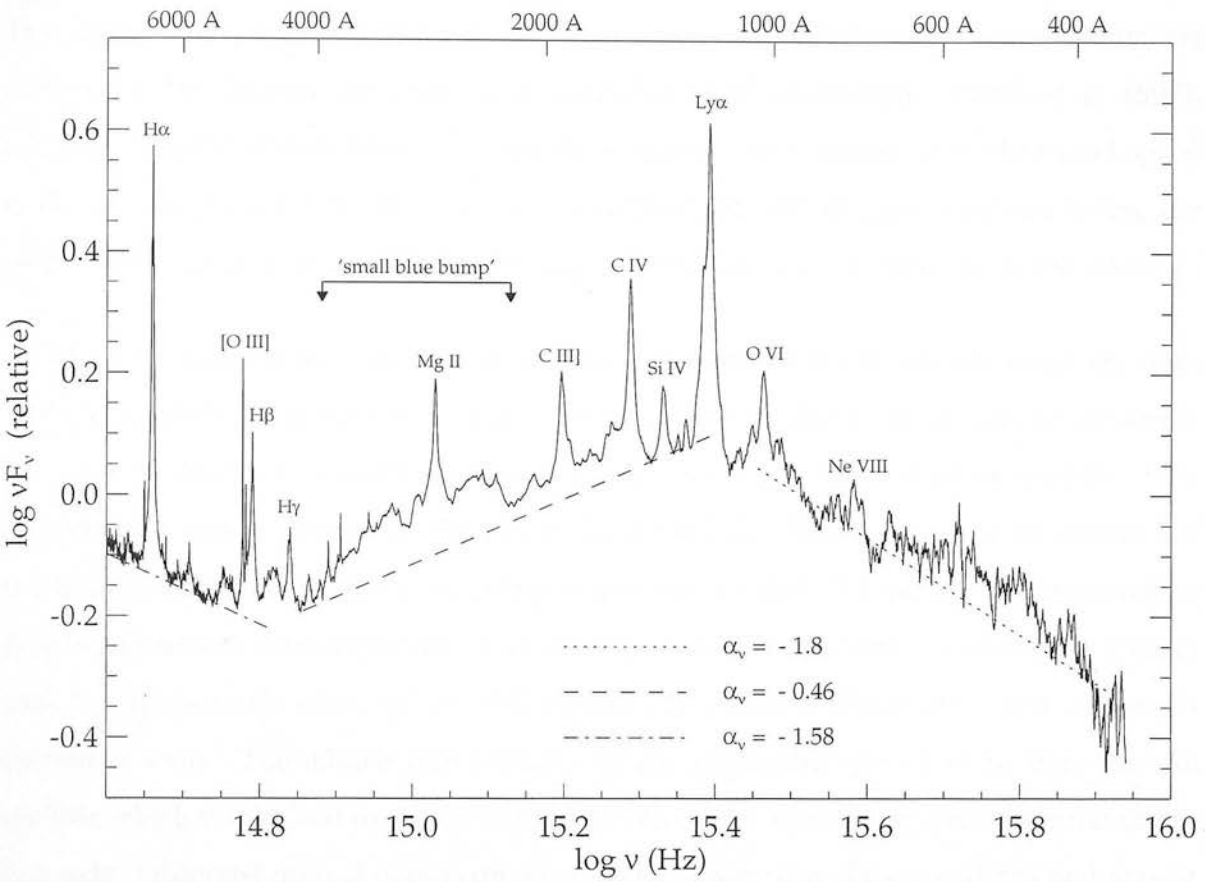

Figure 1.3: Optical - UV composite quasar spectrum. Longward of Lyα, data is compiled from $\sim$ 2200 quasars from the Sloan Digital Sky Survey (Vanden Berk *et al.* 2001). The change in slope at 5000 Å may be partly due to host-galaxy contamination. Shortward of Lyα, data has been taken from HST/FOS observations of radio quiet quasars, corrected for Galactic reddening and intergalactic absorption (Zheng *et al.* 1997).

resolved. Intrinsic reddening by dust very close to the AGN can also have a dramatic effect on the slope of the observed spectrum. Problems also arise from combining spectra that may be from objects in intrinsically different states. Therefore, composite spectra, while useful for estimating the total output of the AGN population, do not have any real physical meaning. Models of the source emission need to be able to fit individual spectra.

Most current models interpret the big blue bump as thermal emission from an optically thick, geometrically thin accretion disc. A radial temperature distribution in the disc results in emission approximated by a multi-blackbody spectrum. Therefore, the majority of the flux at different wavelengths is emitted from physically distant regions of the disc.

This immediately causes a problem for these models as variations in the continuum are observed to be virtually simultaneous at optical and UV wavelengths (Ulrich *et al.* 1997). Changes would therefore need to propagate at speeds much greater than the sound speed in the optically thick medium. The multi-blackbody model also has problems fitting the optical continuum slope, usually producing spectra that are too 'blue' to fit the data.

More realistic models consider vertical structure and radiative transfer along the disc, often using stellar atmosphere models. However, these predict features that are generally not seen in AGN ultra-violet spectra. The optical depth to bound-free absorption in the disc will change sharply at the Lyman limit (912 Å). Effectively, photons redward of the Lyman limit may escape from deeper regions of the disk. Therefore, if a temperature gradient is present there should be a Lyman edge in the UV spectrum. A rest-frame Lyman edge feature is rarely observed ($\sim$ 10% of cases, Koratkar & Blaes 1999) and in these is extremely weak. The models also predict electron scattering opacity to be important in the disc which would lead to significant polarisation in an orientation perpendicular to the disc axis. Observed optical polarisations are much lower than those predicted and appear to be parallel to the disc axis, where this can be inferred from radio jets (Kembhavi & Narlika 1999).

In the reprocessed Comptonised emission model discussed in section 1.1.1 it is possible to produce polarisations parallel to the disc axis as well as a smearing out of the Lyman edge. The high polarisations produced by inverse Compton scattering may also be reduced to the level of those observed, through magnetic fields causing Faraday rotation (e.g. Begelman 1994). The reprocessing model appears to be the only way to explain the simultaneity of variations in the optical and UV. However, recent variability studies of NGC 7469 (Nandra *et al.* 1998) and NGC 3516 (Edelson *et al.* 2000) have shown the UV and X-ray bands are not well correlated in these objects. This is contrary to the scenario observed in NGC 4151 and NGC 5548, as previously discussed, and indicates the mechanism may be more complicated than current models suggest.

1.1.3 Infrared continuum

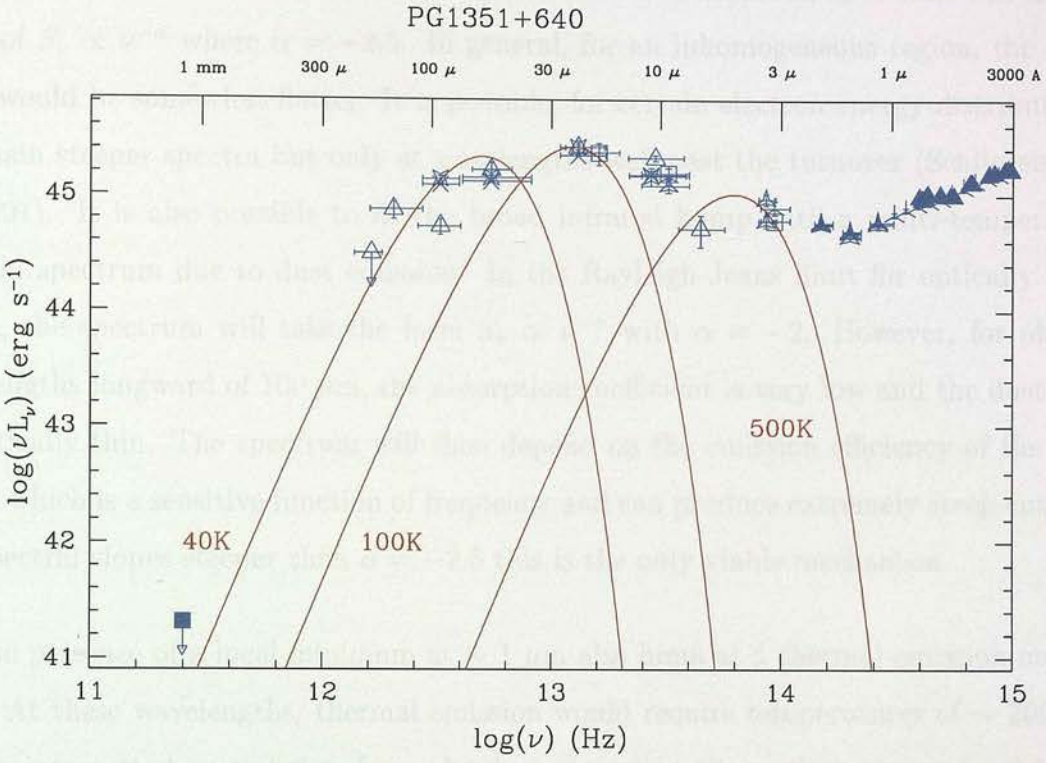

Figure 1.4: Infrared spectral energy distribution of the radio-quiet quasar PG1351+640 (from Wilkes *et al.* 1999).

AGN infrared continua describe a broad, smooth bump between the wavelengths of $\sim$ 2 - 100 μm. The emission is generally comparable in strength to the optical - UV, and is much too wide to be explained by a single-temperature greybody. Figure 1.4 displays the infrared spectral energy distribution of a typical low-redshift radio-quiet quasar, PG1351+640 (Wilkes *et al.* 1999). In the near-infrared the bump ends with a local minimum at $\sim$ 1 μm. Beyond $\sim$ 100 μm there is a sharp drop-off towards the submillimetre.

The infrared emission in AGN can be non-thermal (synchrotron) or thermal in origin. There are a number of diagnostic features in the spectrum that in many cases can unambiguously distinguish between the two. The most important of these is the slope of the steep cut-off at submillimetre wavelengths. The power-law spectrum produced by synchrotron emission can be well fitted to the flat AGN continua at mid-infrared wave-

lengths, with the low frequency turnover explained by synchrotron self-absorption. For a power-law distribution of electrons, a synchrotron self-absorbed spectrum will have a slope of $S_\nu \propto \nu^{-\alpha}$ where $\alpha = -2.5$. In general, for an inhomogeneous region, the spectrum would be somewhat flatter. It is possible, for certain electron energy distributions, to obtain steeper spectra but only at wavelengths well past the turnover (Schlickeiser *et al.* 1991). It is also possible to fit the broad infrared bump with a multi-temperature thermal spectrum due to dust emission. In the Rayleigh-Jeans limit for optically thick media, the spectrum will take the form $S_\nu \propto \nu^{-\alpha}$ with $\alpha = -2$. However, for photon wavelengths longward of 100 μm, the absorption coefficient is very low and the dust may be optically thin. The spectrum will then depend on the emission efficiency of the dust grains which is a sensitive function of frequency and can produce extremely steep cut-offs. For spectral slopes steeper than $\alpha = -2.5$ this is the only viable mechanism.

The presence of a local minimum at ~ 1 μm also hints at a thermal emission mechanism. At these wavelengths, thermal emission would require temperatures of ~ 2000 K. This is interpreted as emission from the dust closest to the nuclear source (~ 0.1 pc). At higher temperatures the grains sublimate and the thermal spectrum will cut-off as the Wien tail of a ~ 2000 K blackbody. A consistent grain sublimation temperature will lead to the observed consistency in the inflection frequency amongst AGN (Sanders *et al.* 1989).

Infrared continuum variability can also provide a valuable diagnostic. The source size for synchrotron self-absorption can be determined from the frequency of the turnover. To explain the 100 μm cut-off, the synchrotron source would be $\sim$ light days across. Variability would therefore be expected over a timescale of days (see section 1.3) for the entire infrared band. For the thermal dust emission scenario, the hotter dust is closer to the central source and covers a smaller region than the cooler dust further out. At ~ 1 μm, variability would be expected on timescales of months to years, while at ~ 100 μm the continuum would vary slowly over thousands of years. As the dust emission is considered to be reprocessed radiation from the central source, the infrared variations should trace variations in the optical - UV. In the case of the Seyfert galaxy Fairall 9, the near infrared

continuum variations have been observed to lag behind UV continuum variations by $\sim$ 400 days (Clavel, Wamsteker, & Glass 1989). This is consistent with emission from dust residing $\sim$ 400 light days from the nucleus. Variations in the far-infrared have only been observed for radio-loud AGN (Edelson & Malkan 1987).

Recent advances in this field have been gained with data from the *Infrared Space Observatory* (ISO). It is now widely accepted that radio quiet quasars are dominated by thermal emission in the far-infrared, while flat spectrum radio-loud quasars usually have a non-thermal component that swamps all other emission (e.g. Haas *et al.* 1998).

In order to fit the infrared continuum of AGN, a range of dust temperatures $\sim$ 50 - 500 K are required (Wilkes 2001). This is difficult to achieve through a model of reprocessed emission from the central source. Sanders *et al.* (1989) proposed a warped-disc geometry to account for the far-infrared emission. Warping is required to increase the covering factor of the disc in order to produce the observed far-infrared to UV ratio. The disc would need to extend a few kiloparsecs from the nucleus in order to produce the longest wavelengths in the infrared bump.

Many models have proposed a toroidal geometry for the emitting dust (e.g. Pier & Krolik 1992, Granato & Danese 1994, Efstathiou & Rowan-Robinson 1995). These generally extend only to mid-infrared wavelengths and find it difficult to account for the cool far-infrared emission. This may be produced further out in a circumnuclear starburst. However, the observed correlation between the mid and far-infrared luminosities indicates that the emission processes must be linked. It is possible that the starburst and AGN are triggered by the same interaction or merger event (Rowan-Robinson 2001).

Whatever the geometry of the emitting dust, it is evident that for an observer behind the optically thick medium, the view of the central radiating source will be obscured. These AGN will appear very different and may not be immediately recognised as active galaxies at all.

1.2 Obscured AGN

1.2.1 Seyfert II galaxies

The majority of AGN seen in the local universe are of low luminosity and are classified as Seyfert galaxies (an often adopted arbitrary criterion is $M_B > -21.5 + 5\log h_0$, Schmidt & Green 1983). All Seyfert galaxies show narrow high ionisation emission lines in their spectra indicating the presence of strong ionising radiation. However, some of these, known as Type I Seyferts, also display a broadening of the permitted lines. This indicates the presence of a dense, fast moving gas ($\sim 10^4$ km s^{-1}), not seen in Seyfert IIs. This gas is thought to be in the form of clouds very close to the centre of the AGN. These may be transient structures blown from the surface of the accretion disc in violent magnetic reconnection events, or perhaps dense inflowing regions. The narrow line region is much further out, with gas velocities of only a few hundred km s^{-1} (Peterson 1997).

Seyfert Is and IIs do not form two distinct groups. There is a continuum of objects in between where the broad line components are only weakly observable and may vary quite considerably. This led to the idea that Seyfert Is and IIs may be intrinsically the same phenomenon viewed through varying amounts of attenuating dust (Rowan-Robinson 1977, Lawrence & Elvis 1982). This may be in the form of a 4π steradian shell of varying thickness, an axisymmetric structure viewed from different angles, or perhaps a patchy dust covering. The idea of a geometrically thick dust torus was put forward on the basis of observations of NGC 1068 and other Seyfert IIs in linear polarised light (e.g. Antonucci & Miller 1985). The broad lines detected in these spectra are thought to be reflected above the torus by a population of free electrons perhaps in the narrow line region. Such observations lead to 'unified schemes' in which all AGN possess an obscuring torus but differ only in orientation. Thus Seyfert Is would be viewed face on with a clear line of sight to the broad line region whilst in Seyfert IIs the torus would be viewed edge on.

The case of Seyfert IIs demonstrates that local and relatively low luminosity AGN

may often be obscured, though it remains unclear whether this is the case for AGN of high luminosity and redshift. There is, however, further evidence for the existence of a large obscured population in the form of the black hole "relic problem".

1.2.2 Quasar relics

Taking the assumption that all the emission from quasars comes from accretion on to a massive black hole, it follows that this emission integrated over the lifetime of the universe should tell us the total mass now residing in the relics of these quasars. Using an observed luminosity function, an assumed cosmology, and a bolometric correction factor, this integrated emission can be calculated from the mean surface brightness of the sky in optical quasar light (Soltan 1982). We then need to estimate a mean accretion efficiency to convert this to a density in black holes. Chokshi & Turner (1992) use an accretion efficiency of 10%, and arrive at a value of $\varrho_{\rm BH} = 2 \times 10^5$ $\rm M_\odot$ $\rm Mpc^{-3}$.

The density in black holes actually observed has also been calculated. Magorrian *et al.* (1998) undertook a kinematic study of 36 nearby galaxies and found evidence for black holes in at least 32 of these. A correlation between the mass of the black hole and the mass of the galactic bulge was also found with an average ratio $\rm M_{BH} \sim 0.006 \times M_{bulge}$. By observing the total integrated emission from starlight in galaxies and converting this to a mean mass of stars in galactic bulges, we can calculate an observed local density in black holes. This comes out to be an order of magnitude higher than that predicted from the integrated quasar emission (Lawrence 1999 and references therein).

The conclusion therefore, is that there appear to be more black holes than we can account for. Unless the assumptions used for these calculations are wrong, there must be a large population of obscured quasars that are not observed at optical wavelengths. This scenario appears particularly plausible if we consider the effects of dust absorption on the optical - UV continuum. Figure 1.5 displays the effect on the AGN continuum of different amounts of absorbing material characterised by their visual extinction ($\rm A_V$). A

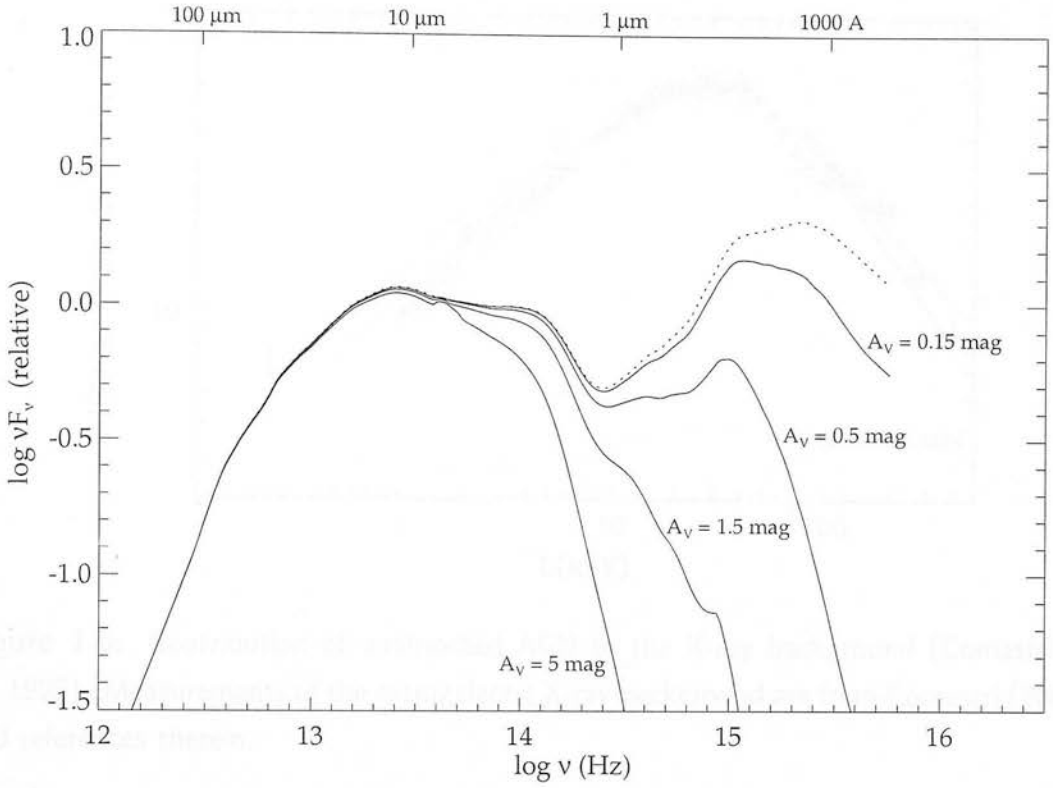

Figure 1.5: Effect of dust absorption on the UV to infrared AGN continuum. This plot has been calculated from the dust extinction model developed in chapter 3 using the mean radio-quiet quasar SED from Elvis *et al.* (1994). A standard gas-to-dust ratio of 2×10^{21} cm^{-2} mag^{-1} would lead to the associated gas absorption plotted in figure 1.7.

relatively small amount of dust can effectively wipe-out the UV emission.

1.2.3 The X-ray background

Another major piece of evidence for the existence of a large population of obscured AGN comes from the nature of the X-ray background.

The spectral shape of the X-ray background is displayed in figure 1.6. In the 3 - 20 keV range the background spectrum can be approximated by a power-law with an energy index of $\alpha \simeq 0.4$ (Comastri *et al.* 1995). The normalisation is somewhat uncertain and varies by up to $\sim 40\%$ between measurements (Vecchi *et al.* 1999). The background peaks at ~ 30

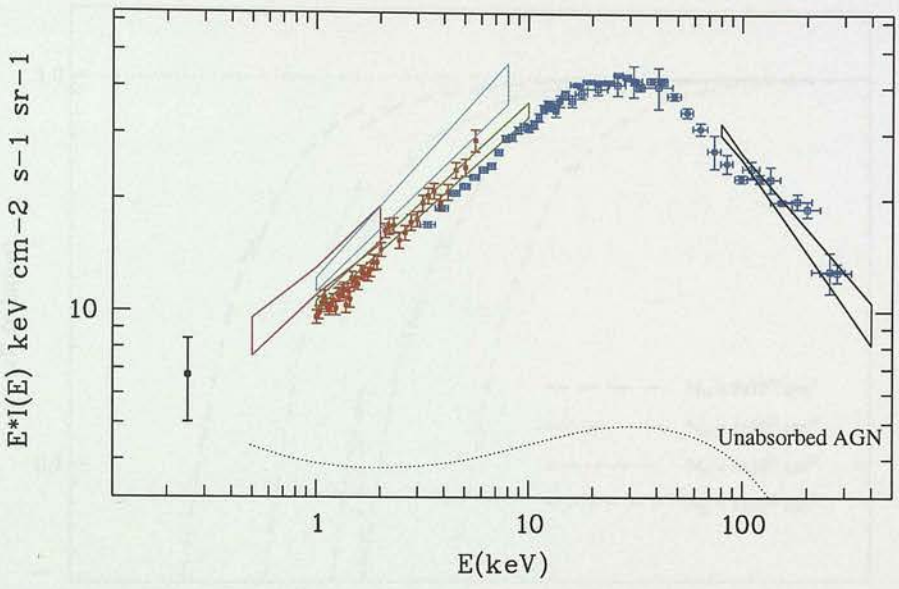

Figure 1.6: Contribution of unabsorbed AGN to the X-ray background (Comastri *et al.* 1995). Measurements of the extragalactic X-ray background are from Comastri (2000) and references therein.

keV (Gruber *et al.* 1999) before dropping away towards higher energies. This spectral shape is almost exactly that expected as a result of thermal bremsstrahlung emission from a hot intergalactic gas. However, a diffuse origin of this kind can now be ruled out due to measurements of the cosmic microwave background. A hot intergalactic gas should inverse Compton scatter photons from the microwave background causing considerable distortions which are not observed (Wright *et al.* 1994).

At soft energies, deep surveys with ROSAT have been able to resolve most of the X-ray background (Shanks *et al.* 1991 $\sim 30\%$, Hasinger *et al.* 1998 $\sim 70-80\%$). Identification of these sources has revealed a high proportion of broad-line AGN (Schmidt *et al.* 1998). At harder energies, however, the spectral shape of the X-ray background and that of broad-line AGN are quite different (Almaini *et al.* 1996). At energies of ~ 30 keV where the X-ray background peaks, the steep spectrum quasars may only contribute $\sim 10\%$ (Fabian *et al.* 1998). There must therefore be a new population of hard spectrum objects appearing at higher energies.

A number of models attempted to ascribe the shape of the X-ray background to a

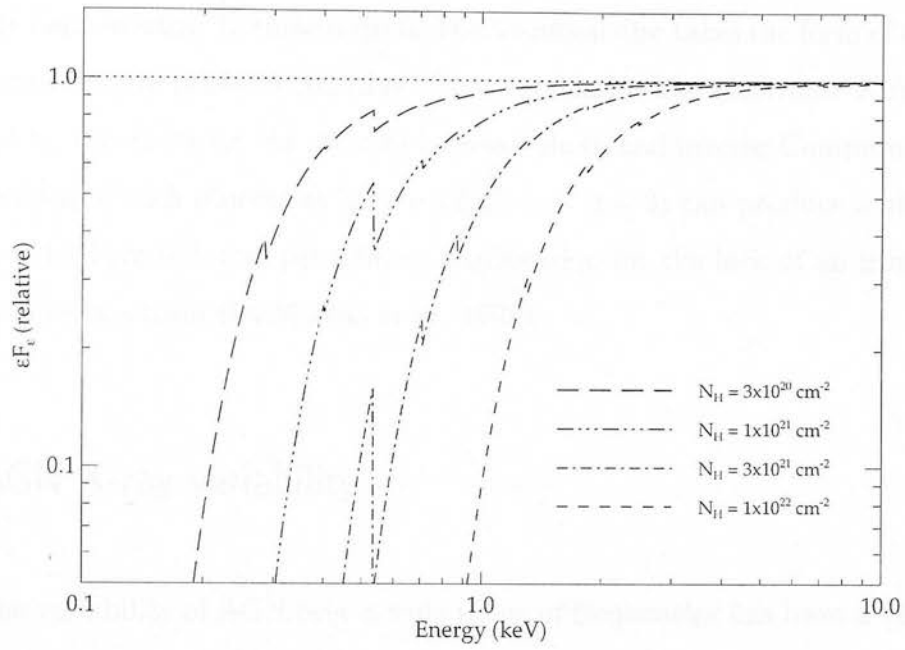

Figure 1.7: Effect of gas absorption on the X-ray AGN continuum (courtesy of O. Johnson).

population of quasars with a strongly enhanced Compton reflection component in their spectra (e.g. Fabian *et al.* 1990). However, these models cannot match the number counts or spectra of sources detected at soft X-rays (Setti 1992, Comastri 1992). The spectra of starburst galaxies and cluster emission are generally too soft to provide a significant contribution. Obscured AGN, however, would have hard spectra due to absorption of soft X-rays by the obscuring gas. Figure 1.7 displays the effect of gas absorption on the X-ray continuum. Increasing columns of gas act to progressively harden the observed spectrum. By adding up the contribution from obscured AGN over a wide range in redshift and column density, one can readily reproduce the spectrum of the X-ray background (e.g. Comastri *et al.* 1995, see section 3.2). Fabian & Iwasawa (1999) used the assumption that the X-ray background is made up of obscured AGN to derive the mass density in black holes. The resulting value is within a factor of 2 of that determined for local galaxies by Magorrian *et al.* (1998), providing a possible solution to the relic problem.

Obscured AGN are not the only viable candidates for the inferred hard spectrum population. Galaxies with an advection-dominated accretion flow (ADAF) would have

intrinsically hard spectra. In these objects, the accretion disc takes the form of an optically thin, two-temperature plasma consisting of hot ions and cooler electrons. X-ray emission is produced by the electrons via thermal bremsstralung and inverse Compton scattering. A superposition of such objects at high redshift ($z \sim 2-3$) can produce a very good fit to the X-ray background, and provides an explanation for the lack of an iron feature in the background spectrum (Di Matteo *et al.* 1999).

1.3 AGN X-ray variability

Study of the variability of AGN over a wide range of frequencies has been a valuable tool in determining the relationship between various emission features seen in AGN spectra (see section 1.1). The intrinsic nature of this variability can also be useful in determining certain characteristics of the source. Variations on a time scale of Δt_{var} in the rest frame, indicate the source of the variable component has a size scale:

$$R \leq c\Delta t_{var} \tag{1.1}$$

For sources larger than R, the variations could not be causally connected over the full extent of the source. This becomes a useful constraint when studying X-rays, which are found to vary faster than any other waveband. The X-ray flux generally accounts for at least 10 % of the total bolometric flux in AGN (e.g. Ward *et al.* 1987), while variations have been observed down to time scales of less than 1 hour. This indicates significant emission is produced in a very small region, and provides strong evidence for the existence of an accreting black hole.

Rapid X-ray variability appears to be very common in AGN (e.g. Turner 1988). Light curves can often look qualitatively very different, but they generally appear completely random in nature with no characteristic time scales or periodicities, indicating there are no long-lived orbiting components. Power spectra show 'red noise' (i.e. more power at lower frequencies), with the form $P(f) \propto f^{-\alpha}$ where $\alpha \approx 1.5$ (Lawrence & Papadakis 1993, Green *et al.* 1993). Departures from a featureless power spectrum are rare. Figure 1.8

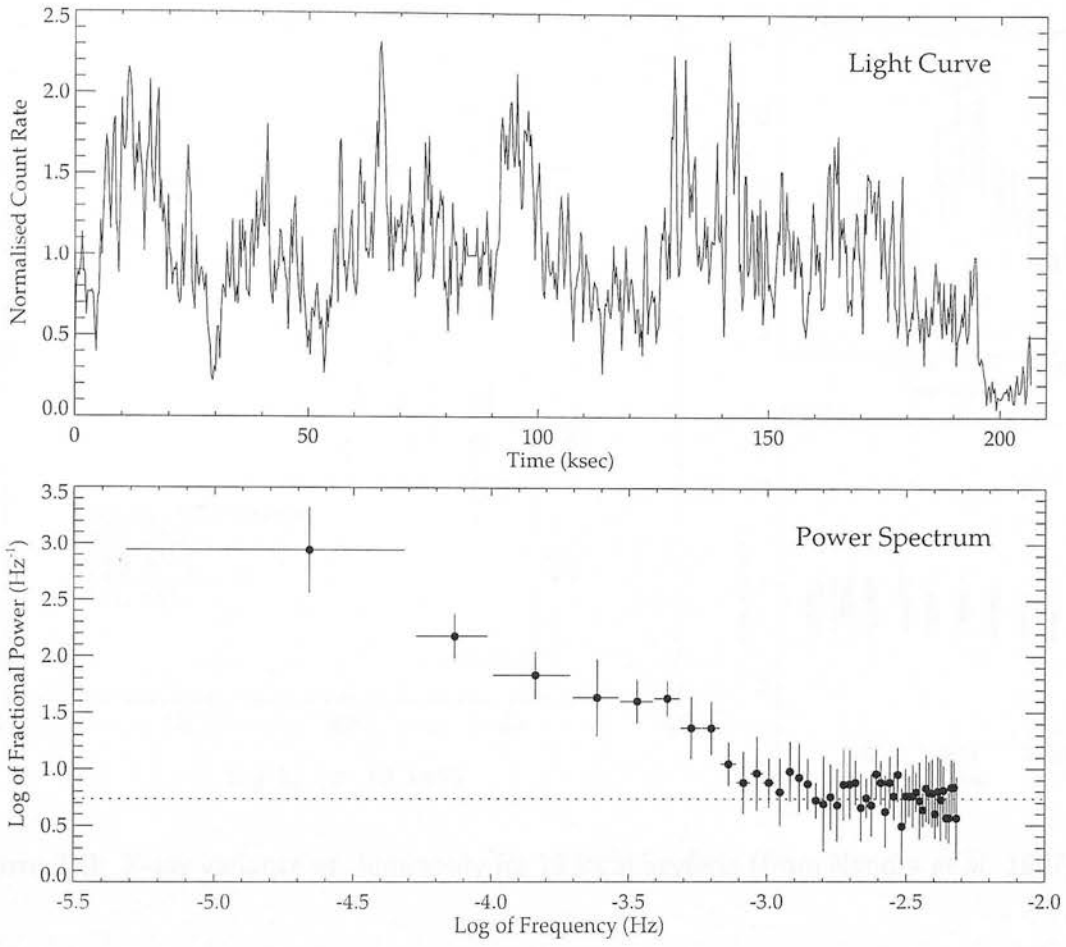

Figure 1.8: X-ray variability of the Seyfert galaxy NGC 4051. Top: Low Energy (0.05 - 2 keV) EXOSAT light curve binned on a timescale of 300 s. Bottom: Temporal power spectrum displaying characteristic 'red noise' and a possible quasi-periodic oscillation at $\sim 4 \times 10^{-4}$ Hz. Data provided by A. Lawrence.

displays the 3 day light curve of a particularly variable Seyfert galaxy, NGC 4051. The power spectrum of this light curve shows the characteristic 'red noise' although excess power is discernible in a broad component around $\sim 4 \times 10^{-4}$ Hz. Papadakis & Lawrence (1995) ascribe this feature to a quasi-periodic oscillation perhaps indicative of an orbital time scale. Some evidence for quasi-periodic oscillations has also been observed in NGC 5548 (Papadakis & Lawrence 1993) and IRAS 18325-5926 (Iwasawa *et al.* 1998), and in a handful of AGN a turnover has been seen at low frequencies (e.g. Edelson & Nandra 1999). A high frequency cut-off would indicate the size of the emission region, although this cannot yet be distinguished from the noise for even the most well studied AGN.

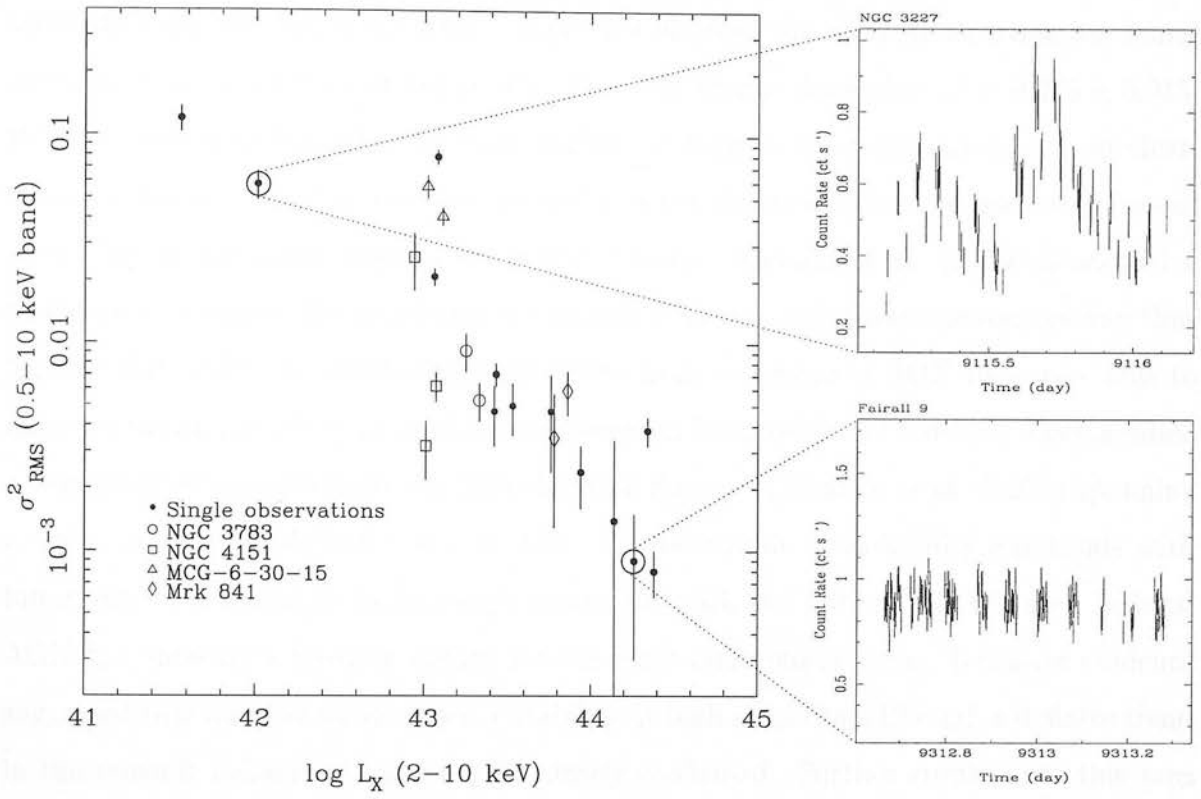

Figure 1.9: X-ray variance vs. luminosity for 18 local Seyferts (from Nandra *et al.* 1997).

Simulated light curves based on the existence of a number of independent flaring regions (i.e. exponential shots) can reproduce the shape of the power spectrum only when the shots are allowed to vary in time-scale. Beyond this, models are difficult to constrain (Green *et al.* 1993).

Variability studies of local ($z < 0.1$) AGN indicate that more luminous sources vary with a lower amplitude. This may be explained if more luminous sources are physically larger in size, so that they are actually varying more slowly. Alternatively, they may contain more independently flaring regions and so have a genuinely lower amplitude. The slope of this correlation has been calculated in a number of papers using overlapping samples of local AGN. Lawrence & Papadakis (1993) and Green *et al.* (1993) analysed samples of light curves from the EXOSAT database. The variability amplitude was found to vary with luminosity as $\sigma \propto L_X^{-\beta}$ with $\beta \approx 0.3$. The most comprehensive analysis of this relation was carried out by Nandra *et al.* (1997, hereafter N97) for 18 local Seyferts

observed with the ASCA satellite. Figure 1.9 displays the clear anti-correlation found between X-ray variance and luminosity. The best fitting slope gives $\beta = 0.355 \pm 0.015$. Whether this well-defined correlation applies to high redshift quasars is not so clear. Observations of distant quasars are generally of low signal-to-noise and measurements of variability in individual objects are poorly defined. Almaini *et al.* (2000) developed a technique to measure the amplitude of variability for low signal-to-noise sources and thus high-redshift AGN. By combining light curves from a number of AGN they were able to measure the amplitude of variability over ranges in luminosity and redshift. They studied a sample of 86 quasars from the Deep ROSAT Survey of Shanks *et al.* (1991) spanning a wide range in redshift ($0.1 < z < 3.2$). The behaviour of variability amplitude with luminosity was found to be in rough agreement with the anti-correlation seen in local AGN but showing a possible upturn for the most luminous sources. Tentative evidence suggested this was due to increased variability at high redshifts, although a definite trend in the redshift behaviour could not be clearly confirmed. Further studies into this area are the subject of the following chapter.

Chapter 2

QSO X-ray Variability

In this chapter I use the techniques of Almaini *et al.* (2000) to determine the amplitude of variability in an expanded sample of QSOs (quasi-stellar objects, or quasars) taken from the ROSAT archive. The primary aim is to identify trends in variability amplitude with luminosity and with redshift. In particular, QSOs at $z > 1$ are preferentially selected in order to investigate the X-ray variability of high redshift QSOs. A cosmology with $q_0 = 0.5$, $H_0 = 50$ km s^{-1} Mpc^{-1} is used throughout.

2.1 The sample

The sample consists of 156 QSOs between $0.08 < z < 4.11$ taken from the ROSAT PSPC archive. It is made up of QSOs taken from a number of sources that all adhere to the following selection criteria:

- ID: Radio quiet quasar
- X-ray exposure > 10,000 seconds
- Flux signal-to-noise > 5

Subsample	Notes	No. QSOs
Deep ROSAT Survey (Shanks *et al.* 1991)	7 deep ROSAT pointings with exposures from 30 - 80 ks over 2-14 days. Broad emission line QSOs, FWHM > 1000 km s^{-1}. (Detailed in Almaini *et al.* 2000.)	84
ROSAT Radio Quiet Quasar catalogue (LEDAS)	Cross-correlation of ROSAT archive sources with the Veron 1993 catalogue for radio quiet 'broad emission line' objects with $z > 1$	28
ROSAT deep survey of the Lockman Hole (Hasinger *et al.* 1998)	Data taken from single 65 ks exposure, to measure short time-scale variations. Object classes a - c selected (broad line AGN). IDs taken from Schmidt *et al.* 1998.	14
Deep ROSAT Survey (McHardy *et al.* 1998)	Data taken from the longer first exposure of 73 ks. Broad emission line objects selected (FWFM > 1000 km s^{-1})	13
Veron 2000 cross-correlated with ROSAT archive sources (LEDAS)	Acts as an update to the ROSAT RQQ catalogue. QSOs selected with $z > 2$, undetected in radio. Veron 2000 QSOs are defined to have 'broad emission lines'.	17
	Total:	**156**

Table 2.1: Samples selected from the ROSAT PSPC archive.

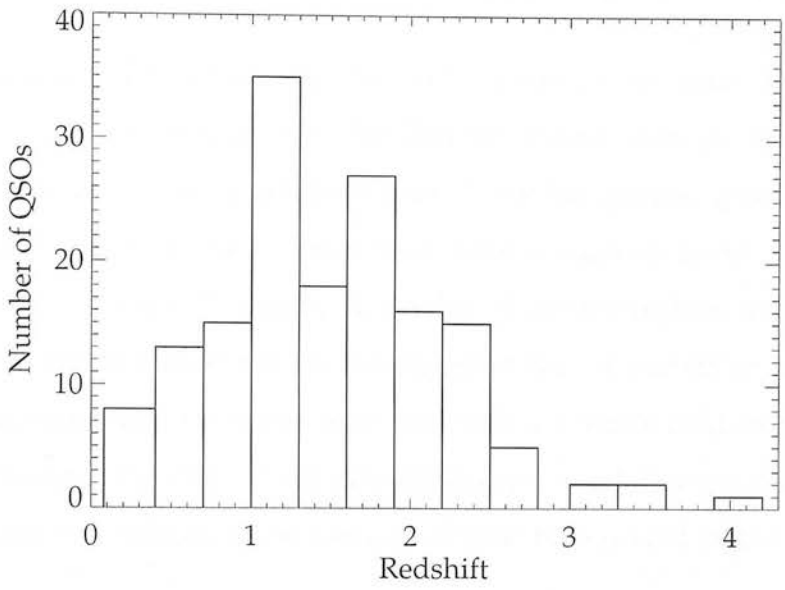

Figure 2.1: Redshift distribution of the sample of 156 radio quiet quasars.

- Within 20 arcmin of ROSAT pointing
- Optimal re-binning (see section 2.2) gives at least 3 time bins

The sample can be broken down into 5 subsamples, individually selected to cover the luminosity and redshift parameter space. These are listed in table 2.1. Only PSPC data was used for reasons of consistency and ease of data reduction. The redshift distribution of the entire sample is displayed in figure 2.1.

2.2 Data reduction

The data were obtained from the LEDAS online database facility at Leicester (ledas-www.star.le.ac.uk). Data reduction was performed with the 'Asterix' X-ray data processing package (www.sr.bham.ac.uk/asterix). Each source was extracted using a circular mask of radius chosen to include 90% of the PSF. The data was then filtered to remove periods of high particle background characterised by the Master Veto Rate rising above

170 counts s^{-1}. Additional filtering restricted the energy range to 0.1 – 2.4 keV.

Careful background subtraction was extremely important to ensure measurement of source variability was not compromised. Background regions were chosen to be as close as possible to the source to minimise the effects of any background gradients. Areas of at least 5 arcmin radius were used. These were large enough to smear out background irregularities due to undetected sources. A number of further regions were selected and compared with the first to ensure that the chosen region did not contain any abnormalities. Finally, the background light curve was compared with the source light curve and a linear correlation coefficient computed. If a highly significant correlation (or anti-correlation) was found the data was reduced again using a different background region.

Binning of the light curves was initially constrained by the orbit of the satellite. ROSAT's low altitude (580km), and overheads led to a typical exposure of 1000-2000 seconds per 96 minute orbit. The light curves were therefore binned on these periodic orbits. An algorithm was then used to bin up the data to allow meaningful Gaussian statistics. Re-binning of light curves can be approached in a number of ways, and important data may be lost if the method used is over-simplified. The algorithm constructed uses the mean intensity of the source to identify bins that would nominally contain less than 15 photons. These bins are merged with the neighbouring bin that has been merged the least number of times. Where large gaps in the data are identified (> 5 hours), bins will be discarded rather than merged with data many orbits away. Light curves with less than 3 time bins were not used for the variability analysis.

In order to remain consistent, all measurements of X-ray luminosity are made through extraction of fluxes from the same datasets used for the variability analysis.

2.3 Measuring variability

The method used for measuring the amplitude of intrinsic variability is fully described in Almaini *et al.* (2000). To compare objects of different flux, the light curves are divided by the mean, so that measurements of *fractional* variability are made. A maximum likelihood technique is used to separate the intrinsic variations in the light curve from those due to noise. The likelihood for values of QSO variability amplitude (σ_Q) is given by:

$$L(\sigma_Q|x_i,\sigma_i) = \prod_{i=1}^{N} \frac{\exp\left\{-\frac{1}{2}(x_i-\bar{x})^2/(\sigma_i^2+\sigma_Q^2)\right\}}{(2\pi)^{1/2}(\sigma_i^2+\sigma_Q^2)^{1/2}} \tag{2.1}$$

where x_i are data points with mean $\bar{x}$ (1 in this case) and σ_i are the measurement errors. The maximum likelihood estimate for σ_Q is obtained from the peak of the distribution. The errors are measured by finding limits of equal likelihood that enclose 68% of the area under the likelihood curve.

The majority of the light curves analysed here are of low signal-to-noise which in many cases can only give us an upper limit on the amplitude of variability. In order to extract meaningful information from the sample it is necessary to combine the light curves into ensembles over given ranges of luminosity or redshift. To do this I assume that all the quasars in an ensemble have the same intrinsic variability. I can then exploit the fact that variance does not depend on the order of the measurements to effectively combine all the light curves into one 'ensemble light curve'. The amplitude of intrinsic variability can then be measured as for a single object. This provides a more comprehensive, accurate and unbiased method of determining variability within an ensemble than simply taking an average of the individual maximum likelihood estimates. Of course, if the quasars in a given luminosity or redshift bin actually have a range of intrinsic variabilities, the estimate may be biased towards the most variable members.

A number of corrections must be made to the variability measurements before they can be compared in an unbiased way. The serendipitous nature of this sample means that light curve observations have a range of total integration times and sampling rates. QSO power spectra show 'red noise' indicating the observed amplitude of variability will increase with

length of observation. I have therefore normalised variability amplitudes to a time-scale of 1 week, assuming the power spectrum slope seen in local AGN ($\alpha = 1.5$). This is also used to correct for time dilation effects. The frequency of variations from distant quasars will be decreased, lowering the measured amplitude of variability for observations of finite length.

A further correction is made for the effects of irregular binning. Low signal-to-noise light curves tend to have longer time bins for which high frequency variations are smeared out. Almaini *et al.* (2000) ran simulations for each QSO in their sample to model the effect of irregular binning on the measured amplitude of variability. For light curves of a given number of bins, a mean correction to the amplitude of variability is determined. I apply this mean correction to each of the QSOs sampled here.

2.4 The results

The maximum likelihood estimates for the corrected intrinsic variability amplitudes of all 156 quasars are displayed in figures 2.2 and 2.3. The size of the points in figures 2.2(a) and 2.3(a) indicate relative flux. This is done in order to distinguish objects of higher signal-to-noise. Nearly half the sample (69 QSOs) give a non-zero maximum likelihood estimate of variability amplitude. The remaining QSOs can only provide upper limits, mainly due to low signal-to-noise. Treating the entire sample as one ensemble, the corrected mean ensemble variability is: $\sigma = 0.15 \pm 0.01$ ($\sigma = 0.16 \pm 0.01$ uncorrected) on a time-scale of 1 week.

2.4.1 Correlations with redshift and luminosity

In figures 2.2 and 2.3 I display the variability amplitude as a function of luminosity and redshift respectively. The data are split into 6 luminosity bins each of ~ 0.5 dex, and 11 redshift bins each of $\delta z = 0.3$. The ensemble variability amplitudes were calculated for

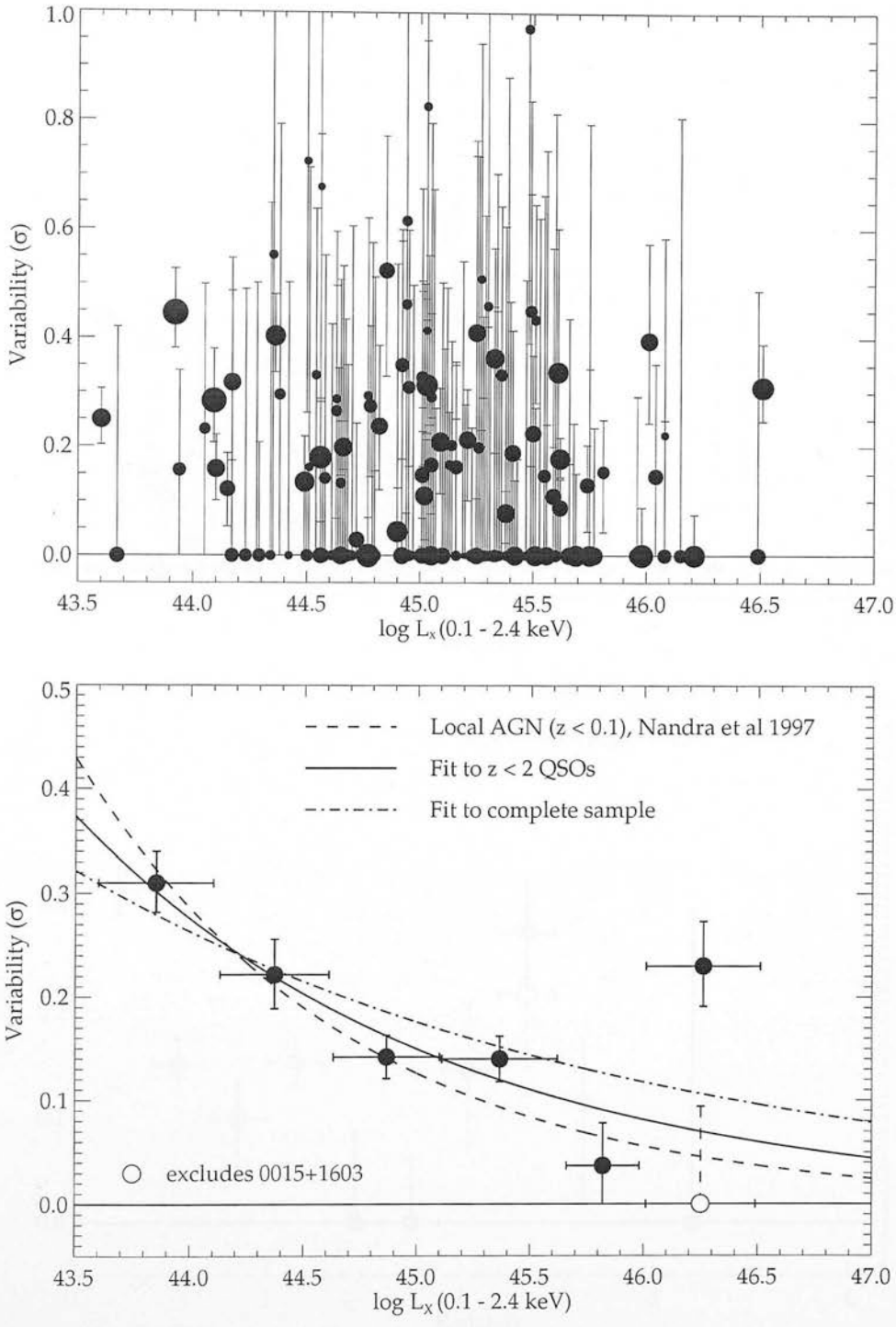

Figure 2.2: (a) Maximum likelihood estimates for the variability amplitude as a function of luminosity for the 156 QSOs. The size of the points indicate relative flux. In (b) I display the results in ensemble form (the vertical scale has been changed). Note, these are calculated from the original light curves and are not averages of the individual likelihood estimates (see section 2.3). The exclusion of QSO 0015+1603 is explained in section 2.5.

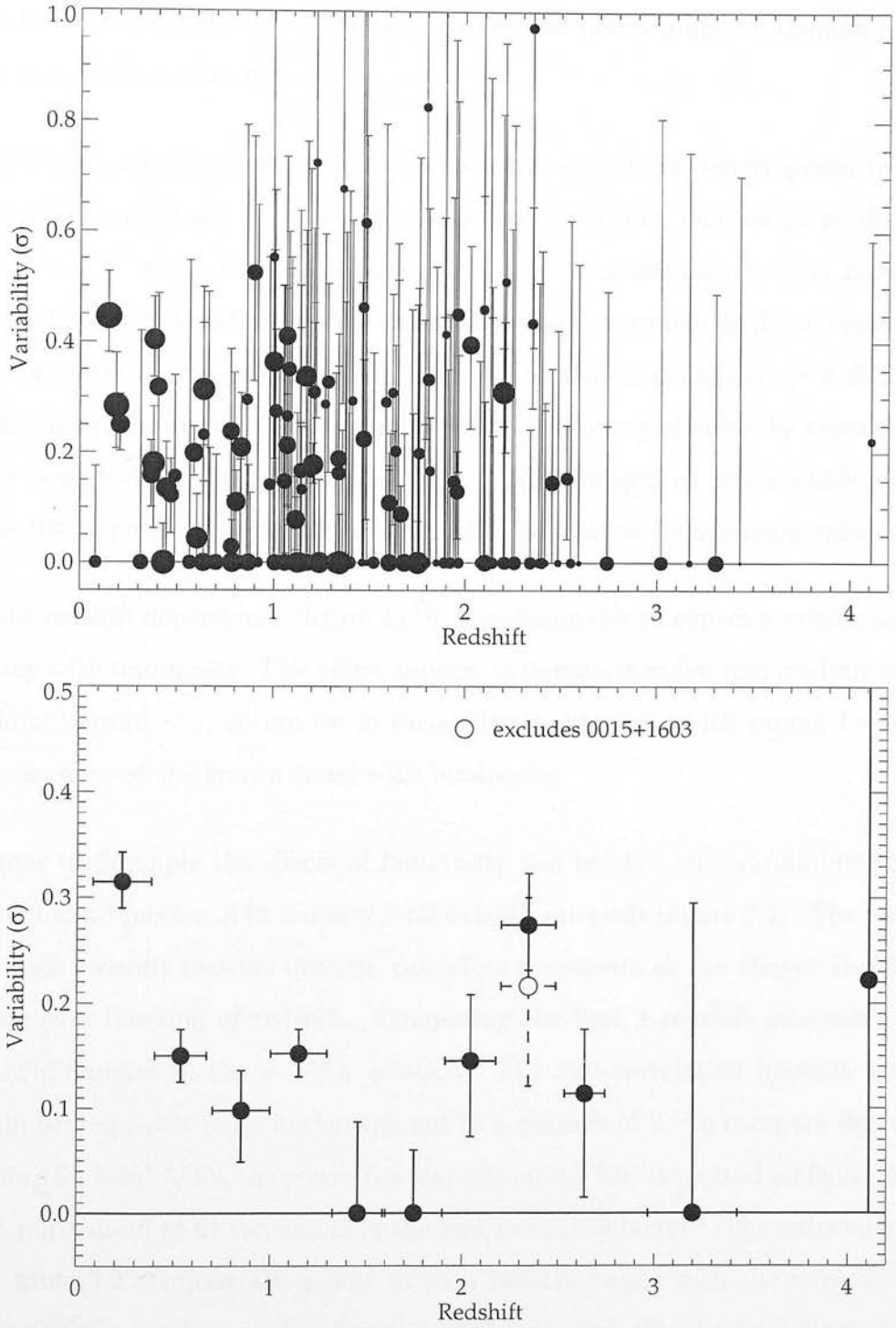

Figure 2.3: (a) Maximum likelihood estimates for the variability amplitude as a function of redshift for the 156 QSOs. The size of the points indicate relative flux. In (b) I display the results in ensemble form (the vertical scale has been changed). Note, these are calculated from the original light curves and are not averages of the individual likelihood estimates (see section 2.3). The exclusion of QSO 0015+1603 is explained in section 2.5.

each bin by combining the individual light curves and performing a maximum likelihood analysis as described in section 2.3.

Immediately apparent in figure 2.2(b) is an anti-correlation between quasar luminosity and variability amplitude. A power law fit to the individual quasars gives the best fit relation: $\sigma \propto L_X^{-\beta}$ where $\beta = 0.18 \pm 0.05$ (plotted as a dot-dash line). This gives a fairly poor fit to the ensemble points, mainly due to some highly variable, high luminosity QSOs. However, a power law fit to QSOs with redshift less than 2 (solid line, $\beta = 0.27 \pm 0.05$) passes through the majority of the ensemble points and is very close to the average relation found for local AGN (plotted as a dashed line). The errors quoted here are 68% confidence limits for the slope on allowing the normalisation to float to its optimum value.

For the redshift dependence (figure 2.3b), it is reasonable to expect a certain amount of degeneracy with luminosity. This effect appears to dominate at low and medium redshifts. At redshifts beyond ~ 2, an upturn in variability is observed which cannot be explained as a consequence of the known trend with luminosity.

In order to decouple the effects of luminosity and redshift, the variability amplitude was plotted as a function of luminosity for 3 redshift intervals (figure 2.4). The luminosity bins for each redshift interval overlap, providing a measure of the change in variability amplitude as a function of redshift. Comparing the first 2 redshift intervals I find no significant difference in the $\sigma - L_X$ relation. The anti-correlation between variability and luminosity appears to be unchanged out to a redshift of 2. To compare this with the relationship for local AGN, the power-law slope found by N97 is plotted on figure 2.4. This has been normalised to fit the points in the first redshift interval.[1] The reduced χ^2 values given in table 2.2 compare the points in each redshift range with the normalised local AGN relation. Low values for the first 2 intervals display the observed close agreement

[1]It would be incorrect to use the normalisation of N97, mainly due to the different observation lengths used (typically less than one day) and the different spectral range used to calculate luminosities. Crude corrections based on a standard power spectrum and X-ray spectral index give variability amplitudes around a factor of 2 lower for the N97 AGN. Given the uncertainties in these corrections and the differing methods of calculating variability amplitudes, this is not thought to be significant.

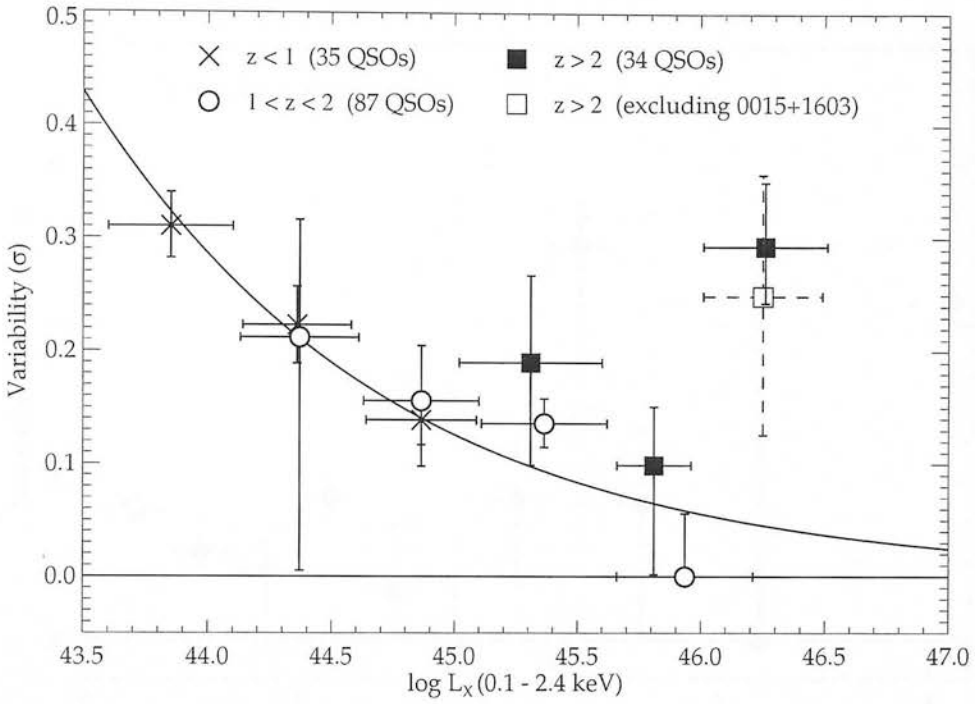

Figure 2.4: Variability amplitude as a function of luminosity over 3 redshift ranges. The line plotted is the best fit relation to local ($z < 0.1$) AGN found by Nandra *et al.* (1997).

QSO sample	$\chi^2_{\rm red}$ fit to local AGN	Probability
$z < 1$	0.1	87%
$1 < z < 2$	1.7	17%
$z > 2$	12.9	0.00001%
$z > 2$ (excl. 0015+1603)	2.0	14%

Table 2.2: Showing agreement between redshift ensembles from figure 2.4, and the best fit relation to local AGN found by Nandra *et al.* ($\sigma \propto L_X^{-0.355}$).

with local AGN. The high value of reduced χ^2 for $z > 2$ can be mostly attributed to the object 0015+1603. However, once this object is removed, the hypothesis that these quasars follow the local $\sigma - L_X$ relation can still be rejected at the 85% confidence level. Considering that all 3 points also show an 'excess' variability indicates that high redshift QSOs may not be well characterised by the variability-luminosity correlation of local AGN.

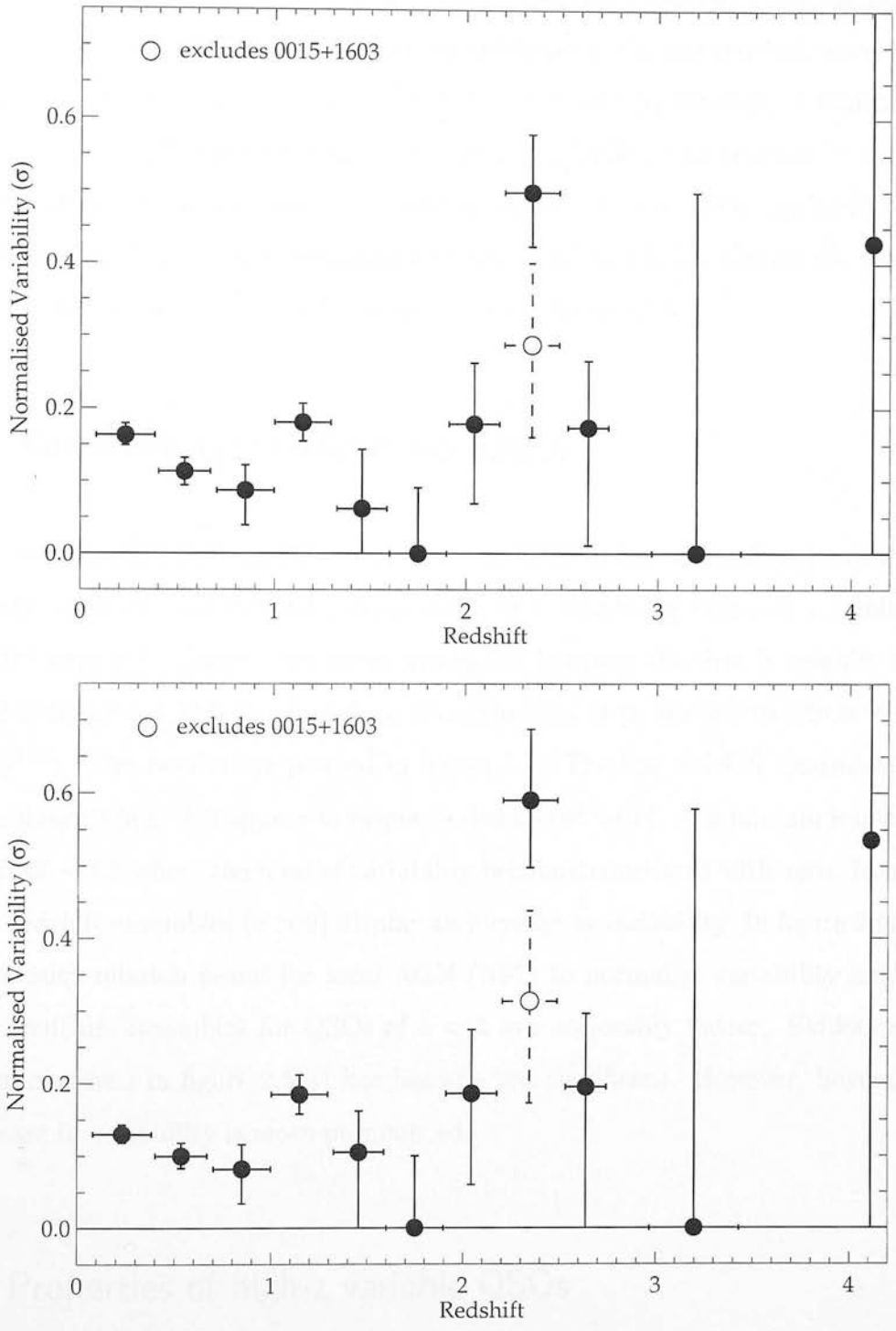

Figure 2.5: Variability amplitude as a function of redshift after removing the luminosity dependence (normalising to $L_X = 10^{45}$). In (a) I use the best-fit power law to QSOs of $z < 2$ of $L_X^{-0.27}$. In (b) the relation for local AGN from Nandra *et al.* (1997) of $L_X^{-0.355}$ is used.

The upturn in variability seen for the highest redshift quasars in our sample can be quantified by fitting the N97 slope to the ensemble points in the redshift interval $z > 2$. This can then be compared to the fit for the $z < 1$ redshift interval. I find at a fixed luminosity, high-z QSOs are more variable than low-z QSOs by an amount $\delta\sigma = 0.11$. An alternative interpretation is that at a fixed variability, high-z QSOs are more luminous by a factor of 16. If I exclude the variable quasar 0015+1603 (see section 6), the best fit requires $\delta\sigma = 0.06$ or an increase in luminosity by a factor of 6.

2.4.2 Characterising the redshift dependence

In order to illustrate the redshift dependence of QSO X-ray variability, I attempted to remove the effect of the luminosity dependence by normalising values to a luminosity of $L_X = 10^{45}$ ergs s^{-1}. Due to the close agreement between the first 2 redshift intervals observed in figure 2.4, this was first done using the best fit power-law to QSOs with $z < 2$ ($\sigma \propto L_X^{-0.27}$). The results are plotted in figure 2.5. The low redshift ensembles (below $z \sim 2$) in figure 2.5(a) still appear to display a downward trend. A minimum is observed at a redshift of ~ 1.7 where the level of variability becomes consistent with zero. In contrast, the high redshift ensembles ($z > 2$) display an increase in variability. In figure 2.5(b) I use the luminosity relation found for local AGN (N97) to normalise variability amplitudes. Here the redshift ensembles for QSOs of $z < 1$ are noticeably flatter. Evidence for the minimum observed in figure 2.5(a) has become less significant. However, beyond $z \sim 2$, the increase in variability is more pronounced.

2.5 Properties of high-z variable QSOs

The apparent increase in variability seen in high redshift QSOs may be due to the inclusion of a new population of objects rather than differences in the 'typical' population. Narrow-line Seyfert 1s are known to exhibit enhanced variability (Boller *et al.* 1996, Leighly 1999)

Name X-ray source name	**RA, Dec.** (J2000.0)	**z**	**log L_X** (0.1-2.4keV)	**Variability** (σ)	**Notes**
1118+1354 RX J112106.0+133825	11 21 06.00, +13 38 25.1	1.94	45.55	0.15 +0.52, -0.15	ROSAT spectrum gives $\alpha \sim 0.3$, Ly α, CIV present Faint emission line quasar (Weedman 1985)
[HBG98] 031 RX J105331.8+572454	10 53 31.80, +57 24 53.8	1.956	45.74	0.13 +0.07, -0.09	Broad SiIV, CIV, CIII] (Lehmann *et al.* 2000)
0438-1638 1E 0438-166	04 40 26.478, -16 32 34.60	1.96	45.49	0.45 +0.39, -0.29	Broad Ly α, CIV (Osmer, Porter & Green 1994)
MS 0104.2+3153 2RXP J010659.1+320920	01 06 58.756, +32 09 18.01	2.027	46.01	0.40 +0.18, -0.15	Broad CIV, SiIV (Gioia *et al.* 1986), BAL quasar with component from foreground IGM (Komossa & Bohringer 1999)
SGP3X:021 SGP 3:48	00 54 47.29 -28 31 54.8	2.097	45.30	0.46 +0.56, -0.46	Broad Ly α, CIV (> 3000km/s, Boyle *et al.* 1990)
0015+1603 2RXP J001749.5+161948	00 17 45.05, +16 19 52.6	2.20	46.51	0.31 +0.08, -0.06	Steep ROSAT spectrum ($\alpha \sim 2.8$) Ly α, CIV present (Anderson & Margon 1987)
F864X:013 (unpublished)	13 43 09.2, -00 22 57	2.21	45.27	0.51 +0.43, -0.31	Broad CIII, CIV (> 3000km/s, Almaini 1996)
F864X:086 RX J1343.4+0001	13 43 29.20, +00 01 33.0	2.347	45.51	0.44 +0.21, -0.15	ROSAT spectrum: $\alpha = 0.6$, Narrow Ly α, CIV (Almaini *et al.* 1995) Broad Hα, no Hβ, type 1.9 QSO (Georgantopoulos *et al.* 1999)
CRSS J1415.1+1140 2RXP J141511.7+114000	14 15 11.20 +11 40 03.0	2.353	45.48	0.97 +0.72, -0.58	Broad Ly α, CIV (Boyle *et al.* 1997)
POX 042 2RXP J120044.8-185952	12 00 44.975, -18 59 45.04	2.453	46.04	0.15 +0.21, -0.15	Broad CIV, SiIV,OIV] (Ulrich 1989)
0315-5522 [ZMH99] X036-04	03 16 50.40, -55 11 09.9	2.531	45.81	0.15 +0.10, -0.11	Broad Ly α, CIV, Si+OIV] (Zamorani *et al.* 1999)
Q0000-26 2RXP J000322.6-260312	00 03 22.909, -26 03 16.83	4.111	46.08	0.22 +0.36, -0.22	Broad Ly α, CIV, SiIV (Schneider *et al.* 1989)

Table 2.3: Notes on high-z variable quasars.

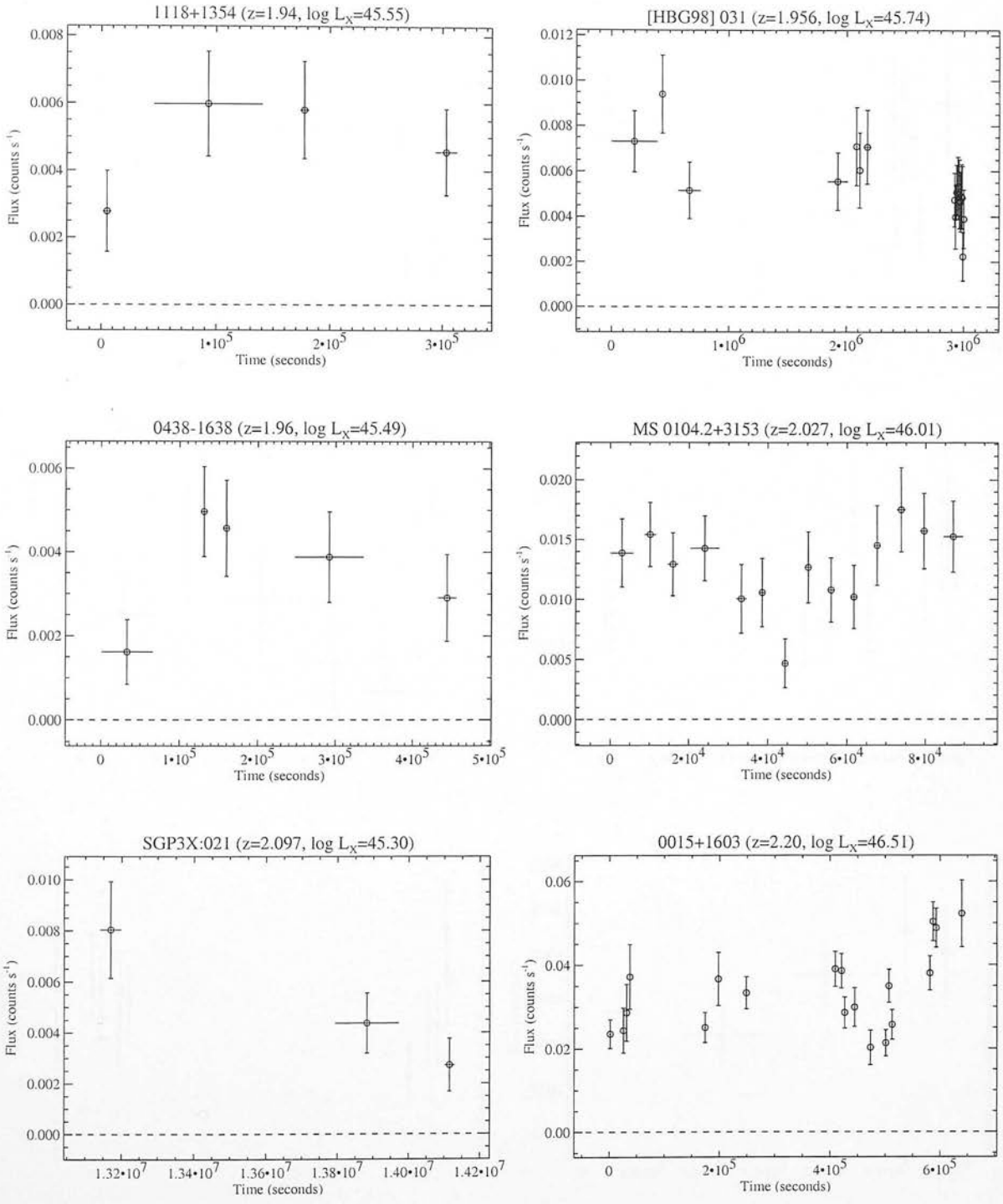

Figure 2.6: Binned soft X-ray light curves of high-redshift variable quasars from the ROSAT PSPC sample.

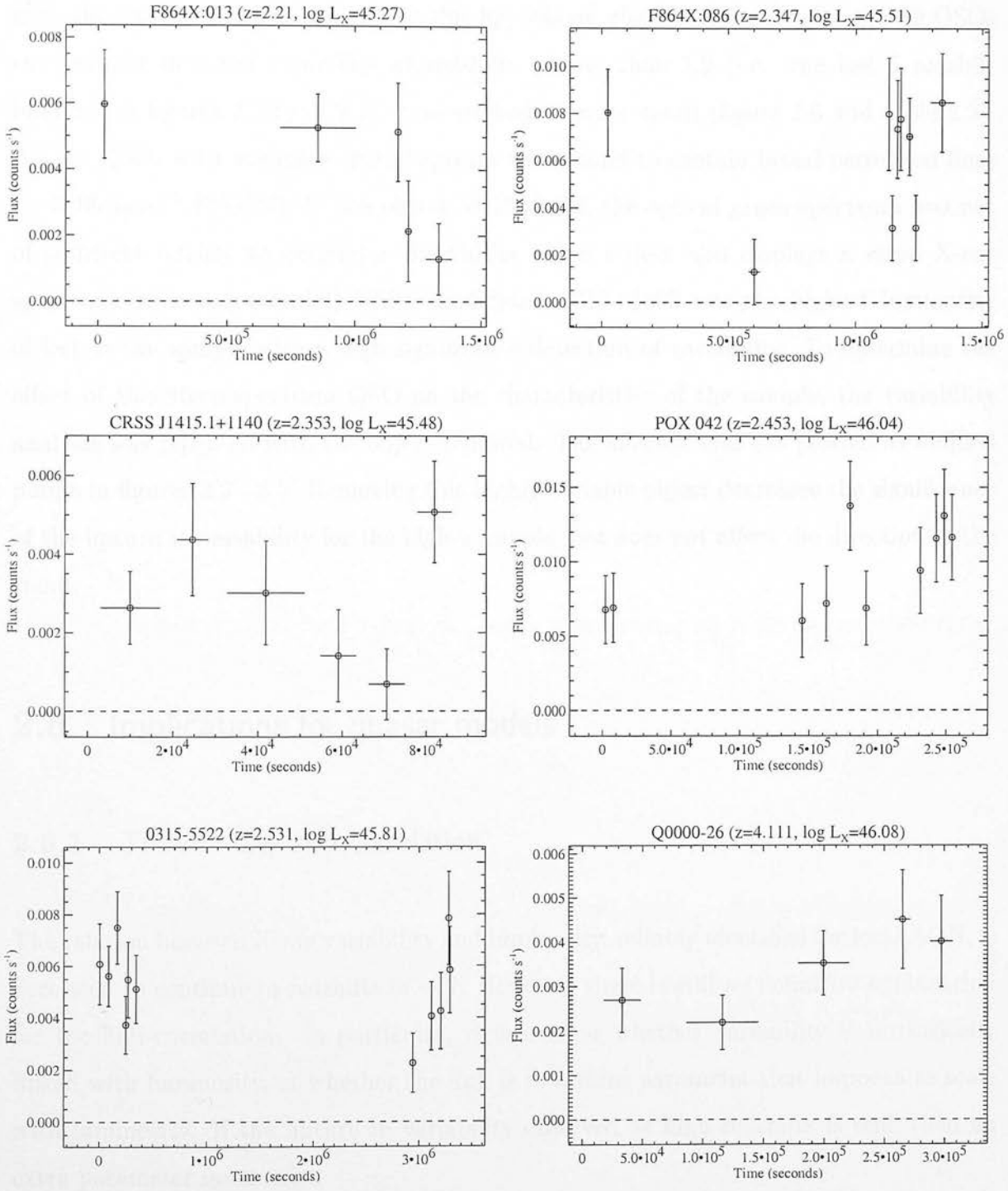

Figure 2.6: Binned soft X-ray light curves of high-redshift variable quasars from the ROSAT PSPC sample (continued).

and could be responsible for this upturn if their high-z equivalents were more prevalent than they are today. In order to test this hypothesis, the identifications for the 12 QSOs that exhibit detected variability at redshifts greater than 1.9 (i.e. the last 5 redshift intervals in figures 2.3(b) & 2.5), were studied in more detail (figure 2.6 and table 2.3). All the QSOs with adequate optical spectra were found to contain broad permitted lines (> 3000 kms^{-1} FWHM). In one object, 0015+1603, the optical grism spectrum was not of sufficient quality to determine linewidths. This object also displays a steep X-ray spectrum, so is a (potential) NLS1 candidate. 0015+1603 was the highest luminosity object in the sample with a high significance detection of variability. To determine the effect of this steep-spectrum QSO on the characteristics of the sample, the variability analysis was repeated with the object removed. The affected bins are plotted as unfilled points in figures 2.2 - 2.5. Removing this highly variable object decreases the significance of the upturn in variability for the high-z sample, but does not affect the direction of the trend.

2.6 Implications for quasar models

2.6.1 The $\sigma - L_X$ anti-correlation

The relation between X-ray variability and luminosity, reliably identified for local AGN, is here seen to continue to redshifts of ~ 2. However, there is still no definitive explanation for the anti-correlation. In particular, it is unclear whether variability is intrinsically linked with luminosity, or whether the link is to a third parameter that happens to scale with luminosity. If the upturn in variability observed at high redshifts is real, then an extra parameter must exist.

A change in measured variability amplitude can occur when the power spectrum of a quasar light curve is shifted in either amplitude or time-scale. At present these cannot be distinguished as features in the power spectrum (such as a turn-over of the power law at

low frequency) have only been identified for the most well studied AGN (e.g. Edelson & Nandra 1999, Pounds *et al.* 2001). This leaves us with a variety of possible explanations for the $\sigma - L_X$ relation, for example:

- A flaring accretion disc may cause the observed correlation in two ways. The luminosity may be related to i) the *number* of flares present on the disc (assumed to be all identical), or ii) the *size* of the individual flares. In the first case, an increase in the number of overlapping flares would act to 'smear out' the observed variability leading to an amplitude shift in the quasar power spectrum. The second case could lead to a time-scale effect if flares of longer duration are responsible for the increased luminosity.
- X-ray variability time-scale may directly scale with black hole mass if, for example, the emission occurs at a fixed number of Schwarzschild radii.
- Regardless of black hole mass, variability may depend on X-ray source size, which could in turn depend on luminosity.

Recent studies by Ptak *et al.* (1998) show that most low-luminosity AGN (LLAGN) display very little X-ray variability, in marked contrast to the relation found by N97. However, these objects are expected to harbour relatively massive black holes with low accretion rates. Iwasawa *et al.* (2000) studied the variability of a dwarf Seyfert (NGC 4395) which is thought to contain a small black hole ($\sim 10^5$ $M_\odot$). They find a large variability amplitude consistent with an extrapolation of the power-law fit to the $\sigma - L_X$ relation for the sample of N97. This would suggest that X-ray variability correlates with black hole mass, rather than directly with luminosity.

2.6.2 Explaining the high-redshift upturn

Given the possible reasons for the $\sigma - L_X$ anti-correlation, I can now identify potential causes for a high-redshift upturn in variability. It is tempting to think this may be

simply due to a smaller typical black hole mass at these early epochs. In practice, this scenario does not work. Smaller black holes may lead to increased variability, but they should also lead to lower luminosities. These QSOs would then just fit an extrapolation of the measured $\sigma - L_X$ relation. Therefore, we may be seeing an intrinsic change in the behaviour of these objects. For the same variability seen in local AGN, these high redshift quasars appear almost an order of magnitude more luminous. The root of this shift in behaviour could be a change in the following parameters:

i) Intrinsic change in luminosity (i.e. accretion efficiency)

It seems reasonable to assume the amplitude of variability is linked with a global property of the QSO, such as black hole mass. The luminosity of the quasar must in some way be related to the rate of fuelling ($\dot{M}$). Seeing a different $\sigma - L_X$ relation at high redshift then suggests that for a given black hole mass, the high-z quasars must have a greater rate of fuelling, in other words, they are accreting at a higher fraction of the Eddington limit. Is it then feasible that $z > 2$ QSOs are accreting more efficiently than local AGN by almost an order of magnitude?

The Eddington ratio for local AGN has been relatively well constrained. Wandel *et al.* (1999), use reverberation methods to accurately define the Eddington ratio for local Seyferts. They find $L/L_{Edd} \approx 0.01 - 0.3$, though there is a strong trend of the Eddington ratio to increase with luminosity. The necessary increase in accretion efficiency to allow a typical high redshift QSO to be almost an order of magnitude more luminous, would imply these objects were accreting very close to the Eddington limit.

If this increase in accretion efficiency is real, the cause must lie with the environmental conditions at these redshifts. It is plausible that early QSOs enjoyed a more fuel-rich environment. This may lead to a scenario where local AGN and quasars at redshift $>$ 2 are similar in nature. However, the high-z QSOs are, on average, accreting close to maximum efficiency, whilst low-z AGN have become starved of fuel and typically only

reach 10% of the Eddington limit.

ii) Intrinsic change in variability

The upturn may also be characterised as an increase in variability for QSOs of the same luminosity. Possible scenarios include:

1. The X-ray emitting region is physically smaller in size, but of greater intensity, for high-z QSOs. This could occur if the emission region was located at a smaller number of Schwarzschild radii.

2. In the flaring accretion disc model, there may be a smaller number of more luminous flares for high-z QSOs. Enhanced magnetic fields could conceivably provide a mechanism to achieve this.

3. It is possible that some short time-scale variability is caused by temporary obscuration of the X-ray source. This could be due to broad-line clouds moving across the line of site, or perhaps rotations of a warped accretion disc. It is feasible that high-z QSOs may contain more of this obscuring material, leading to enhanced variability over these time-scales.

iii) Spectral sampling

The ROSAT band of 0.1 - 2.4 keV used for the variability analysis, will sample higher rest frame energies as redshift increases. For a QSO at a redshift of 2.5, variability will actually be measured in the rest frame band of 0.35 - 8.4 keV. The increased variability observed at high redshift could therefore be due to intrinsic spectral variability. This would require QSOs to be more variable at harder energies indicating a different source for these X-rays. However, N97, showed there was a strong correlation between hard band (2-10keV) and soft band (0.5-2 keV) variability in local AGN. Where the correlation breaks down they find greater variability in the soft band.

iv) Emergence of a new population

An increase in mean AGN variability would be observed if a subset of highly variable AGN (such as Narrow-line Seyfert 1s) were more prevalent at high redshift. Based on the optical spectra however, I find no evidence that this is due to the emergence of a 'narrow-line' population (see section 2.5).

Given the low signal-to-noise of this data it is difficult to constrain these models beyond the general descriptions given here. A full power spectrum analysis is required to fully characterise and confirm this trend. This may be possible with long observations using XMM-Newton, XEUS or Constellation-X.

2.7 Conclusions

I have measured the amplitude of short-term X-ray variability of 156 radio quiet quasars taken from the ROSAT PSPC archive over a redshift range of 0.08 - 4.11. In order to identify trends with luminosity and redshift I have combined light curves into ensembles. For QSOs out to redshift ~ 2 I find the amplitude of variability decreases with luminosity as $\sigma \propto L_X(0.1 - 2.4keV)^{-\beta}$ with $\beta = 0.27 \pm 0.05$. This is comparable to the relation found for local AGN. The behaviour of QSO variability amplitude with redshift is approximately flat out to $z \sim 2$, although there is some suggestion of a minimum at $z \sim 1.7$. Beyond redshift ~ 2 there is some evidence for an increase in QSO X-ray variability. The hypothesis that these quasars observe the local $\sigma - L_X$ relation found by Nandra *et al.* (1997), is marginally rejected. I explore the possible reasons for this upturn. If the amplitude of X-ray variability is linked to black hole mass, this would imply nearly an order of magnitude increase in accretion efficiency for typical high-redshift QSOs.

Chapter 3

Obscured AGN & the Extragalactic Background

A number of models (e.g. Comastri *et al.* 1995) have been able to accurately fit the X-ray background using the integrated spectral emission from an obscured population of AGN. The presence of this hidden population will have implications for other wavebands. We can put constraints on these models by predicting where emission from obscured AGN should be observed, their contribution to the background light, and number-flux relations for different wavebands.

Here I attempt to quantify the contribution of this obscured population to the entire cosmic background from submillimetre to UV wavelengths. For this to be done, a number of assumptions are made on the nature of AGN emission and their evolution with redshift. A standard mean spectral energy distribution (SED, Elvis *et al.* 1994) is used as the baseline for a typical 'unobscured' radio quiet quasar. The emission from an obscured quasar of a certain column density is then synthesised, firstly by assuming a standard gas-to-dust ratio, and secondly, by invoking a possible extinction curve to redden the SED. I assume that re-emission of the absorbed radiation need not be considered. This is consistent with unified schemes for AGN (Antonucci 1993), where to first order, emission

from the absorbing torus is present in the 'unobscured' quasar SED. This would not be the case if obscured objects actually contain more absorbing material, a possibility which is not explored further here.

Number counts for unobscured objects are obtained from a model of the QSO X-ray luminosity function (XLF) from Boyle *et al.* (1994). Ratios of obscured objects are then taken from Comastri *et al.* (1995), who base their background synthesis model on the 'Boyle luminosity function'. I have assumed that the degree of obscuration is not dependent on luminosity.

3.1 QSO luminosity function.

The luminosity function gives the space density of QSOs as a function of their luminosity. Its evolution with redshift is indicative of how QSOs themselves evolve with time. Determination of this evolution has been hampered by the fact that the QSO luminosity function is very close to a power law. A movement of this power law with redshift cannot distinguish between pure density and pure luminosity evolution.

Boyle *et al.* (1994) identified a feature in the luminosity function of X-ray selected broad line QSOs that allows its evolution with redshift to be traced. The sample of quasars used excludes narrow line objects and shows no evidence for photoelectric absorption in the X-ray spectra (Almaini *et al.* 1996). I can therefore use this luminosity function to represent the population of 'unobscured' AGN. Its form is parameterised into two power laws intersecting at a 'break luminosity':

$$\Phi_X(L_X) = \begin{cases} \Phi_X^* L_{44}^{-\gamma_1} & L_X < L_X^*(z=0) \\ \\ \frac{\Phi_X^*}{L_{44}^{*(\gamma_1-\gamma_2)}} L_{44}^{-\gamma_2} & L_X > L_X^*(z=0) \end{cases} \tag{3.1}$$

where γ_1 and γ_2 represent the low and high luminosity slopes of the XLF respectively and L_{44} is the $0.3-3.5$ keV luminosity expressed in units of 10^{44} erg s^{-1}. The evolution with

redshift was best fitted with a 'pure luminosity evolution' model that becomes stationary at a maximum redshift z_{max}:

$$L_X^*(z) = \begin{cases} L_X^*(0)(1+z)^k & z < z_{max} \\ \\ L_X^*(z_{max}) & z > z_{max} \end{cases} \tag{3.2}$$

The parameters used were $z_{max} = 1.79$, $k = 3.34$, $\gamma_1 = 1.53$, $\gamma_2 = 3.38$, $L_X^* = 10^{43.70}$, and $\Phi_X^* = 0.63 \times 10^{-6}$ Mpc^{-3} for a cosmology with $q_0 = 0.0$ and $H_0 = 50\,\mathrm{km\ s^{-1}Mpc^{-1}}$ (Model S, Boyle *et al.* 1994).

The best fit of a pure luminosity evolution model would indicate that either: a) Quasars are long lived phenomena and have been dimming systematically since the 'quasar epoch' at redshift ~2, or b) Short lived quasars are being produced at the same rate but with progressively lower luminosities.

Hypothesis a) predicts that only a fraction of galaxies would contain extremely massive black holes. This seems to be refuted by observational evidence for the existence of massive black holes in almost every local galaxy (Magorrian *et al.* 1998).

Hypothesis b) appears counter intuitive as some density evolution would be expected. If AGN are sparked by mergers as has been theorised (e.g. Carlberg 1990), the number of these phenomena should decrease as mergers become less common. However, the details of AGN ignition are little understood and cannot easily be used as a constraint.

The 'Boyle luminosity function' has been used as a major factor in the background calculations presented here.

3.2 Synthesis of the hard X-ray background

Comastri *et al.* (1995) used this XLF in a model to fit the hard X-ray background using contributions from a large obscured AGN population. In this model the intrinsic X-ray

spectrum of the obscured objects was assumed to be the same as for the unobscured ones, modified by the effects of an absorbing column of density N_H (atoms cm^{-2}). Contributions from obscured objects were divided into four decade wide bins in N_H ranging from 10^{21} to 10^{25}. For the best fit model, the number density in each bin, normalised to the number of unobscured AGN was 0.35, 1.10, 2.30, & 1.65 respectively.

Within this model, AGN contribute 100% of the hard X-ray background from 5 - 100 keV. The contribution in the 1 - 2 keV band is 74%. This is consistent with a contribution from galaxy clusters of 5% (Piccinotti *et al.* 1982) and a significant contribution from starburst galaxies in this band.

A major assumption of this model is that the luminosity function of Boyle *et al.* does not change with the degree of obscuration. This predicts the existence of highly absorbed, high luminosity objects, very few of which have been detected (e.g. Almaini *et al.* 1995, Boyle *et al.* 1998, Stern *et al.* 2002). In the absence of any model for the luminosity dependence of obscuration I have continued to apply this assumption in these calculations.

The contribution of obscured sources found by Comastri *et al.* is extrapolated to longer wavelengths by simulating their combined spectral energy distributions from the submillimetre through to the extreme ultra-violet.

3.3 A 'standard' quasar SED

AGN often display widely varying spectral energy distributions. There appears to be a distinct difference between the output of radio quiet and radio loud AGN particularly in the X-ray, and longward of the mm break (Elvis *et al.* 1994). Given that radio loud objects only contribute a few percent to the X-ray background at 2 keV (Della Ceca *et al.* 1994), I will only consider radio quiet objects. Other variations in the SEDs may be due to dust and gas extinction, a spectral luminosity dependence, or just a random dispersion about the mean value indicating varying contributions from different features

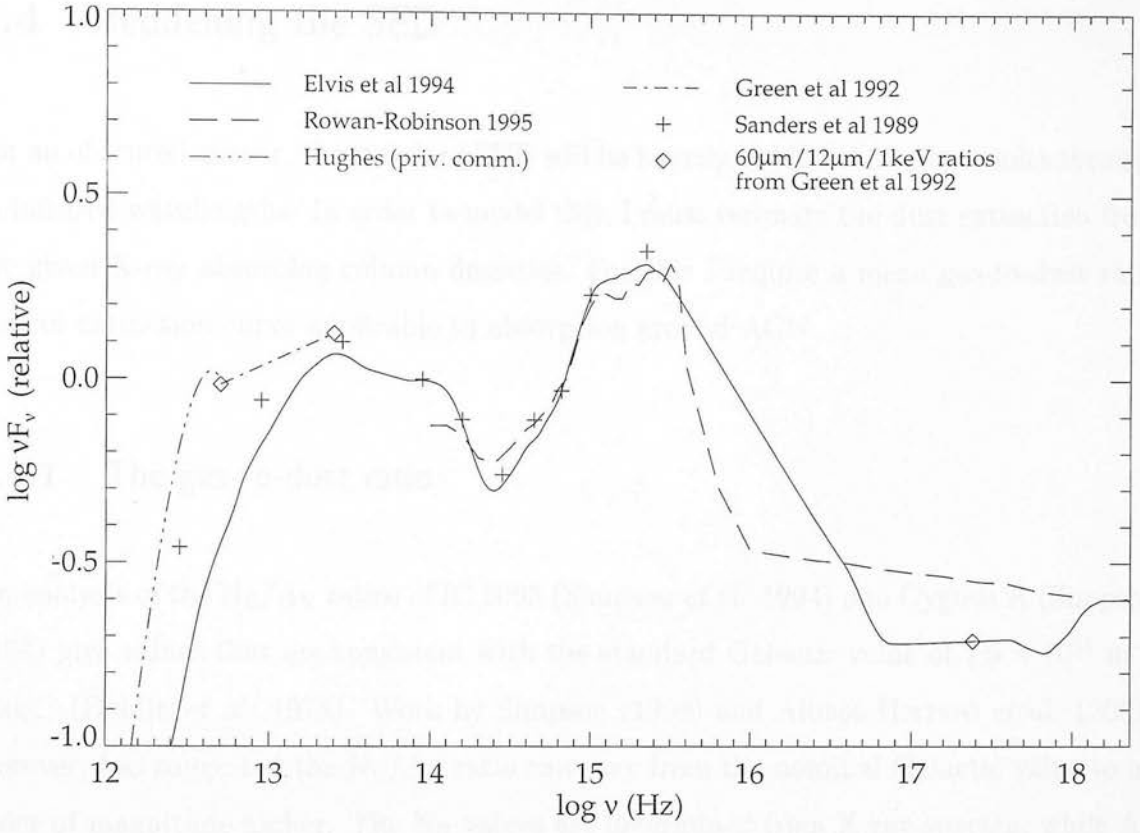

Figure 3.1: Mean spectral energy distributions constructed from a number of sample quasar populations.

of the active nucleus.

For the purposes of these calculations, I require a mean SED for 'unobscured' radio quiet quasars. Elvis *et al.* (1994) used a sample of 29 radio quiet, UV excess selected quasars to construct a mean SED. This is compared (figure 3.1) with those of Rowan-Robinson (1995), and Sanders *et al.* (1989), who used a similar sample. For all of these, quasars of relatively high luminosity are used, and a fairly sharp cut-off is seen in the far-infrared. Contrasting this with the far-infrared to X-ray ratio from Green *et al.* (1992), and the SED of D. H. Hughes (private communication), obtained from relatively low luminosity AGN, it appears there may be a luminosity dependence at these wavelengths. The SED from Elvis *et al.* (1994) is used for the basic model. However, I include an 'alternative SED' model to demonstrate these discrepancies in the far-infrared.

3.4 Reddening the SED

For an obscured quasar, the standard SED will be heavily reddened at ultra-violet through to infrared wavelengths. In order to model this, I must estimate the dust extinction from the given X-ray absorbing column densities. For this I require a mean gas-to-dust ratio and an extinction curve applicable to absorption around AGN.

3.4.1 The gas-to-dust ratio

An analysis of the N_H/A_V ratios of IC 5063 (Simpson *et al.* 1994) and Cygnus A (Simpson 1994) give values that are consistent with the standard Galactic value of 1.9×10^{25} m^{-2} mag^{-1} (Bohlin *et al.* 1978). Work by Simpson (1998) and Alonso-Herrero *et al.* (2001) however, has suggested the N_H/A_V ratio can vary from the nominal Galactic value to an order of magnitude higher. The N_H values are determined from X-ray spectra, while A_V is measured from the broad-band spectrum of the unresolved IR nuclei. Unresolved IR sources have been clearly seen even in Compton-thick objects like NGC 1068, indicating very high N_H/A_V ratios. The need for large X-ray fluxes to obtain good N_H values has meant that only Seyferts have been used and sample sizes are small. Data is not yet available to determine whether the ratio is luminosity dependant.

Granato *et al.* (1997) suggest the gas and dust regions within the nucleus are physically distinct. They show that X-ray column density can be related to the ratio L/L_{Edd} implying the absorbing gas is located inside the dust sublimation radius and directly feeding the black hole. This scenario would not conflict with the use of a 'standard' ratio so long as a mean value can still represent the distribution. They do however suggest that the ratio may increase with increasing N_H, up to around an order of magnitude as N_H reaches values of $\sim 10^{24}$ cm^{-2}.

For these calculations I have used the standard Galactic ratio for the baseline model. I have also considered a model for which the ratio is an order of magnitude higher. Were the

ratio to have an N_H dependence the result would fall somewhere between these models.

3.4.2 Extinction curves for AGN

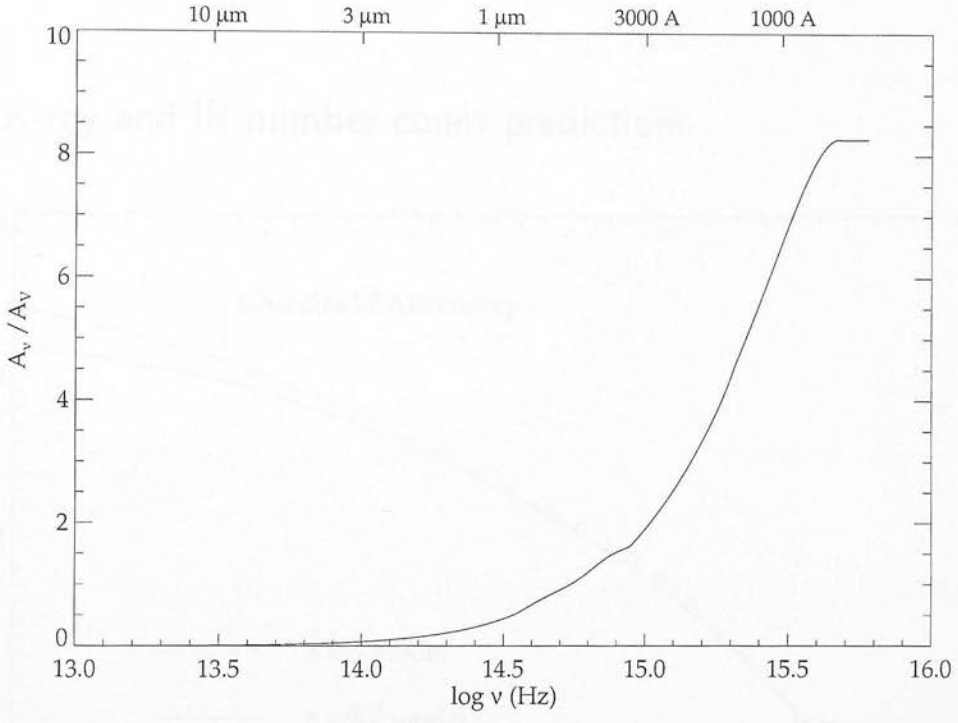

Figure 3.2: Assumed AGN extinction curve, constructed from observed extinction in the Small Magellanic Cloud ($\nu > 9 \times 10^{14}$ Hz) and in the Milky Way ($\nu < 9 \times 10^{14}$ Hz).

The extinction properties of dust in AGN have not been well constrained. The extreme conditions within an active nucleus make it unlikely that a standard galactic curve will be viable, as demonstrated by the lack of an absorption feature at 2200Å in most quasar spectra. The fact that the opacity of the interstellar medium becomes very high below the Lyman limit of 912Å means there is little data to determine an extinction curve at these wavelengths. For these reasons I am required to construct a reasonable extinction curve from available data in a manner similar to that of Tripp *et al.* (1994). I take the standard Milky Way extinction curve from Cardelli, Clayton, and Mathis (1989) down to a wavelength of $\sim$ 3400Å. Below this wavelength I use a mean extinction curve from the Small Magellanic Cloud (SMC) given by Gordon & Clayton (1998). (Extinction in the

SMC does not display a bump at 2200Å.) I then arbitrarily level off the extinction curve below $\sim$ 700Å. There is some evidence that extinction may decrease again below these wavelengths (Laor & Draine 1993). However this will have little effect on the model, and the SED is, in any case, very uncertain in this region.

3.5 X-ray and IR number count predictions

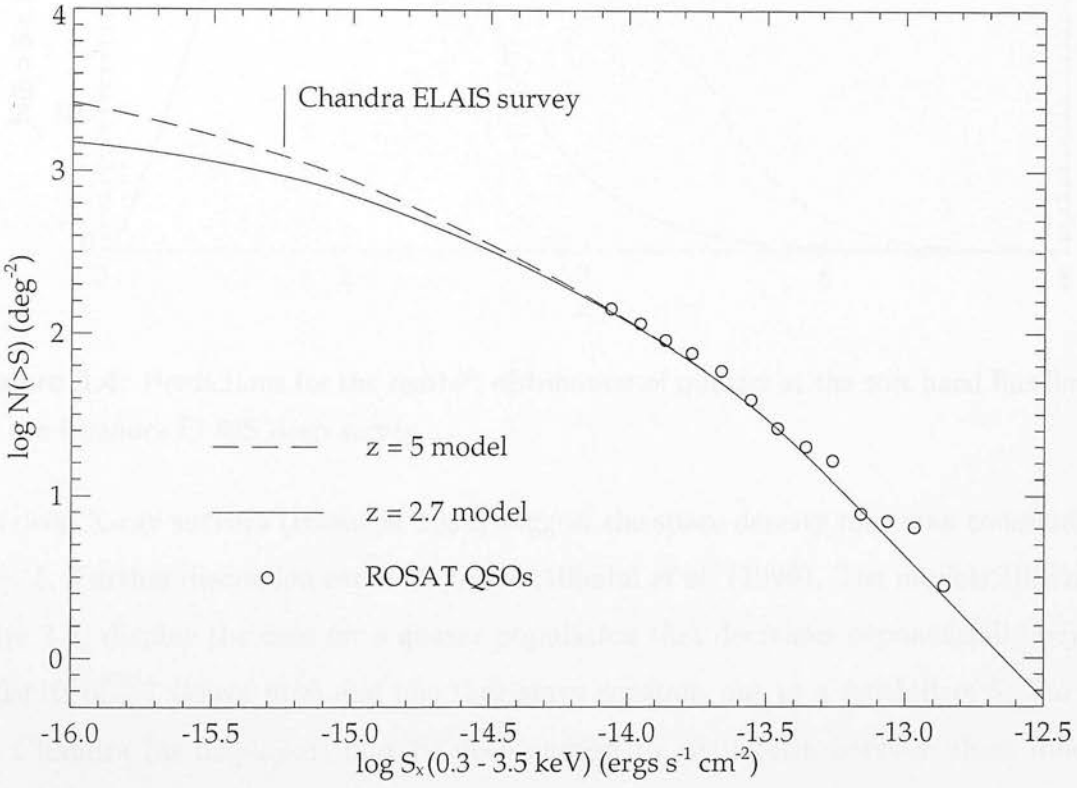

Figure 3.3: Quasar number count predictions for X-ray surveys.

Before modelling predictions for the entire background, number count predictions in the X-ray and IR were made by way of a log N - log S plot. The X-ray luminosity function from Boyle *et al.* (1994) was used to obtain number counts for AGN in the band 0.3 - 3.5 keV (see appendix A). The survey used for construction of the luminosity function contained very few quasars beyond z = 3. Optical surveys suggest an exponential decline in quasar space density beyond z = 2.7 (Schmidt *et al.* 1995). However, recent evidence

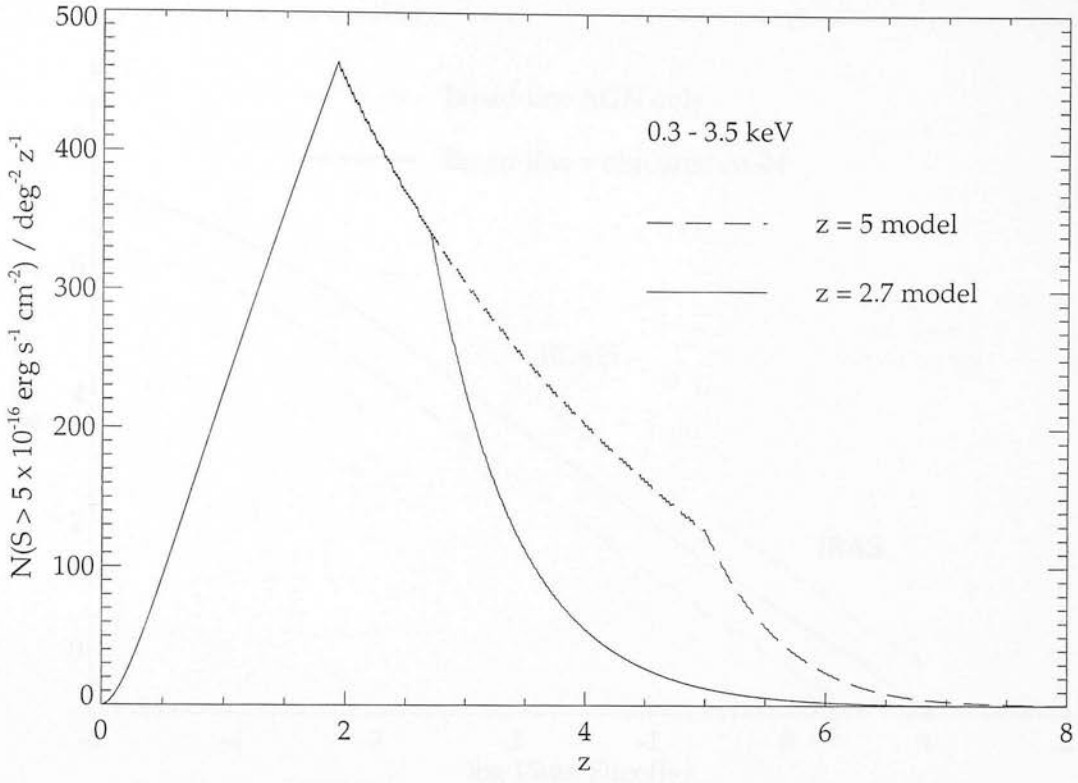

Figure 3.4: Predictions for the redshift distribution of quasars at the soft band flux limit of the Chandra ELAIS deep survey.

from deep X-ray surveys (Hasinger 1998) suggest the space density may stay constant out to $z \sim 5$. Further discussion can be found in Almaini *et al.* (1999). The models illustrated (figure 3.3) display the case for a quasar population that decreases exponentially beyond a redshift of 2.7 (lower line) and one that stays constant out to a redshift of 5. Surveys with Chandra (as displayed) may be deep enough to distinguish between these models. Predictions for the redshift distribution of quasars down to the expected flux limit of the Chandra ELAIS deep survey are displayed in figure 3.4. There is a large difference between the models at redshifts of ~ 4 - 5. Once redshifts have been identified for quasars in this survey, it should be possible to clearly distinguish between the two models.

The X-ray counts were converted to number count predictions in the infrared at a wavelength of 15μm (see appendix B). In order to do this I have made use of the X-ray to IR flux ratio for radio quiet quasars given by Green *et al.* (1992). As displayed in figure 3.1, this ratio agrees very well with the SED of Elvis *et al.* (1994) at 12μm,

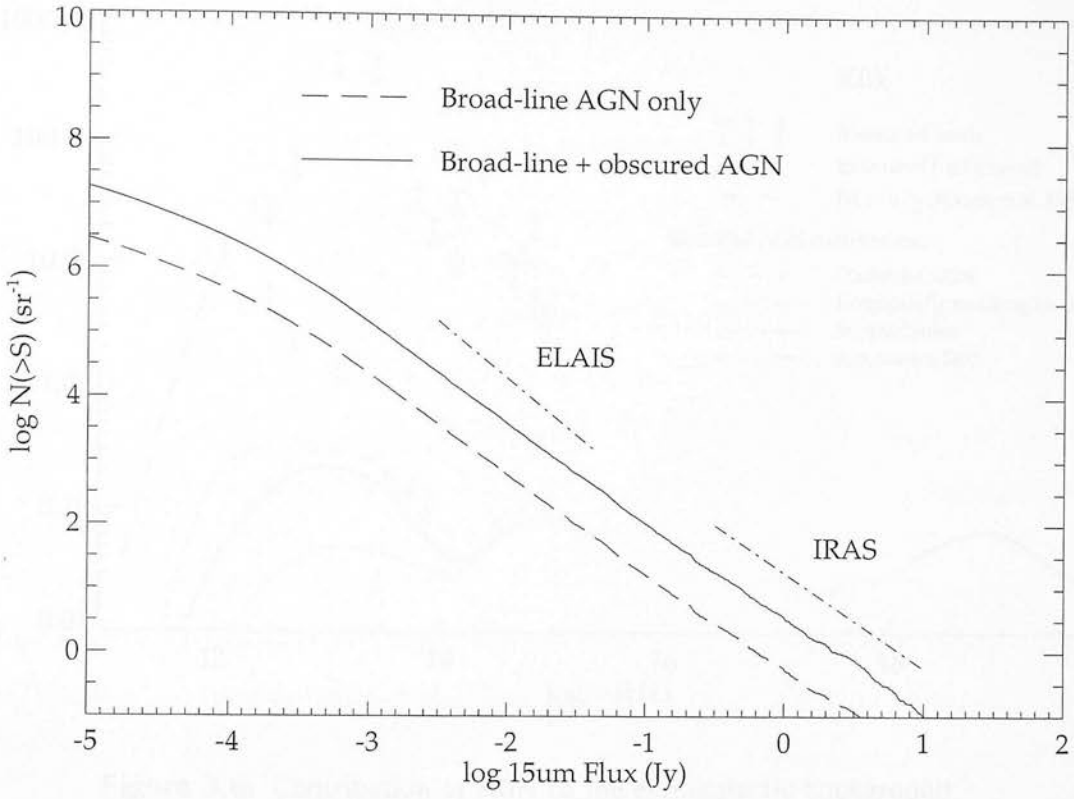

Figure 3.5: AGN number count predictions for the ELAIS 15μm survey.

but diverges at longer wavelengths. The ELAIS and IRAS mid-infrared extragalactic source counts (Serjeant *et al.* 2000) are displayed on the plot (figure 3.5) for comparison. The unobscured population should only contribute a few percent of the counts found by ELAIS. Taking into account the obscured population, this figure rises to 20 - 25%. These sources will thus have an X-ray counterpart observable with Chandra in the upcoming deep surveys.

3.6 Submillimetre to X-ray background

The contribution to the background at a particular wavelength is found by integrating over the flux from all sources. The equations used can be found in appendix C. Figure 3.6 displays the predicted background for four separate models explained below. Measurements of the observed submillimetre to optical background are taken from Hauser *et al.* (1998)

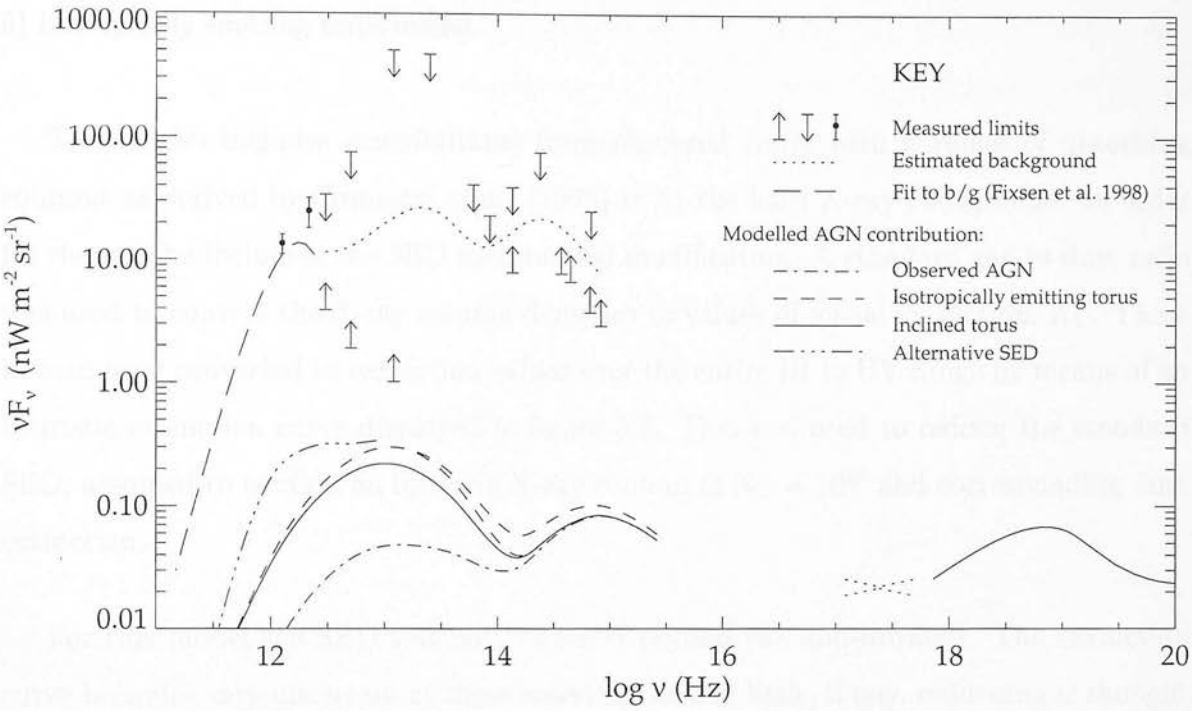

Figure 3.6: Contribution of AGN to the extragalactic background.

and references therein. Measurements in the ROSAT (0.5-2keV) band are from Hasinger (1992). A solid line displays measurements of the hard X-ray background (Gruber 1992) as fitted with contributions from obscured AGN by Comastri *et al.* (1995).

The break in the model predictions between the UV and the soft X-ray is a consequence of the lack of data on quasar SEDs at these wavelengths. Virtually all emission beyond the Lyman edge is absorbed in the interstellar medium of our own galaxy and in the quasar host.

The four models were constructed as follows:

i) Observed AGN

This is the background contribution from broad-line AGN only, as included in the luminosity function of Boyle *et al.* (1994). The unmodified SED of Elvis *et al.* (1994, as displayed in figure 3.1) is used to derive flux ratios.

ii) Isotropically emitting torus model

This model includes contributions from obscured AGN with a range of absorbing columns as derived by Comastri *et al.* (1995) to fit the hard X-ray background. In order for these to be included, the SED used needed modification. A standard gas-to-dust ratio was used to convert the X-ray column densities to values of visual extinction, A_V. These in turn were converted to extinction values over the entire IR to UV range by means of an heuristic extinction curve displayed in figure 3.2. This was used to redden the standard SED, assumed to contain an intrinsic X-ray column of $N_H = 10^{20}$ and corresponding dust extinction.

For this model the SED was not reddened beyond the mid-infrared. The extinction curve becomes very uncertain at these wavelengths and little, if any, reddening is thought likely to occur. The cut-off was chosen at a possible torus component of the SED, as modelled by Pier & Krolik (1993) for NGC 1068. The torus component has been chosen to remain constant, independent of absorbing column density and thus perhaps, viewing angle (i.e. an isotropically emitting torus).

The reddened SEDs for each column density were added to the standard 'unobscured' SED in the correct ratios, in order to obtain the combined spectral energy distribution for all AGN. This was then used to calculate the background.

The background calculations were repeated using a gas-to-dust ratio an order of magnitude larger. This is displayed as the higher of the two dashed lines at UV to IR wavelengths.

iii) Inclined torus model

This model differs from the previous one in that emission from the torus component is assumed to be dependent on viewing angle. Pier & Krolik (1992) calculated the infrared spectral properties of a model AGN torus. They found that face-on tori are $\sim$ an order of

magnitude brighter than edge on tori, due to the direct line of sight to the hot inner edge of the torus. Assuming that the density of the absorbing column is proportional to the viewing angle, heavily absorbed objects would thus be expected to emit relatively little in the infrared.

For this model I have approximated to a torus geometry, as used by Pier & Krolik (1993) to fit the spectral emission from NGC 1068, in order to calculate the dependence of viewing angle on column density. This can only be a rough approximation. If the geometry actually remained constant from AGN to AGN, we would be able to infer the distribution of column densities from a random distribution of viewing angles. (Note, it is possible that a mean torus geometry could be inferred from the distribution of absorbing columns modelled by Comastri *et al.*).

For the unobscured SED I have assumed that the face-on torus spectrum of Pier & Krolik contributes 100% of the emission at $10\mu m$. For the SEDs of the obscured objects I have used the tori spectra relevant for the derived viewing angle. The combined SED is therefore somewhat lower than that used for the isotropic torus model described above. The background derived from this is thus lower by a similar amount.

iv) Alternative SED

The motivation for this model stems from the fact that quasar SEDs are very uncertain at far-infrared and submillimetre wavelengths. As discussed in section 3.3, the discrepancy in SEDs for different samples of AGN indicate there may be a strong luminosity dependence. The Elvis *et al.* (1994) sample consisted of relatively high luminosity quasars for which far-infrared data was scarce. This model uses an SED derived from a much larger sample of far-infrared data, and may be more representative of the total population at these wavelengths.

The model uses the X-ray to IR flux ratio for radio quiet quasars from Green *et al.* (1992). The flux conversion factors are as used for the IR number count predictions

(appendix B). The X-ray to IR ratio is combined with the 12 - 60μm slope from the same paper and a determination of the far-infrared/submillimetre SED from D. H. Hughes (private communication). This SED is assumed to remain unaltered for obscured quasars, and thus a simple conversion factor of 5.4:1 (Comastri *et al.* 1995) is used to obtain the total emission from AGN.

3.7 Discussion

These models may still not contain the total contribution of AGN to the cosmic background radiation. Many recent papers (e.g. Maiolino *et al.* 1998) have drawn attention to the existence of a large number of AGN with X-ray absorbing columns $N_H > 10^{24.5}\mathrm{cm}^{-2}$. At these densities the gas will become optically thick to Compton scattering and virtually no X-ray emission will get through. AGN obscured by 'Compton thick' clouds would thus not contribute at all to the X-ray background and would not appear in these models. Given the ratios found by Maiolino *et al.*, the predicted backgrounds could increase by $\sim 50\%$.

A number of papers (Archibald *et al.* 2001b, Silk & Rees 1998, Fabian 1999) have suggested the existence of a large population of highly obscured AGN in the centres of newly forming galaxies at high redshift. These are inspired by the correlation found between black hole mass (M_{BH}) and galaxy bulge mass (e.g. Magorrian *et al.* 1998), now better defined as a correlation between M_{BH} and bulge velocity dispersion (Ferrarese & Merritt 2000, Gebhardt *et al.* 2000). These newly forming objects would likely be Compton thick from all viewing angles and would not fit in to the unified scheme. Emission from these obscured AGN would also contribute little to the X-ray background and are outside the scope of these models. Their contribution to the extragalactic background at IR / submillimetre wavelengths however may be significant.

A major discrepancy in the models presented is the nature of the background contribution beyond far-infrared wavelengths. This can be attributed to the uncertainty of

the SED in this region. Measurements in the far-infrared and submillimetre are only now beginning to be made with reasonable resolution and there is insufficient data to make large statistical samples. The data that is available has hinted at the existence of a luminosity dependence (see section 3.3). This may be due to a host galaxy contribution that becomes dominant at low luminosities, or perhaps a nuclear starburst surrounding the AGN (Fabian *et al.* 1998). Within samples of radio-loud galaxies there certainly appears to be a luminosity dependence in the relative numbers of broad-line to narrow-line AGN (Lawrence 1991). At the lowest luminosities, most radio-loud AGN are narrow-lined, while at the highest luminosities, only $\sim$ half. This indicates that the luminosity function for obscured objects may be completely different to the one used for this model. These observations, however, only apply to radio loud objects and it is unclear how this may relate to the much larger population of radio-quiet AGN.

McMahon *et al.* (1999) presented the first submillimetre observations of very high redshift ($z > 4$) quasars. These represent rest wavelength emission in the far-infrared at $\sim 150\mu m$. They find very high ratios for far-infrared to ultra-violet luminosity compared to the SED for radio quiet quasars of Elvis *et al.* (1994). This could indicate the presence of a large starburst component in these early galaxies, possibly advocating the need for a redshift dependence of the SED. This is further supported by Archibald *et al.* (2001a), who find the typical submillimetre luminosity of powerful radio galaxies is a strongly increasing function of redshift. Page *et al.* (2001) find a similar relation for X-ray selected radio-quiet quasars. In the near future, observations with SIRTF should be able to properly characterise the IR / far-IR properties of radio-quiet quasar SEDs as a function of both luminosity and redshift.

Due to the above factors, the background predictions presented here are at present only a lower limit. Still, it can be concluded that models to reproduce the X-ray background with integrated AGN emission are not constrained by the observed background at other wavelengths.

Note: Since this analysis was first performed more accurate measurements of the AGN

X-ray luminosity function have been made (e.g. Miyaji *et al.* 2000). However, little would be gained by a repeat of this modelling without further improvements to a number of the assumptions used. In particular, a luminosity dependence of the SED would have a large effect.

Chapter 4

X-ray Imaging

4.1 The beginnings of X-ray imaging

X-rays were discovered accidentally on the 8th of November 1895 when Wilhelm Conrad Roentgen noticed his cathode ray generator was causing a screen across the room to glow. Roentgen tested the properties of these new 'rays' by holding up materials in front of the screen and found the bones of his hand were clearly silhouetted in a faint outline of flesh.

It was many years before the true nature of X-rays as electromagnetic waves was uncovered. First, that they were diffracted when passing through a crystal (von Laue 1912), and then, that they can be reflected from a polished surface (Compton 1923), albeit at glancing angles. This requirement for 'grazing incidence' provided a major obstacle in developing an X-ray imaging system. Standard optical telescope designs can not be employed as X-rays are either absorbed or pass straight through any material they impinge at normal incidence. It was further shown (Jentzsch 1929) that any single mirror grazing incidence system will suffer from severe astigmatism.

A practical solution was first devised by Kirkpatrick and Baez in 1948. The problem of astigmatism was overcome with the use of 2 orthogonally crossed cylindrical mirrors,

each providing 1D focusing. This led to the production of the first 2D X-ray image. In the same year, an experiment carried by a V2 rocket discovered the Sun to be a bright source of X-rays (Burnight 1949). This marked the beginning of X-ray astronomy, though the use of grazing incidence optics was still some way off.

In 1951, Wolter greatly improved on the design of Kirkpatrick and Baez. While working on the design for an X-ray microscope, he showed that a true image over an extended field of view can be formed by glancing reflections off a paraboloid/hyperboloid or paraboloid/ellipsoid combination of coaxial and confocal mirrors. The Wolter design is now the most widely used in X-ray telescopes, although it was almost a decade before Giacconi & Rossi first suggested the use of grazing incidence optics for this purpose.

In the 1960s X-ray astronomy finally took off. The first X-ray image of the Sun was taken with the use of a pinhole camera (Chubb *et al.* 1961). In 1962 an experiment by Giacconi *et al.* carrying a Geiger counter on a sounding rocket discovered the first non-solar celestial X-ray sources. These turned out to be the diffuse X-ray background and the low mass binary system Scorpius X-1. Soon afterwards, in 1963, the first grazing incidence telescope (Wolter type) was used to record pictures of the Sun on photographic film.

The next milestone to be attained came with the launch of Skylab in 1973 carrying the telescopes S-054 (Vaiana *et al.* 1977) and S-056 (Underwood *et al.* 1977) which achieved a resolution of a few arcseconds. These were surpassed when the Einstein observatory (originally HEAO-B) was placed into orbit in 1978. The four nested shells in a Wolter type I configuration provided a massive leap forward in collecting area. The detectors included an efficient imaging proportional counter and a high-resolution (3″ FWHM) channel plate device.

In May, 1983 EXOSAT was launched into a highly eccentric orbit with an apogee of 200,000 km. This allowed up to 80 hours of uninterrupted exposures with its two Wolter type I telescopes. The variability of X-ray sources could be studied continuously

for the first time. The improvement in X-ray telescopes continued with ROSAT and now Chandra and XMM-Newton, which provide us with unprecedented collecting area and resolving power. The field of X-ray astronomy is enjoying a wealth of high quality data that looks set to continue for the foreseeable future.

4.2 X-ray telescope configurations

The critical angle for total external reflection of X-rays from materials composed of heavy elements is approximately:

$$\alpha_c = 69.4\frac{\sqrt{\rho}}{E} \tag{4.1}$$

where α_c is in arcminutes, ρ is the mass density of the reflecting material in g cm^{-3} and E is the X-ray energy in keV (Aschenbach, 1985). This gives a critical angle of around 1° for X-rays of a few keV. For incidence angles greater than this, the X-rays will be absorbed by the mirrors.

The requirement for grazing incidence reflections leads to telescope designs that are far removed from those used at longer wavelengths. Aberrations observed with grazing incidence optics are unlike those produced at more normal incidence and need to be dealt with in different ways. Further to this, the grazing incidence condition demands extremely low levels of surface roughness. The practicality of polishing the mirrors to the necessary standard must also be considered when choosing a design.

4.2.1 Kirkpatrick-Baez telescope

The first grazing incidence system to form a real image was proposed by Kirkpatrick and Baez, 1948. This consisted of a set of two orthogonal parabolas of translation as shown in Figure 4.1a. The first reflection focused to a line, which the second reflection then focused to a point. This was necessary to avoid the extreme astigmatism suffered by

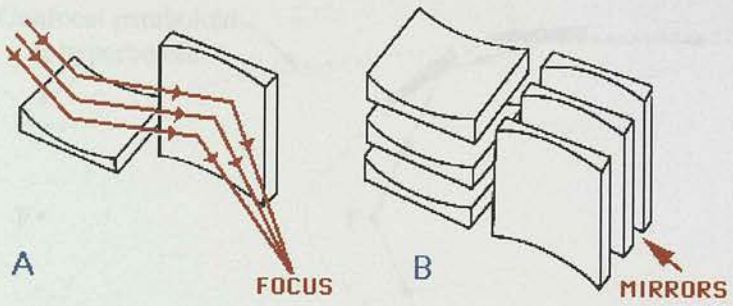

Figure 4.1: Kirkpatrick-Baez telescope configuration (from imagine.gsfc.nasa.gov).

a single mirror but was by no means free from geometric aberrations. The system was attractive for the ease of constructing the reflecting surfaces. These could be polished to a high level of accuracy as flat plates and then mechanically bent to the required curvature. In order to increase the aperture a number of mirrors could be nested together (figure 4.1b), although this introduces further aberrations.

4.2.2 Wolter telescopes

Wolter, 1952, set out to design an aplanatic system of grazing incidence mirrors that would be free of both spherical aberration and coma. This required that the 'Abbe sine condition' be fulfilled. For on-axis rays this occurs when the forward projection of the incident rays meet the backward projection of the focused rays on the surface of a sphere centred on the image focus. Wolter showed such a system could be produced using a combination of a paraboloid with either a hyperboloid or ellipsoid secondary. The three simplest designs are outlined in Figure 4.2 and are known as Wolter types I, II and III.

In each of the three types of Wolter telescope, the mirrors are arranged in a coaxial configuration and share a common focus. For the type I system, reflections are off the internal surface of a paraboloid and hyperboloid in a simple configuration that lends itself to nesting several mirrors inside one another. For this reason, Wolter type I systems are the most widely used in astronomical telescopes.

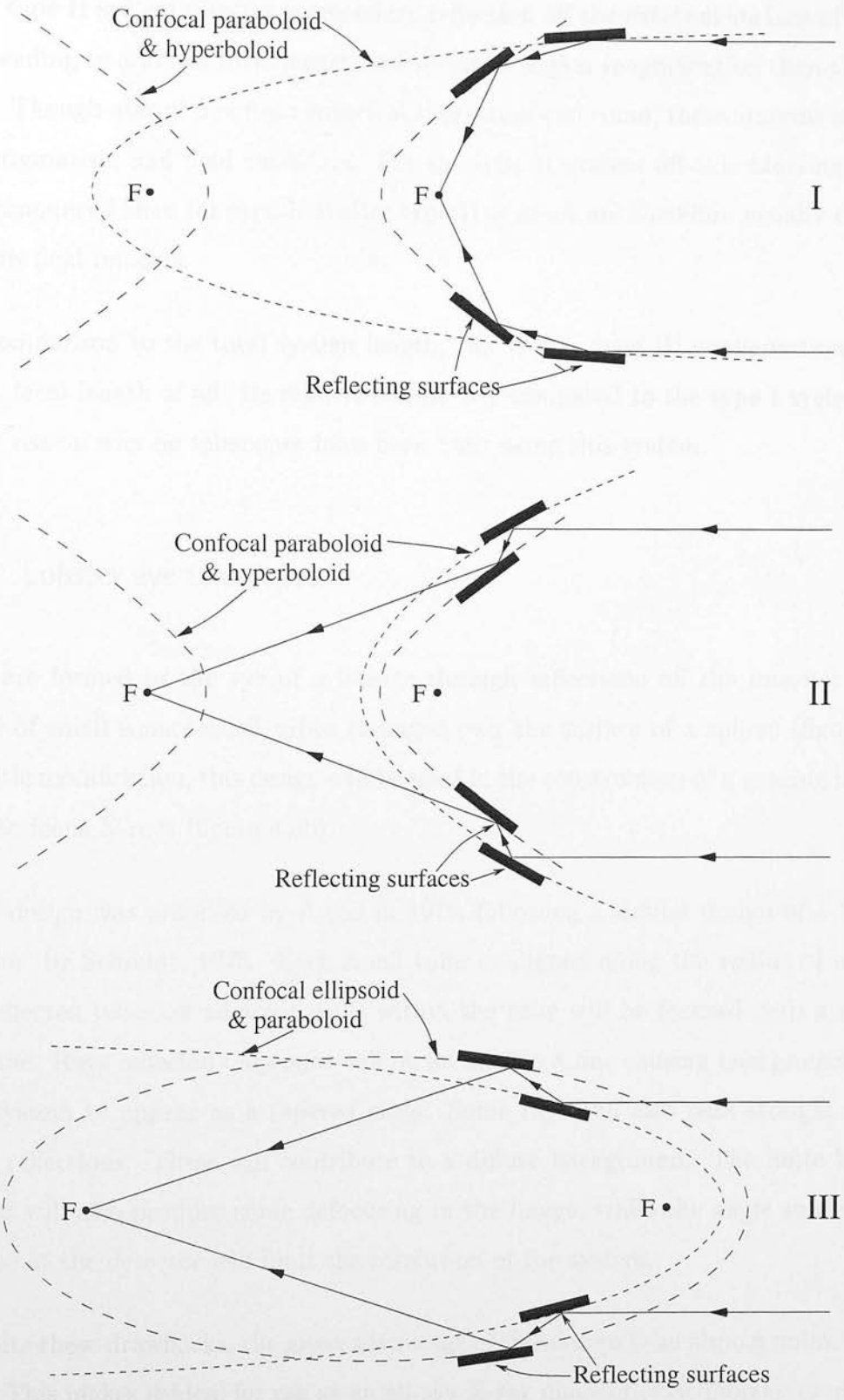

Figure 4.2: Wolter grazing incidence imaging systems, types I - III.

The type II system involves a secondary reflection off the external surface of a hyperboloid leading to a longer focal length and therefore higher magnification than the type I system. Though almost free from spherical aberration and coma, these systems still suffer from astigmatism and field curvature. For the type II system off-axis blurring is much more pronounced than for type I. Wolter type II systems are therefore usually employed as narrow field imagers.

In comparison to the total system length, the Wolter type III configuration has the shortest focal length of all. Its relative complexity compared to the type I system is the primary reason why no telescopes have been built using this system.

4.2.3 Lobster eye telescopes

Images are formed in the eye of a lobster through reflections off the internal walls of a lattice of small square-sided tubes arranged over the surface of a sphere (figure 4.3a). With little modification, this design can be used in the construction of a grazing incidence system to focus X-rays (figure 4.3b).

This design was proposed by Angel in 1979, following a similar design of a 'focusing collimator' by Schmidt, 1975. Each small tube is aligned along the radius of a sphere. A ray reflected twice off adjacent walls within the tube will be focused onto a spherical focal plane. Rays reflected only once will be focused to a line causing background images in this system to appear as a tapered cross. Some rays will also pass straight through with no reflections. These will contribute to a diffuse background. The finite height of the tubes will also produce some defocusing in the image, while the angle subtended by each tube at the detector will limit the resolution of the system.

Despite these drawbacks, the great advantage of this design is an almost unlimited field of view. This makes it ideal for use as an all-sky X-ray monitor (Priedhorsky *et al.* 1996). To date, no X-ray telescopes have been built using lobster-eye optics, principally due to

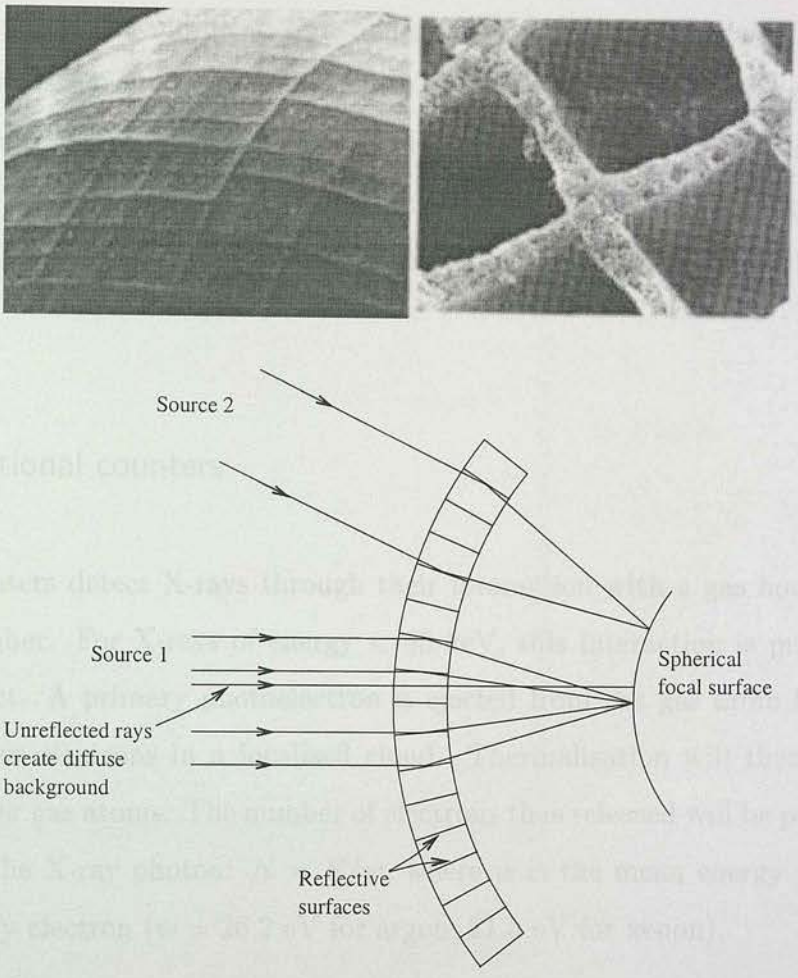

Figure 4.3: The 'Lobster-eye' imaging system (from www.src.le.ac.uk/lobster).

the difficulty in constructing the reflective tubes. However, improvements in multichannel plate technology has led to a proposal for a lobster-eye X-ray telescope to be placed on the International Space Station (Fraser *et al.* 2000).

4.3 X-ray detectors

By whichever method X-rays are focused or collimated their properties must be measured on arrival at the X-ray detector. The quality of the X-ray data will depend on the performance of the detector in a number of areas, namely: spatial resolution and

extent, temporal resolution and 'dead-time', energy resolution and bandwidth, quantum efficiency, spurious background rate and the overall stability of these characteristics with time. A number of different types of X-ray detector exist, optimised for best performance in one or more of these areas. The following sections describe three of the most common types of detector used on space-borne X-ray telescopes. Further details can be found in Fraser (1989).

4.3.1 Proportional counters

Proportional counters detect X-rays through their interaction with a gas housed within a windowed chamber. For X-rays of energy < 50 keV, this interaction is primarily the photoelectric effect. A primary photoelectron is ejected from the gas atom followed by a number of Auger electrons in a localised cloud. Thermalisation will then cause the ionisation of further gas atoms. The number of electrons thus released will be proportional to the energy of the X-ray photon: $N = E/w$, where w is the mean energy required to release a secondary electron ($w = 26.2$ eV for argon, 21.5 eV for xenon).

The presence of this electron cloud is eventually measured through an arrangement of electrodes. This usually consists of a uniform low-field 'drift region' where the X-rays are absorbed, and a high-field 'avalanche' region near to the anode. When the charge cloud reaches the avalanche region the electrons are accelerated sufficiently to ionise further gas atoms. The resulting pulse of charge onto the anode will have been amplified by a factor dependent on the geometry of the electrodes (e.g. ROSAT PSPC has a gain of $\sim 5 \times 10^4$). This can then be measured and the energy of the original X-ray photon simply derived. The energy resolution is constrained by the intrinsic variance in the number of electrons produced in the original charge cloud. This depends on the 'Fano' factor (F) of the gas: $\sigma_N^2 = FN$ where F ~ 0.17 for argon and xenon.

Position information is often provided through the signal induced on a cathode grid. Spatial resolution is constrained by the extent to which the charge cloud diffuses laterally

within the drift region. This is heavily dependent on the number of electrons within the cloud. Timing resolution is governed by the anode-cathode spacing and the positive ion mobility, usually limiting resolution to the microsecond level.

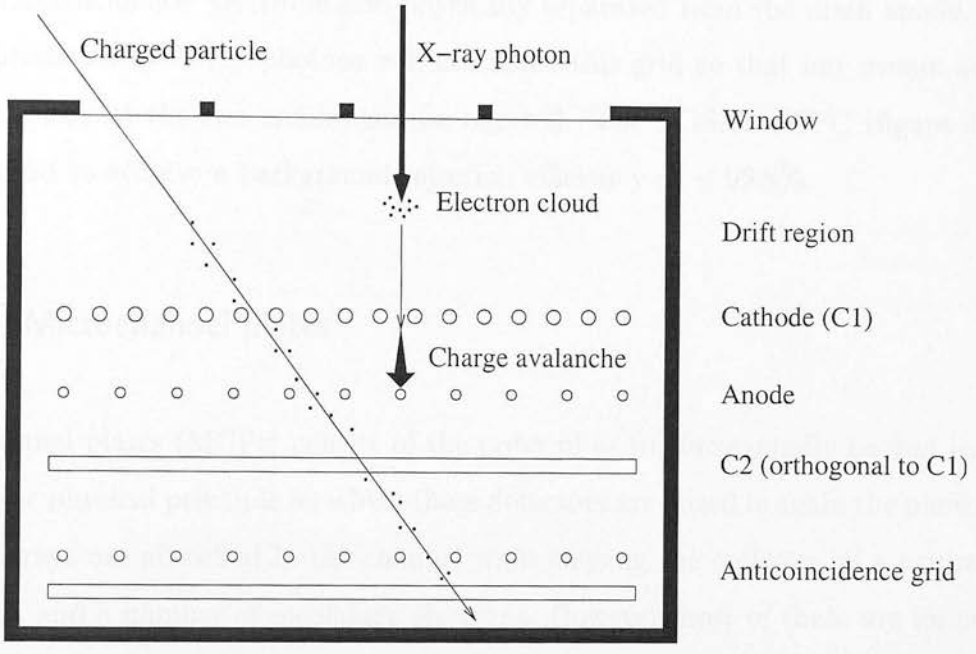

Figure 4.4: Schematic cross-section of the ROSAT position-sensitive proportional counter (PSPC). The counter gas is a mixture of 65% argon, 20% xenon and 15% methane. Energy resolution ($\Delta E/E$) is $42/E^{1/2}$% with a bandwidth of 0.1 - 2 keV. Spatial resolution ranges from 20 - 50 arcsec for energies between 1.5 and 0.2 keV on axis. This increases to $\sim$ 4 - 5 arcmin, 50 arcmin off axis. The field of view is $\sim 1.6°$.

The quantum efficiency of a gas proportional counter is dependent on the transmission properties of the window (including the support mesh) and the absorption properties of the gas. Photoelectric absorption follows the general relation $Z^4/E^{8/3}$ in regions not dominated by absorption edges. Therefore windows are made of material with low atomic number (Z), generally plastics coated with a thin metallic layer to stop optical photons and provide electrical conductivity. Below 1 keV the quantum efficiency is dominated by absorption in the window, principally the C K absorption edge at 0.28 keV which generally reduces the transmission to zero. At higher energies the quantum efficiency is dominated by the optical thickness of the gas. Mixtures of noble gases are often employed to maintain the absorption cross-section over a range of energies.

Spurious background events can be caused by charged particles passing through the chamber leaving a trail of electron-ion pairs. These can be distinguished from X-ray events due to the different rise-time of the resulting pulse. A more robust method makes use of an 'anticoincidence' electrode grid physically separated from the main anode. Charge clouds produced by X-ray photons will not reach this grid so that any events occurring simultaneously at the two anodes can be rejected. The ROSAT PSPC (figure 4.4) uses this method to achieve a background rejection efficiency of $\sim 99.8\%$.

4.3.2 Microchannel plates

Microchannel plates (MCPs) consist of the order of $\sim 10^7$ hexagonally packed lead glass tubes. The physical principle on which these detectors are based is again the photoelectric effect. X-rays are absorbed in the channel walls causing the emission of a primary photoelectron and a number of secondary electrons. However most of these are immediately recaptured by the lead glass medium and the most probable number of electrons escaping into the channel is just one. This is practically independent of X-ray energy and leads to almost a complete lack of energy resolution for uncoated microchannel plates. Once an electron has emerged into the evacuated tube it is accelerated along its length by an applied electric field. The kinetic energy gained allows the electron to release a number of secondary electrons on collision with the channel walls. The resulting cascade of electrons emerge from the back of the plate and impinge upon a charge detector (often a crossed wire grid) which measures the pulse shape and position of the event.

Many microchannel plate detectors such as the Chandra High Resolution Camera (HRC), use a chevron arrangement of two plates (see figure 4.5). Here, the axis of the plate tubes are canted at an angle of 6° to the optical axis (and the applied electric field) though in opposite directions for the two plates. The primary reason for this is to reduce positive ion feedback. Residual gas atoms within the tube may be collisionally ionised and proceed back up the tubes under the influence of the electric field. The bias angle of the tubes ensures these ions will reach the walls before they have gained enough kinetic

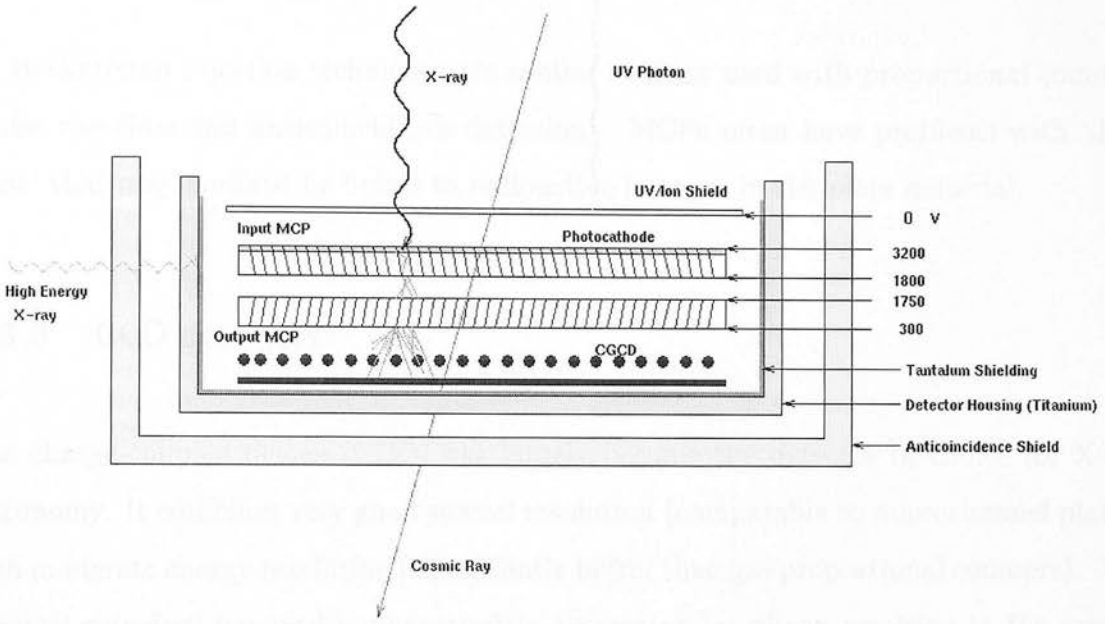

Figure 4.5: A schematic of the Chandra HRC microchannel plate detector (from http://cxc.harvard.edu).

energy to release further electrons and produce an unwanted cascade event.

The spatial resolution of an MCP detector is fundamentally limited by the channel diameter ($10\mu m$ for the HRC-I). However, this is degraded through a spreading of the electron cascade in the inter-plate gap to a number of channels in the second plate. At X-ray energies above $\sim$ 5 keV, the X-ray photon penetrates the lead glass channel walls to release photoelectrons in neighbouring channels further degrading the PSF. For the Chandra HRC intrinsic spatial resolution is $\sim 20\mu m$ ($\sim$ 0.4 arcsec) with a field of view of $\sim 30 \times 30$ arcmin. Time resolution is also extremely good (16 μsec for the HRC) and usually only limited by the telemetry rate.

Quantum efficiency for uncoated MCPs is low (1 - 10%) and decreases towards higher energies. To improve efficiency the channel walls are coated with a material of high photo-electric yield. This coating may also allow for the release of more than one photoelectron leading to some measure of energy resolution. At 1 keV the Chandra HRC has a quantum efficiency of 30% and a spectral resolution $\Delta E/E \sim 1$. Quantum efficiency at soft energies

is limited by the transmission of the UV/Ion shield.

Background rejection techniques are similar to those used with proportional counters (pulse rise-time and anticoincidence detection). MCPs often have problems with 'dark noise' that may perhaps be linked to radioactive isotopes in the plate material.

4.3.3 CCD detectors

The charge-coupled device (CCD) has largely become the detector of choice for X-ray astronomy. It combines very good spatial resolution (comparable to microchannel plates) with moderate energy resolution (significantly better than gas proportional counters). The physical principal involved is photoelectric absorption by silicon resulting in the release of a proportional number of electrons, analogous to the process within a gas proportional counter. Beyond that the physical properties and operation of a CCD detector are somewhat different. A detailed description of scientific charge-coupled devices can be found in Janesick (2001).

Theory and design

Detectors such as the Chandra Advanced CCD Imaging Spectrometer (ACIS) use what are known as 'buried channel CCDs'. The basic structure of this type of CCD is shown in figure 4.6. The semiconducting material (usually silicon) is divided into a number of regions of differing conductivity by introducing 'dopants'. Neutral silicon contains four electrons in the valence band. If these electrons are given enough energy they may cross the band gap ($E_g = 1.12$ eV) and enter the conduction band, leaving a 'hole' in the valence band. Introduction of a pentevalent atom such as phosphorus supplies an extra valence electron in an energy level just below the conduction band ($\delta E = 0.05$ eV). At temperatures above $\sim$ 70 K these electrons are completely thermally ionised. Silicon doped with phosphorus is known as 'n-type' material and contains an over-density of free

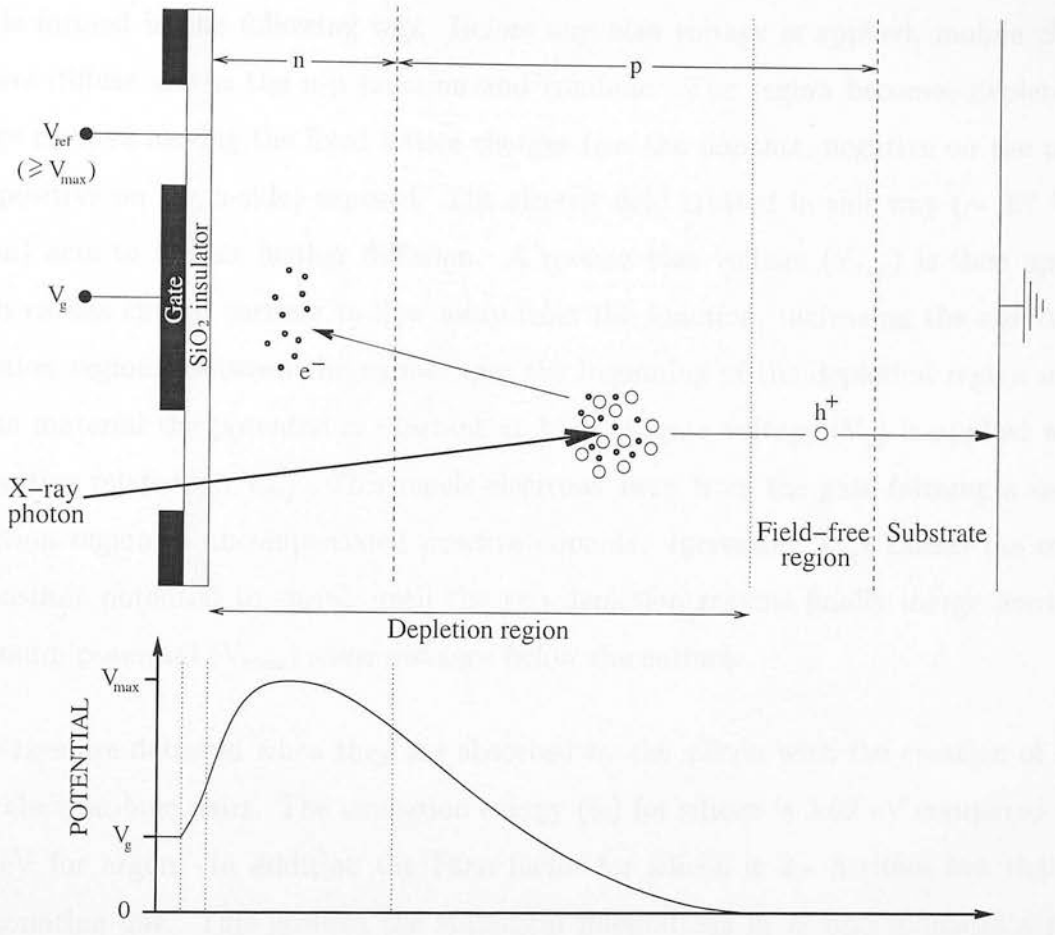

Figure 4.6: Structure and potential well of a buried-channel CCD.

electrons equivalent to the donor impurity density. In contrast 'p-type' material is doped with trivalent atoms such as boron or aluminium. These provide energy levels just above the valence band which 'accept' electrons thermally excited from the surrounding silicon. This creates an over-density of holes.

Layers of p and n-type material are created on one side of a less refined silicon substrate. The outer surface is then oxidised to form a thin insulating layer. The electrode or gate material is then deposited on top of this. The purpose of the CCD structure is to store charge beneath the gate. Charge can become trapped at the Si-SiO_2 interface which causes problems when the CCD is read out. To eliminate this problem voltages are applied across the n-p structure in order to produce a potential maximum below the surface. Charge then collects within this 'buried channel' (see figure 4.6). The potential

well is formed in the following way. Before any bias voltage is applied, mobile charge carriers diffuse across the n-p junction and combine. The region becomes depleted of charge carriers leaving the fixed lattice charges (*i.e.* the dopants, negative on the p-side and positive on the n-side) exposed. The electric field created in this way ($\sim$ 0.7 V for silicon) acts to inhibit further diffusion. A reverse bias voltage (V_{ref}) is then applied which causes charge carriers to flow away from the junction, increasing the size of the depletion region. Between the surface and the beginning of the depletion region in the n-type material the potential is constant at V_{ref}. A gate voltage (V_g) is applied which is negative relative to V_{ref}. This repels electrons away from the gate forming a second depletion region of uncompensated positive dopants. Increasing V_{ref} causes the region of constant potential to shrink until the two depletion regions finally merge leaving a maximum potential (V_{max}) some distance below the surface.

X-rays are detected when they are absorbed by the silicon with the creation of $N = E/w$ electron-hole pairs. The ionisation energy (w) for silicon is 3.62 eV compared with 26.2 eV for argon. In addition the Fano factor for silicon is 2 - 3 times less than for any counting gas. This governs the statistical fluctuations in N and indicates a great improvement in energy resolution over gas proportional counters. The electrons liberated by the X-ray photon are confined by the potential well to a small volume beneath the gate.

Operation

Once the charge has been collected its position, energy and time of arrival must be determined. The gate structure on the surface of the CCD is designed to produce well-defined pixels and efficient read-out of charge. The electrodes are arranged in thin parallel strips where three adjacent electrodes constitute the pixel width. The centre electrode is set to a high potential (V_g) while the outer electrodes are negatively biased. The other pixel dimension is set by 'channel stops', heavily doped p-type implants which are negatively charged once depleted.

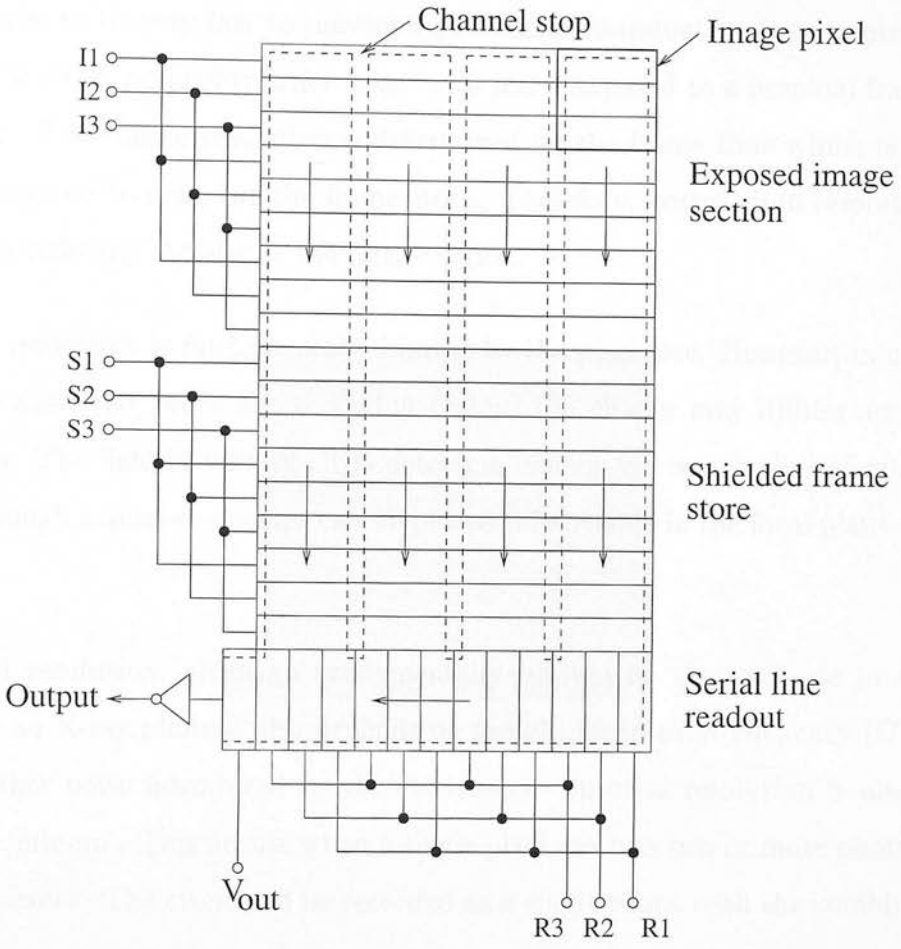

Figure 4.7: Readout of a frame transfer CCD (such as Chandra ACIS). This schematic displays parallel charge transfer through clocking of the image (I) and store (S) gate voltages. The frame store is read out line by line by clocking the readout voltages (R).

An integration begins once the gate voltage is applied. Electrons released through X-ray absorption collect beneath the gate. At the end of the allotted integration time, the accumulated charge is quickly transferred to a shielded 'frame store'. The transfer is achieved by reducing the voltage on the gate electrode while the voltage on the neighbouring electrode is raised. By cyclically varying the voltages, stored charge over the entire imaging region is read out in parallel (figure 4.7). The frame store is then transferred to a serial readout line-by-line, which feeds into an output amplifier.

The imaging region of the CCD is continuously exposed to X-rays so that a second integration proceeds while the first is being read from the frame store. The parallel

transfer needs to be very fast to prevent significant contamination from exposure during readout. For ACIS parallel transfer takes $\sim$ 40 ms, compared to a nominal frame time of 3.2 seconds. The timing resolution is determined by the frame time which is limited by the time required to read out the frame store. Therefore, better time resolution can be achieved by reducing the size of the image region.

Spatial resolution is fundamentally limited by the pixel size. However, in cases where X-rays are absorbed below the depletion region, the charge may diffuse across two or more pixels. The field of view of CCD detectors cannot yet match that of microchannel plates, although a number of chips can be placed side-by-side in the focal plane to increase coverage.

Spectral resolution, although fundamentally limited by the variance in the charge released by an X-ray photon, also depends on the charge transfer efficiency (CTE) of the chip and other noise introduced by the electronics. Spectral resolution is also seriously affected by 'pile-up'. This occurs when a single pixel receives two or more photons during a single exposure. The event will be recorded as a single count with the combined energy of the photons.

4.4 Characteristics of Chandra ACIS data

The Chandra X-ray Observatory was launched on July 23, 1999, into a highly elliptical orbit. With a steady apogee of $\sim$ 140,000 km and a perigee of $\sim$ 10,000 km after launch (rising to $\sim$ 23,000 km as of September 2001), the satellite spends $>$ 75% of the time well above the radiation belts. The orbital period is 63.5 hours allowing continuous observations of $\geq$ 170 ks.

The X-ray telescope is of a Wolter type I design. The four nested pairs of mirrors have a total aperture of 1145 cm^2 and a focal length of 10 m. The two focal-plane science instruments are the Advanced CCD Imaging Spectrometer (ACIS) and the High

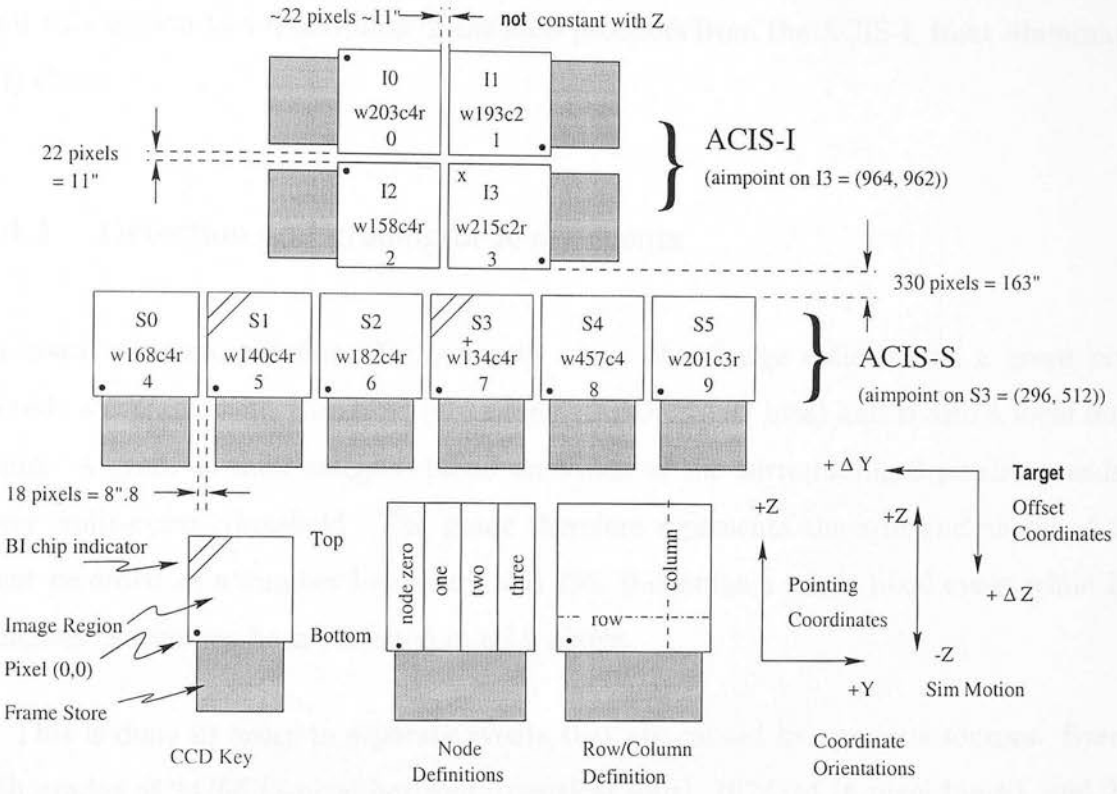

Figure 4.8: Schematic of the ACIS focal plane, looking along the optical axis from the direction of the source (-X). From http://cxc.harvard.edu.

Resolution Camera (HRC). Here, I will consider data taken with the Chandra ACIS detector.

The X-ray data delivered from ACIS is a product of the true incident X-ray radiation, the response of the High Resolution Mirror Assembly (HRMA), the efficiency of the CCD detectors, and the pre-processing performed. This section outlines some important characteristics of this data. A more complete description can be found in the 'Chandra Proposers' Observatory Guide' available from the Chandra X-ray Centre (values quoted are from this reference unless otherwise stated).

The layout of the ten 1024 × 1024 pixel CCDs is displayed in figure 4.8. Any 6 chips may be operated simultaneously. If the 2 × 2 ACIS-I imaging array is used the aimpoint is nominally set to a point on the I3 chip close to the centre of the array. Data collected far from this aimpoint, such as on the ACIS-S chips will be out of focus. I will therefore

limit this section to a description of the data products from the ACIS-I, front illuminated (FI) chips.

4.4.1 Detection and grading of X-ray events

On-board processing defines X-ray events where the charge collected at a given pixel exceeds a certain event threshold (after removing the CCD bias) and is also a local maximum. A grade is then assigned based on which of the surrounding 8 pixels exceeds a lower 'split-event' threshold. The grade therefore represents the size and shape of the event recorded as a number between 0 and 255. 0 denotes a single pixel event while 255 indicates charge has been collected in all 9 pixels.

This is done in order to separate events that are caused by spurious sources. Events with grades of 24/66 (3-pixel horizontal/vertical split), 107/214 (6-pixel block), and 255 make up 97.7% of the 0.3 - 10 keV non X-ray background and are discarded on-board. All other grades are included in the telemetry stream along with event position in detector coordinates, event amplitude and arrival time. Pipeline processing on the ground then limits the data to an optimum standard set of grades.

4.4.2 Spatial resolution

The on-axis spatial resolution is limited by the CCD pixel size (24 μm or $\sim$ 0.492 arcsec square). The point spread function (PSF) is affected by the response of the nested mirror assembly, telescope aspect (pointing) errors, and the ACIS response function. Figure 4.9 displays the resulting on-axis PSF at a number of different energies.

The HRMA consists of 4 nested pairs of mirrors in a Wolter type I configuration. Aberrations intrinsic to this design and the effect of the different focal surfaces for the 4 mirrors results in a degradation of the PSF off-axis. The 4 flat ACIS-I chips are tilted

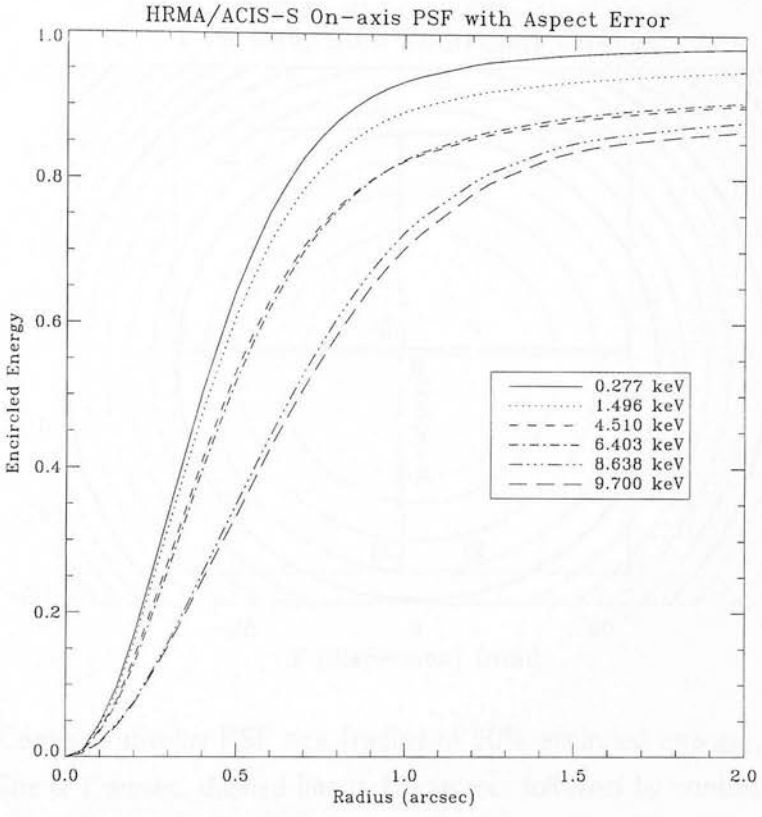

Figure 4.9: Simulated PSF for an on-axis point source as measured by the ACIS-S3 chip (will be almost identical to the ACIS-I response). From http://cxc.harvard.edu.

tangential to the curved focal plane which introduces further aberrations. The increase in PSF size with off-axis angle is displayed in figure 4.10. It should be noted that this effect is also energy dependent.

The Chandra X-ray Centre provide a 'PSF library' from which models of the PSF can be interpolated for a given position and energy.

4.4.3 Energy resolution

Prior to launch, the energy resolution for the ACIS FI CCDs ranged from $\sim$ 60 eV FWHM at 1 keV to $\sim$ 150 eV at 8 keV. The CCDs were later damaged by low energy protons from the radiation belts and the energy resolution has been degraded. The damage has affected

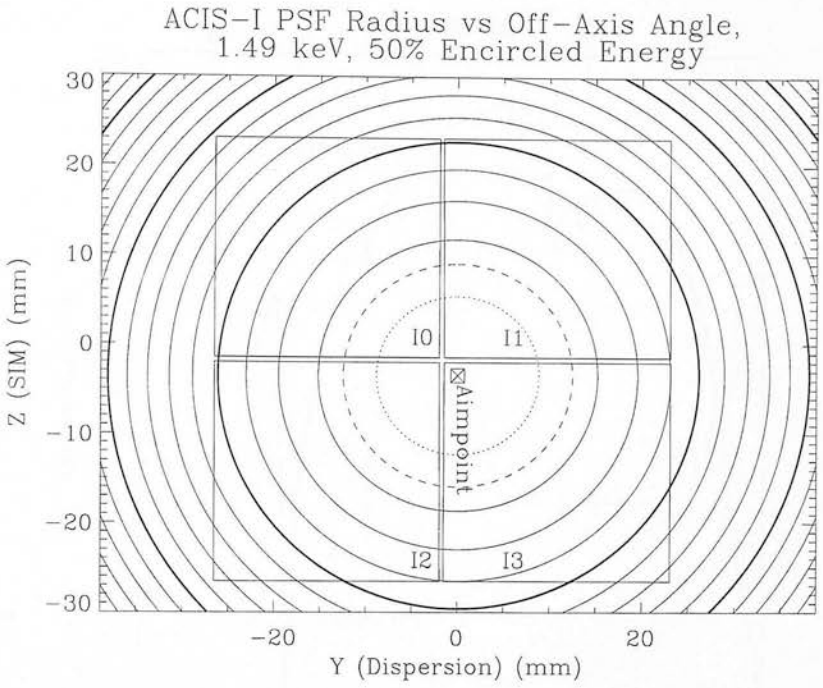

Figure 4.10: Contours display PSF size (radius of 50% encircled energy), with off-axis angle. Dotted line is 1 arcsec, dashed line is 1.5 arcsec, followed by contours at 1 arcsec intervals. Thick lines denote 5, 10, and 15 arcsec contours. From http://cxc.harvard.edu.

the charge transfer efficiency of the front illuminated CCDs so that energy resolution is now a function of row number. Close to the frame store pre-launch values still apply, while the energy resolution degrades by a factor of ~ 2 towards the opposite edge. Software is now available to model this effect and significantly improve the energy resolution.

4.4.4 Effective area

The geometric aperture of the HRMA is 1145 cm^2. However, the effective area at the detector is reduced by a number of factors. These are i) obstruction by supporting struts (less than 10%), ii) energy dependence of the mirror reflectivity, iii) transmission of the optical blocking filter and iv) quantum efficiency of the CCDs. The combined effect of these factors are displayed in figure 4.11. Off-axis dimming (vignetting) acts to reduce the effective area by $\sim 20\%$ for sources 10 arcmin from the aimpoint.

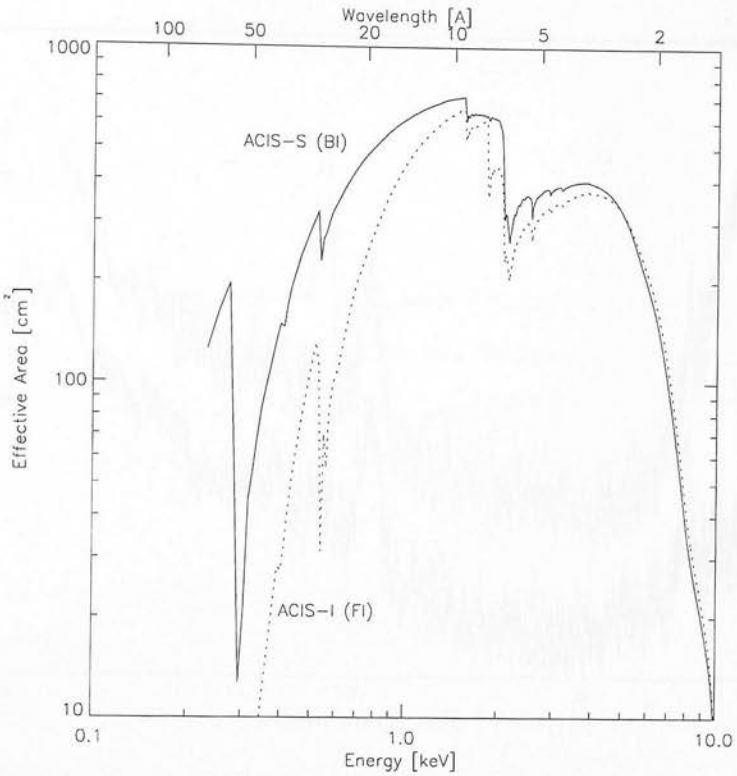

Figure 4.11: The HRMA/ACIS predicted effective area as a function of energy. Calculations are for a point source using the standard grade set. From http://cxc.harvard.edu.

4.4.5 Background properties

The total background count rate for Chandra ACIS-I standard grade data is very low. For the Chandra observation of the ELAIS N2 field the rate is 6 $\times 10^{-10}$ counts cm^{-2} s^{-1} pixel^{-1}, equivalent to 1 count over a $\sim$ 75 pixel ($\sim$ 18 square arcsecs) region for the entire 75 ks integration.

There are a number of different components to the background count rate. The diffuse X-ray background is primarily composed of unresolved sources and will effectively decrease as the integration time increases. The remaining component is referred to as the non X-ray background. This is principally cosmic ray induced events with a hard spectrum. Neutral particles and charged particles that have sufficient momentum to avoid deflection by the applied electric field leave a trail of charge in the detector that can usually be filtered out

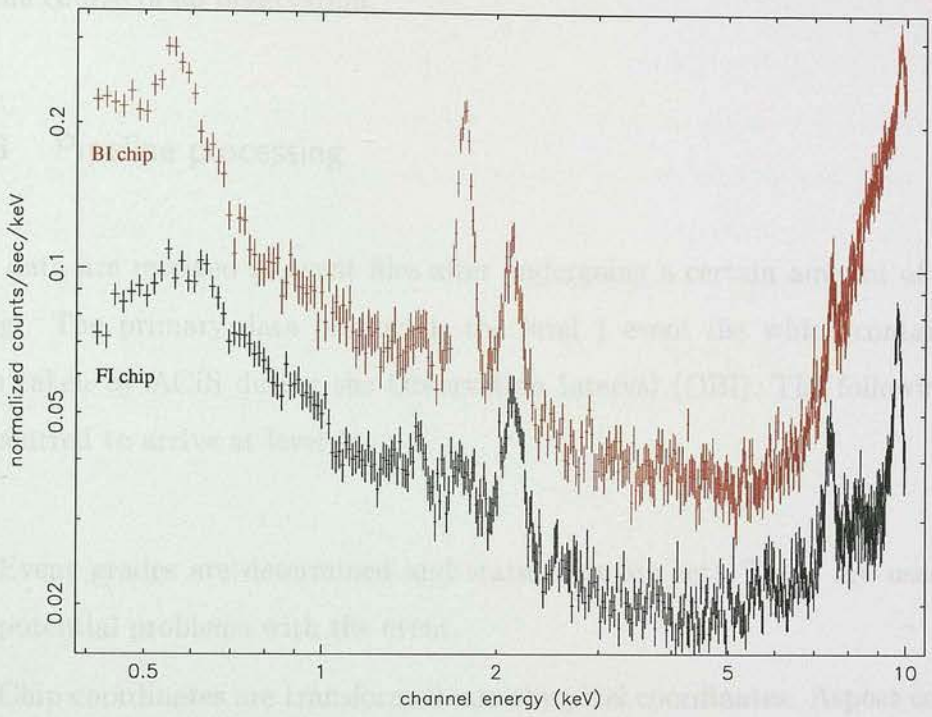

Figure 4.12: Quiescent background spectra for the BI chip S3 (red) and FI chip I3 (black). Data is for standard grades with an ACIS temperature of -90C. From http://cxc.harvard.edu.

by excluding certain grades. Photons with energies outside the X-ray bandpass will also add slightly to the background.

The quiescent background spectrum is shown in figure 4.12. Diffuse X-ray events dominate at low energies while the cosmic ray component becomes dominant above $\sim$ 5 keV. The background count rate is relatively stable except during periods of flaring activity. These are a significant problem for the back illuminated chips where the background may exceed 10 times the quiescent rate 5 - 15% of the time. This reduces to less than 1% of the time for the front illuminated chips of the ACIS-I array. The flares have a soft X-ray spectrum.

There is significant spatial variation in the background count rate. This is mainly due to the hard cosmic ray component. The 5 - 10 keV background can vary by more than 30% across a single chip. However, the spatial structure of the background remains stable

over the course of an observation.

4.4.6 Pipeline processing

ACIS data are received as event files after undergoing a certain amount of pipeline processing. The primary data product is the level 1 event list which contains all of the events taken by ACIS during the Observation Interval (OBI). The following processing has occurred to arrive at level 1:

- Event grades are determined and status bits are set. These are used to indicate potential problems with the event.
- Chip coordinates are transformed into sky pixel coordinates. Aspect corrections are made to account for spacecraft motion and instrument dither.
- The pulse invariant (PI) energy is calculated, correcting for gain variations and charge transfer inefficiency.
- Data is formatted into an event list and standard FITS header.

A level 2 event list is prepared with the following further processing:

- Multi-OBI observations are merged into a single event file.
- A good time interval (GTI) filter is applied to remove periods where no useful data was recorded.
- Events are filtered to include only the standard ACIS grade set.
- Further filtering removes events with non-zero status bits. This removes bad-pixels and 'problem' events such as cosmic ray afterglows.

Further data products are also prepared including bad-pixel lists, aspect offset files etc.

Cosmic ray afterglows

Cosmic rays can deposit large amounts of energy in front-illuminated chips which is not entirely removed on read-out. In these cases events are recorded in a number of consecutive frames for the same pixel. These events are flagged in the status bits and removed for level 2 event files, however a significant number of real X-ray events can also be flagged as afterglows for bright X-ray sources. For this reason, cosmic ray afterglow events should be reinstated when estimating the flux of an X-ray source.

4.5 Source detection with wavelets

Wavelets are oscillatory, scalable functions which are non-zero only within a limited spatial and Fourier regime. Their overall normalisation is zero. Wavelets used in source detection also exhibit vanishing moments. A wavelet (ψ) with M vanishing moments will obey the following equation:

$$\int_{-\infty}^{\infty} \psi(x) x^n dx = 0 \qquad n = 0, \ldots, M-1 \tag{4.2}$$

Integrating the product of such a wavelet with a polynomial of degree $\leq$ M - 1 will give zero. Therefore, correlating a wavelet function with a photon count image will only give significant values where the image undergoes high-order variations (i.e. in the vicinity of a source). The limited spatial and Fourier extent of a wavelet also makes it an excellent filter for characterising the size and shape of a source.

WAVDETECT is a source detection and characterisation algorithm developed by Freeman *et al.* (2002). The Marr or 'Mexican Hat' wavelet function is used which has a positive kernel similar in shape to a canonical PSF. The shape of this wavelet function is displayed in figure 4.13. The scale parameter (i) can be changed to 'stretch' the wavelet in the x-y plane. The Mexican Hat function has two vanishing moments indicating correlations with constant or linear functions will be zero.

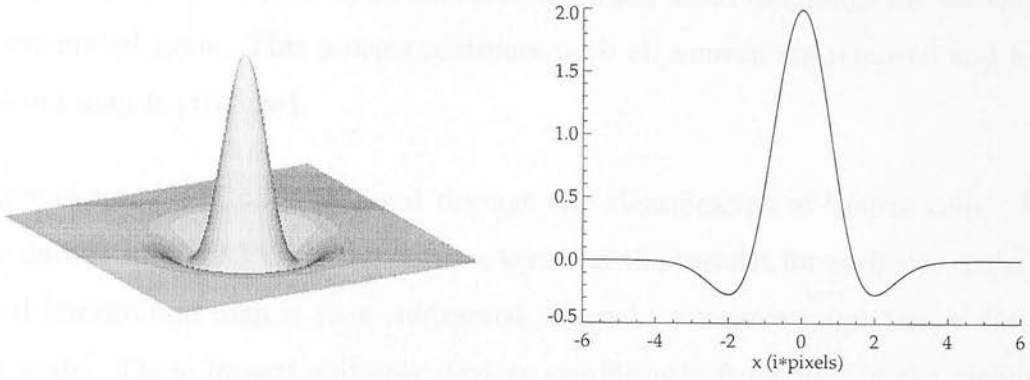

Figure 4.13: The 'Mexican Hat' wavelet function.

The first step in source detection is correlation of the image data with the wavelet function for a number of user defined scales. The 'correlation image' at a certain scale size replaces each pixel with the integrated product of the data and a wavelet centred on that pixel. Correlation values ($C_{i,j}$) are then used to determine whether a source is present at that pixel location. The detection threshold depends on the probability of obtaining a certain correlation value given the local background ($B_{i,j}$). These probabilities have been calculated by over 50,000 simulations which are sufficient to characterise the bulk of the probability distribution, but insufficient to assign probabilities to the most significant correlations. The threshold correlation value ($C_{o,i,j}$) is therefore defined as follows:

$$S_o = \int_{C_{o,i,j}}^{\infty} dCp(C|B_{i,j}) \tag{4.3}$$

where S_o is a user-defined threshold significance. Correlation values $C_{i,j} > C_{o,i,j}$ lead to the identification of source pixels. S_o can be given a value equal to the inverse of the number of image pixels, which would lead to an average detection of one false source over the full extent of an image.

The background value for each pixel ($B_{i,j}$) is found through an iterative process. Initially $B_{i,j}$ is estimated at each wavelet scale by correlating the data with the negative annulus of the 'Mexican Hat'. The background maps created will include contamination from sources that coincide with the wavelet annulus. These sources are identified through the method outlined above using the initial background map with S_o set high in order

to identify all possible sources. Once these are 'cleansed' from the image the background can be estimated again. This process continues until all sources are removed and a final background map is produced.

Source characterisation is achieved through the identification of 'source cells'. First, the raw data is smoothed using the positive kernel of the wavelet for each size scale. The corrected background map is then subtracted to create a 'source count image' for each wavelet scale. These images will only deviate significantly from zero in the vicinity of sources. Each of these islands in the image will contain one or more peaks and can be separated in to subislands divided by saddle points. For each identified source, an image is chosen that has been smoothed at a scale closest to the PSF size at that point. The subisland in which the correlation maximum resides is then identified as the source cell.

Source characteristics are identified using the raw data contained within the source cell and a corrected background map made by combining background estimates from each size scale. The smoothing procedure used to generate the source cells means that for isolated sources the cells will contain practically all of the source counts.

Chapter 5

The ELAIS Deep X-ray Survey

5.1 Introduction

The results of recent deep X-ray surveys reveal that almost the entire X-ray background can be resolved into discrete sources. The ROSAT Deep Survey (Hasinger *et al.* 1998) resolved 70 - 80% of the 0.5 - 2 keV background at a flux level of 1 $\times 10^{-15}$ erg s^{-1} cm^{-2}. Observations with Chandra and XMM-Newton are now pushing the detection limits even further. In particular, the unprecedented resolution of Chandra allows extremely deep observations that are not limited by source confusion. The Chandra Deep Fields (North, Brandt *et al.* 2001; South, Giacconi *et al.* 2001) have each accumulated 1 Msec of data reaching flux limits of 3 - 5 $\times 10^{-17}$ erg s^{-1} cm^{-2} in the 0.5 - 2 keV band. However, the greatest advances have been at higher energies where Chandra is now beginning to resolve the 2 - 8 keV background.

The majority of sources resolved by ROSAT were found to have spectra that were too steep to account for the flat spectrum of the hard X-ray background. Almaini *et al.* (1996) showed that towards fainter fluxes a new population emerged in the ROSAT data with intrinsically harder X-ray spectra. Chandra is now uncovering a large number

of hard spectrum sources, and the majority of the 2 - 8 keV background has been resolved. Over the flux range 2 $\times 10^{-16}$ to 10^{-13} erg s^{-1} cm^{-2} the contribution of resolved sources to the 2 - 8 keV background is 1.1 $\times 10^{-11}$ erg s^{-1} cm^{-2} deg^{-2} (Cowie *et al.* 2002). This translates to $\sim$ 65 - 85 per cent of the background as measured by Vecchi *et al.* (1999, Beppo-Sax) and Ueda *et al.* (1999, ASCA) respectively.

Early spectroscopic observations of these hard sources are finding most to be obscured AGN at $z < 1$ (Tozzi *et al.* 2001). In contrast, Type I AGN display softer X-ray spectra and cover a wider range in redshift. A considerable fraction of the hard X-ray sources are optically faint, probably due to obscuration, and provide challenging targets for spectroscopic identification.

There are still a number of unanswered questions relating to the properties of the hard X-ray populations at longer wavelengths. AGN with large X-ray absorbing columns do not always appear as Type II AGN in the optical (e.g. Maiolino *et al.* 2001). The relationship between gas and dust absorption in AGN remains unclear. It is also uncertain where the absorbed radiation may be re-radiated. Approximately $\sim$ 7 per cent of X-ray sources in the Chandra Deep Field North are submillimetre sources (Barger *et al.* 2001), however whether this is the result of reprocessed nuclear emission or due to a starburst component, is unknown. Almaini *et al.* (2001) find evidence for a strong angular cross-correlation between the X-ray and submillimetre populations. They suggest there may be an evolutionary sequence in these galaxies between the major episode of star-formation (submillimetre sources) and the onset of quasar activity (X-ray sources). To more fully understand the nature of these sources will require in-depth multi-wavelength studies of the X-ray source population.

We are conducting a deep X-ray survey with Chandra and XMM in two of the European Large Area ISO Survey (ELAIS) fields, N1 and N2. These high latitude fields were chosen for their low cirrus emission, and have a wealth of multi-wavelength data available. Both fields have been observed with ISO at 7, 15, 90, and 175 μm (Oliver *et al.* 2000), with the VLA at 1.4 GHz (Ciliegi *et al.* 1999, Ivison *et al.* 2002), and have

deep g′, r′, i′, H, and K imaging (Gonzalez-Solares *et al.* 2002). Region N2 has been mapped with SCUBA to 8 mJy at 850μm (Fox *et al.* 2001, Scott *et al.* 2001). As well as the Chandra observations described here, XMM-Newton observations in regions N2 (150 ksec deep pointing) and N1 (5 × 30 ksec pointings) are awaiting scheduling.

In this chapter I present the analysis of the Chandra X-ray data and the Chandra source catalogue.

5.2 The X-ray data

The ELAIS Deep X-ray Survey (EDXS) is being conducted in the northern ELAIS regions N1 and N2. The Chandra data consists of approximately 75 ks exposures in each field. Region N1 was observed on 3-4 August 2000 (OBS_ID 888) and N2 on 2-3 August 2000 (OBS_ID 887). The nominal aimpoints were N1: 16:10:20.11 +54:33:22.3, and N2: 16:36:46.99 +41:01:33.7. The ACIS-I chips were used with the addition of ACIS-S2 and ACIS-S4.

Analysis was carried out on data reprocessed with version R4CU5UPD14.1 of the pipeline processing software. The data were reduced using the CIAO (cxc.harvard.edu/ciao) software package (version 2.1). Bad pixels and columns were removed and data were filtered to eliminate high background times. The latter was achieved through constructing a lightcurve for background regions and identifying periods of intense background activity due to solar flares. One obvious flaring period was identified over the course of the observations resulting in the removal of 1552 seconds from the data in region N1. More stringent conditions for the removal of high background times were not thought necessary considering the low level of the quiescent background. After filtering, exposures in fields N1 and N2 were 71.5 ks and 73.4 ks respectively.

Exposure maps were constructed to account for variations in effective exposure across an image. This incorporates the positions of bad pixels, dithering, and vignetting. The

effective exposure is significantly affected by the energy of the source counts. To account for this, an assumed source spectrum is convolved with the quantum efficiency of the chip and the effective area of the mirrors. The resulting map provides an estimate of the effective exposure (cm^{-2} s^{-1}) at each point on the image. For our images, I used a standard power-law model spectrum, with photon index $\Gamma = 1.7$.

5.3 Source detection

Sources were detected using a wavelet method, specifically the WAVDETECT program (Freeman *et al.* 2002) included with the CIAO software package. The "Mexican Hat" wavelet function is used, which consists of a positive core similar to a canonical PSF, surrounded by a negative annulus. The overall normalisation is zero. The zero-crossing point is at a radius of $\sqrt{2}$i, and the minimum at 2i, where i refers to the scale size in pixels. The correlation of this wavelet function with an image will reveal sources where correlation values are larger than a pre-defined threshold.

A 2×2 binned image was used, giving a pixel size of $0.984''$. The threshold for source detection was set such that the probability of erroneously identifying a given pixel with a source is 9.5×10^{-7}. This translates to a mean detection of 1.0 false sources over the region of the 4 ACIS-I chips. Wavelet scales were chosen at i = 2, $2\sqrt{2}$, 4, $4\sqrt{2}$, 8, $8\sqrt{2}$, 16, $16\sqrt{2}$, and 32 pixels. The minimum scale was chosen to enclose ~90% encircled energy of an on-axis PSF. Larger scales can then match the increased size of off-axis and resolved sources. The algorithm also uses an exposure map to correct for inconsistencies across the chips.

Sources were detected in 3 bands: 0.5 - 8 keV (full band), 0.5 - 2 keV (soft band), and 2 - 8 keV (hard band). Below 0.5 keV the quantum efficiency (including the optical blocking filters) of the front illuminated chips drops off steeply. A steep rise is also observed in the background rate due to charged particles. Beyond 8 keV the effective area of the mirrors is sharply decreasing whilst the background rate is again beginning to rise.

In order to verify that no sources were missed, I also ran a source detection on the 0.3 - 10 keV band. All sources found were also detected in the 0.5 - 8 keV band, and overall, fewer sources were detected.

5.3.1 Sample reliability and completeness

For the purposes of source detection, counts flagged as cosmic-ray afterglows were removed from the image. This procedure is known to also remove several percent of source photons. Therefore, to obtain reliable measurements of source flux and extent, a second source detection was performed on an image where the flagged counts were reinstated. Only sources obtained in the original source detection were used.

WAVDETECT simulations (Freeman *et al.* 2002) suggest a mean of 1.0 false sources will be detected over the region of the 4 ACIS-I chips. I also impose a cut-off at a S/N of 3.0, principally for the purpose of defining a flux limit. This has the effect of removing a handful of the least significant sources, further improving the reliability of the sample.

The completeness of the WAVDETECT method is yet to be definitively established. Early simulations have been done by V. Kashyap (private communication). These indicate an overall completeness for our sample of 98.5 – 99.5 %.

5.4 The Chandra source catalogue

A total of 233 X-ray sources have been detected in the 2 fields. In N1 there are 127 sources in the full band (0.5 - 8 keV), 101 in the soft band (0.5 - 2 keV) including 2 extra sources not detected in the full band, and 72 sources in the hard band (2 - 8 keV) including 1 extra source not detected in the full band. There are 57 sources detected in both the soft and hard bands. In N2 there are 98 sources in the full band, 81 in the soft band (including 3 extra sources not in the full band), and 52 sources in the hard band (including 2 extra

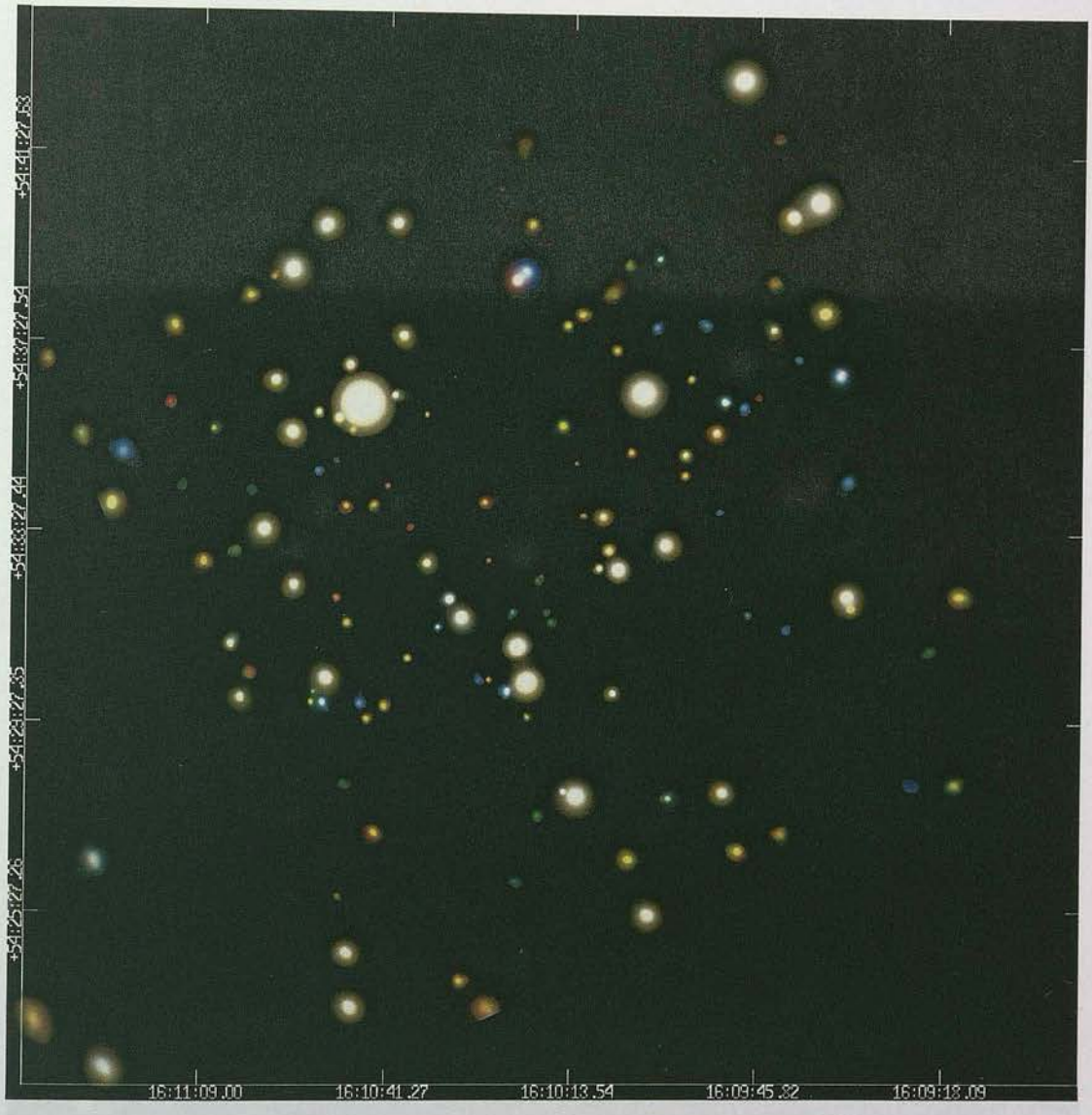

Figure 5.1: 'True-colour' source image of the Chandra field N1. This is a noise-free reconstruction of the raw data using the source properties and correlation images output from the source detection algorithm WAVDETECT. The colours are constructed from the soft-band (red), full-band (green), and hard-band (blue).

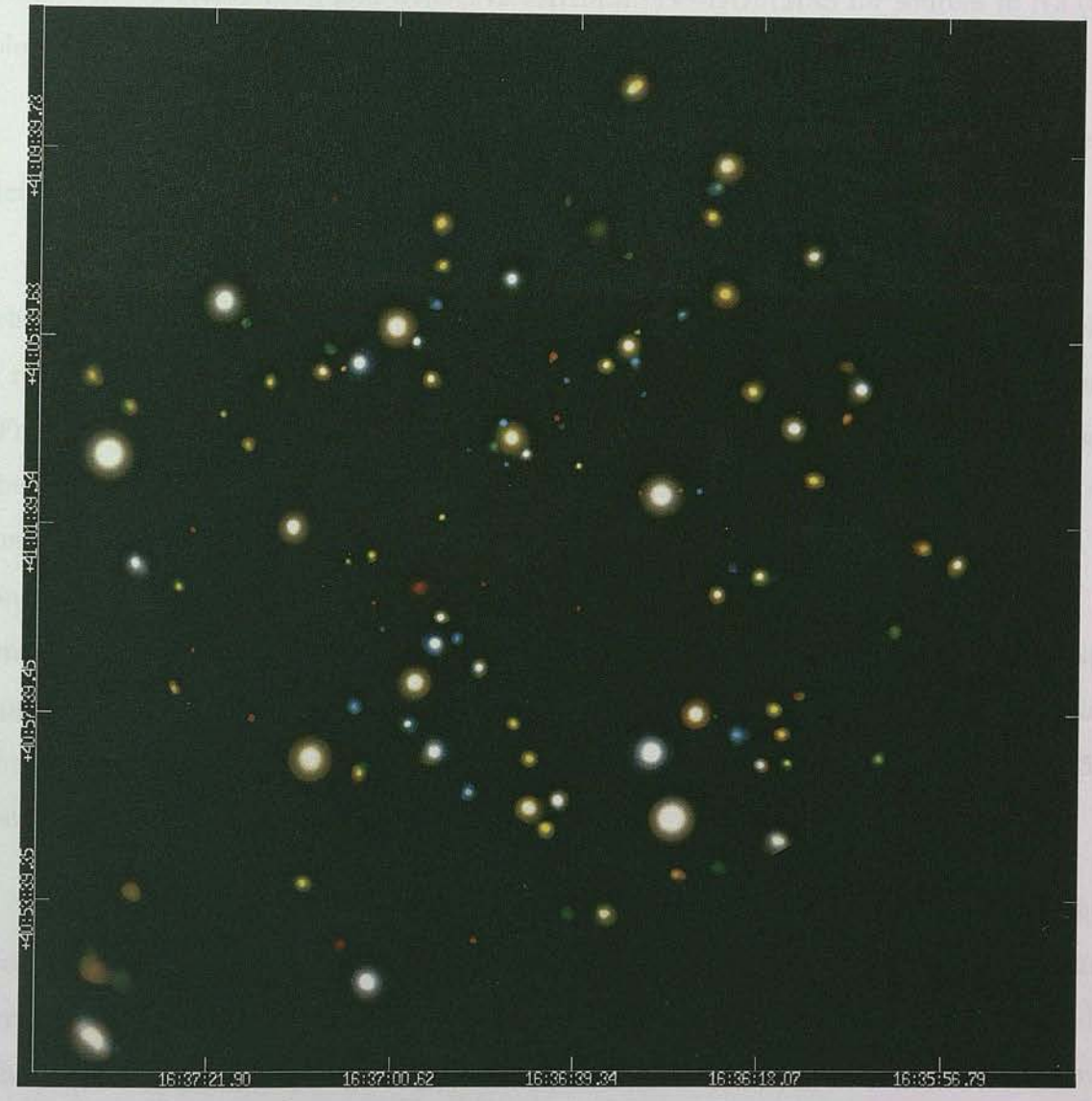

Figure 5.2: 'True-colour' source image of the Chandra field N2, constructed as figure 5.1

sources not in the full band). There are 41 sources detected in both the soft and hard bands.

The IAU name for the catalogued sources is CXOEN1 JHHMMSS.s+DDMMSS, for sources in N1 (table E.1), and CXOEN2 JHHMMSS.s+DDMMSS for sources in N2 (table E.2). Coordinates are truncated to the above accuracy.

Tables E.1 & E.2 display the full catalogue. Sources are detected to a S/N limit of 3, defined as

$$S/N = C/(1 + \sqrt{0.75 + B}) \tag{5.1}$$

where C are the net source counts, and B the background counts within the 'source cell', a region defined by WAVDETECT assumed to contain effectively all of the source counts (Freeman *et al.* 2002). It should be noted that the source cell used here may be larger than regions used for conventional aperture photometry. The values calculated for S/N may therefore be lower than those expected from such methods. The denominator of equation 5.1 is an approximate expression for the error on the background counts (a small number statistic). This comes from Gehrels (1986: equation 7), which gives the upper confidence level equivalent to a 1σ Gaussian error. For sources that do not reach the S/N limit in a certain band, an upper flux limit has been calculated from equation 5.5 (section 5.5.1).

Source coordinates have been astrometrically corrected using calibrated r′ band images (to a depth of r′ ∼26). High S/N Chandra sources were matched with stellar r′ band counterparts. 16 sources were used in N1 and 11 in N2, with a good spread across the fields. The Starlink package ASTROM (star-www.rl.ac.uk/star/docs/sun5.htx/sun5.html) was used to perform a 6-parameter fit (zero points, scales in x and y, orientation and non-perpendicularity). The RMS residuals were all less than 1″, randomly distributed with a mean of ∼0.4″. The positional error quoted in the catalogue is the error on the centroid position from the source detection algorithm, with 0.4″ added in quadrature to represent astrometric error.

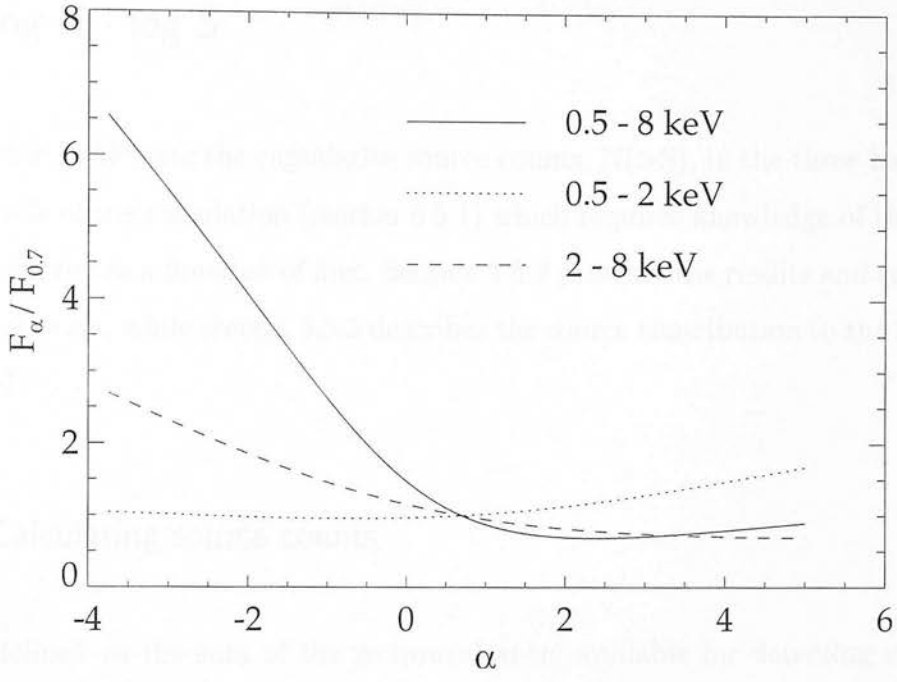

Figure 5.3: Conversion factors to calculate true flux for a source with spectral slope α given the fluxes quoted in the source catalogue (which assumes $\alpha = 0.7$). This figure has been calculated by passing model spectra of slope α through the total response matrix of the detector at a position corresponding to the source N1_23.

Net counts are quoted as the total source counts (background subtracted) in the full energy band (0.5 - 8 keV). Where sources are only detected in the soft or hard bands, the net counts represent counts in this band only.

Flux values are calculated assuming a power-law source spectrum of the form $F = \nu^{-\alpha}$ with $\alpha = 0.7$. The effective area will vary as a function of α depending on the response of the detector. If the slope of the spectrum is known for a given source, figure 5.3 can be used to calculate the true flux from the value given in the catalogue. This figure has been calculated by passing model spectra of slope α through the total response matrix of the detector at a position corresponding to the source N1_23.

5.5 Log N - log S

In this section I calculate the cumulative source counts, N(>S), in the three bands. I first outline details of the calculation (section 5.5.1) which requires knowledge of the available area of the survey as a function of flux. Section 5.5.2 presents the results and comparisons with other surveys, while section 5.5.3 describes the source contribution to the hard X-ray background.

5.5.1 Calculating source counts

N(>S) is defined as the sum of the reciprocal areas available for detecting each source that is brighter than flux S. The sky area over which a source of flux S may be observed depends on the flux limit at each point in the image. This, in turn, depends on the variation in PSF size and effective exposure across the image. The flux limit (S_{lim} in erg cm^{-2} s^{-1}) may be defined by the chosen S/N limit of our sample (from equation 5.1):

$$S/N_{lim} = 3 = C_{lim}/(1 + \sqrt{0.75 + B}) \tag{5.2}$$

where

$$C_{lim} = S_{lim} \times \text{effective exposure} \times K \tag{5.3}$$

K is a constant (conversion factor from ergs to counts), while the effective exposure (in cm^2 s) at each point on the image can be found from the exposure map. The background counts within the source region (B), depend on the size of the PSF:

$$B = B_{avg} \times \text{PSF size} \tag{5.4}$$

B_{avg} is the mean background counts per pixel. This leaves the following expression for the flux limit:

$$S_{lim} = 3 \times \frac{1 + \sqrt{0.75 + (B_{avg} \times \text{PSF size})}}{\text{effective exposure} \times K} \tag{5.5}$$

PSF sizes across the image were taken from the latest PSF library available with the CIAO software distribution. These were used in conjunction with the relevant exposure

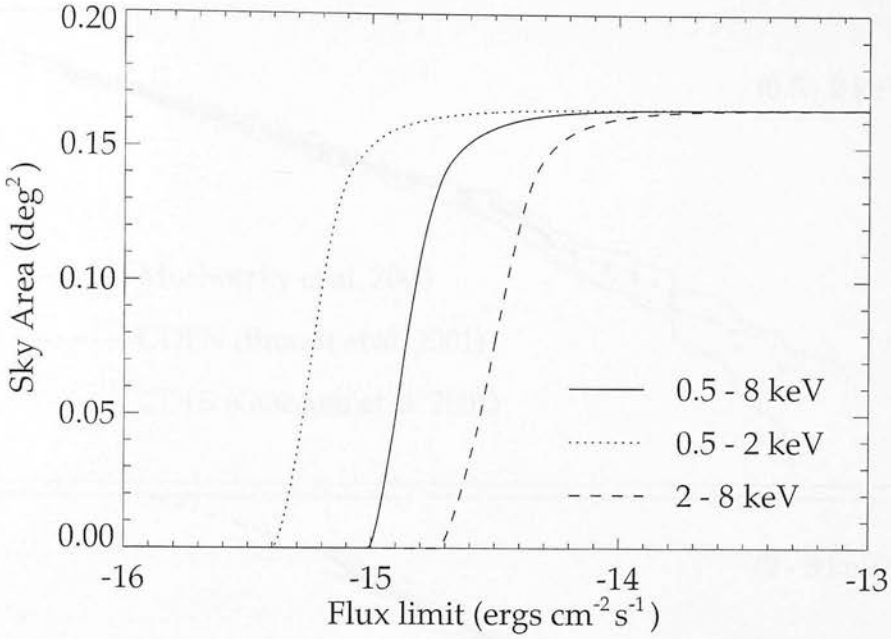

Figure 5.4: Sky area observed at survey flux limit.

maps for each band to calculate a 'flux limit map' of the Chandra image. The sky area available at a given flux limit is found by summing all the pixels with values smaller than this limit. Figure 5.4 displays the sky area available at the flux limit of our survey.

5.5.2 Results

The cumulative number counts per square degree are plotted as filled circles in figure 5.5. 1σ errors are plotted as solid lines. These incorporate Poisson errors on the counts and the error on the available sky area. The limiting flux levels are 1.1×10^{-15} erg cm^{-1} s^{-1} (0.5 - 8 keV), 4.6×10^{-16} erg cm^{-1} s^{-1} (0.5 - 2 keV), and 2.2×10^{-15} erg cm^{-1} s^{-1} (2 - 8 keV). Simulations show completeness to be around 99% (V. Kashyap, private communication), while Eddington bias may result in an over-estimation of the cumulative number counts by approximately 1% (see appendix D for details). These factors work to cancel each other and can safely be neglected.

The slope of the log(N) - log(S) for each band was fitted with a power-law using a

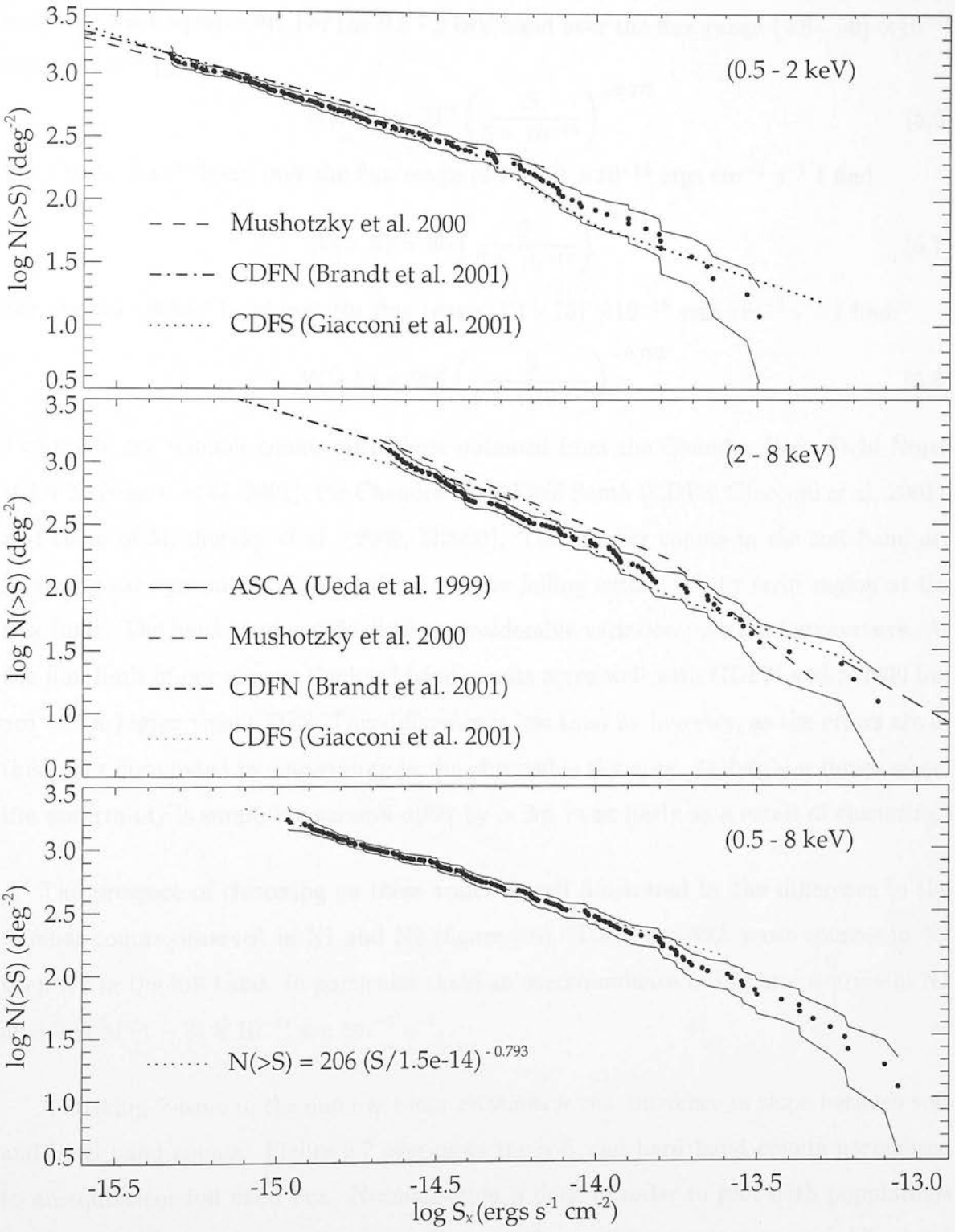

Figure 5.5: Cumulative number counts per square degree for sources detected in the soft (top), hard (middle), and full (bottom) band images. Data are plotted as filled circles with solid lines enclosing 1σ errors. Number counts from other recent surveys are estimated from best-fitting power laws quoted in the above references.

weighted least-squares fit. For the 0.5 - 2 keV band over the flux range (4.6 - 50) $\times 10^{-16}$ erg cm^{-2} s^{-1} I find:

$$N(>S) = 212 \left(\frac{S}{5 \times 10^{-15}} \right)^{-0.773} \tag{5.6}$$

For the 2 - 8 keV band over the flux range (2.2 - 20) $\times 10^{-15}$ ergs cm^{-2} s^{-1} I find:

$$N(>S) = 96 \left(\frac{S}{2 \times 10^{-14}} \right)^{-1.074} \tag{5.7}$$

For the 0.5 - 8 keV band over the flux range (1.1 - 15) $\times 10^{-15}$ ergs cm^{-2} s^{-1} I find:

$$N(>S) = 206 \left(\frac{S}{1.5 \times 10^{-14}} \right)^{-0.793} \tag{5.8}$$

I compare the number counts with those obtained from the Chandra Deep Field North (CDFN, Brandt *et al.* 2001), the Chandra Deep Field South (CDFS, Giacconi *et al.* 2001), and those of Mushotzky *et al.* (2000, M2000). The number counts in the soft band are in very good agreement, with all three surveys falling within the 1σ error region at the flux limit. The hard band counts display considerable variation over the four surveys. At the flux limit of our survey, the hard band counts agree well with CDFN and M2000 but are ~25% higher than CDFS. This difference is less than 2σ however, as the errors are at this point dominated by uncertainty in the observable sky area. At brighter fluxes where the uncertainty is small, the surveys differ by $> 2\sigma$, most likely as a result of clustering.

The presence of clustering on these scales is well illustrated by the difference in the number counts observed in N1 and N2 (figure 5.6). There are 30% more sources in N1 than N2 in the full band. In particular there an overabundance of brighter sources in N1 at a flux of $(1 - 2) \times 10^{-14}$ erg cm^{-2} s^{-1}.

A striking feature of the number count relations is the difference in slope between soft and hard band counts. Figure 5.7 over-plots the soft and hard band counts normalised to an equivalent full band flux. Normalisation is done in order to plot both populations on the same flux scale and does not affect the slope of the number counts. The hard band sources are assumed to have hard spectra and so are normalised using an alpha of 0. The soft band sources are normalised assuming a soft spectrum with an alpha of 1. The ratio of hard sources to soft sources is seen to increase dramatically towards fainter

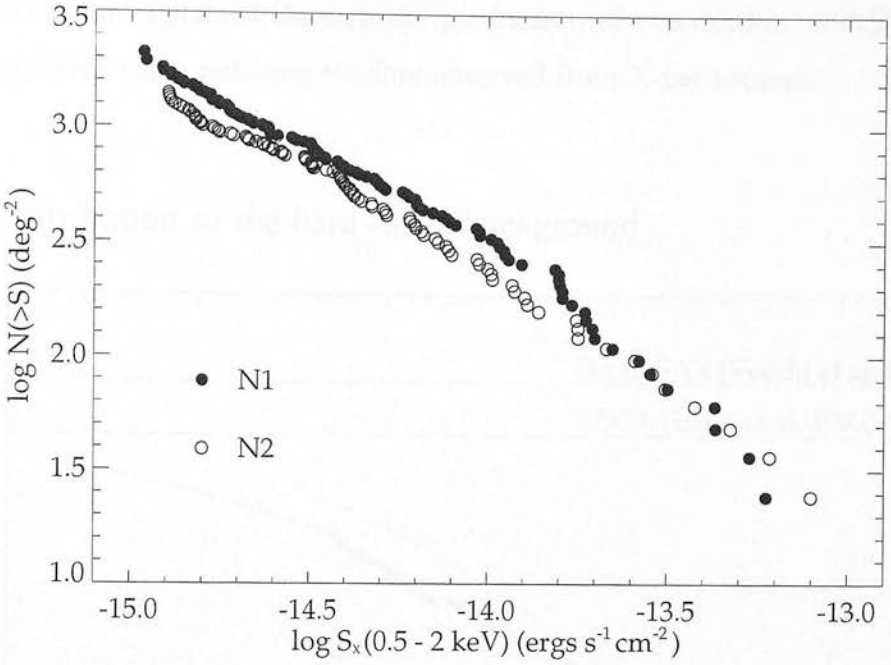

Figure 5.6: Cumulative source counts (0.5 - 8 keV band) for the survey fields N1 & N2 are over-plotted, illustrating the presence of clustering on scales larger than the field size.

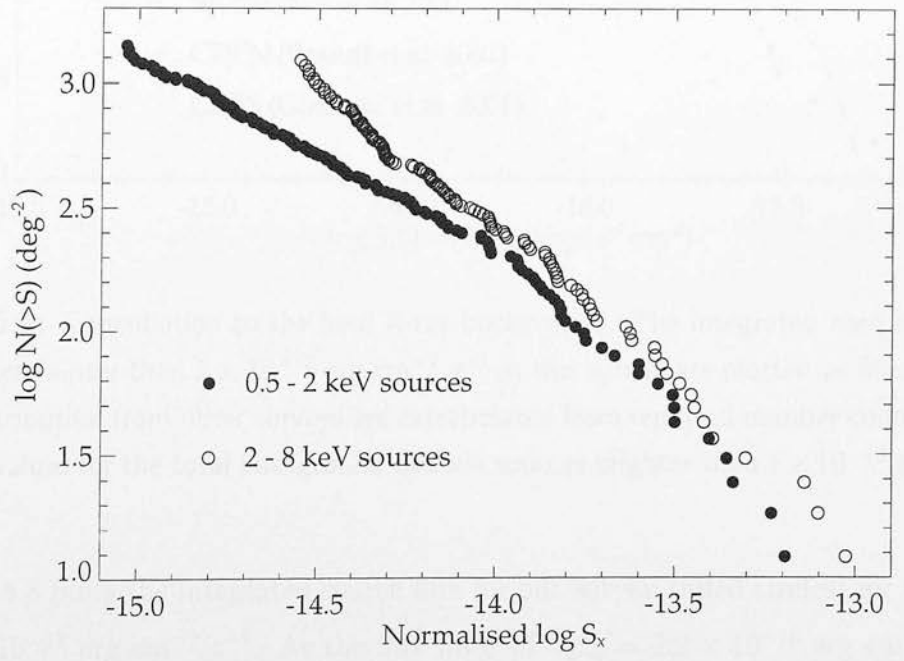

Figure 5.7: Comparison of the cumulative source counts for the combined fields in the soft and hard bands. The counts have been normalised to an equivalent full band flux (see text, section 5.5.2) to better emphasise the difference in slope between these populations.

fluxes. This can be explained through the mechanism of obscuration, which will act to harden the spectra while reducing the flux observed from X-ray sources.

5.5.3 Contribution to the hard X-ray background

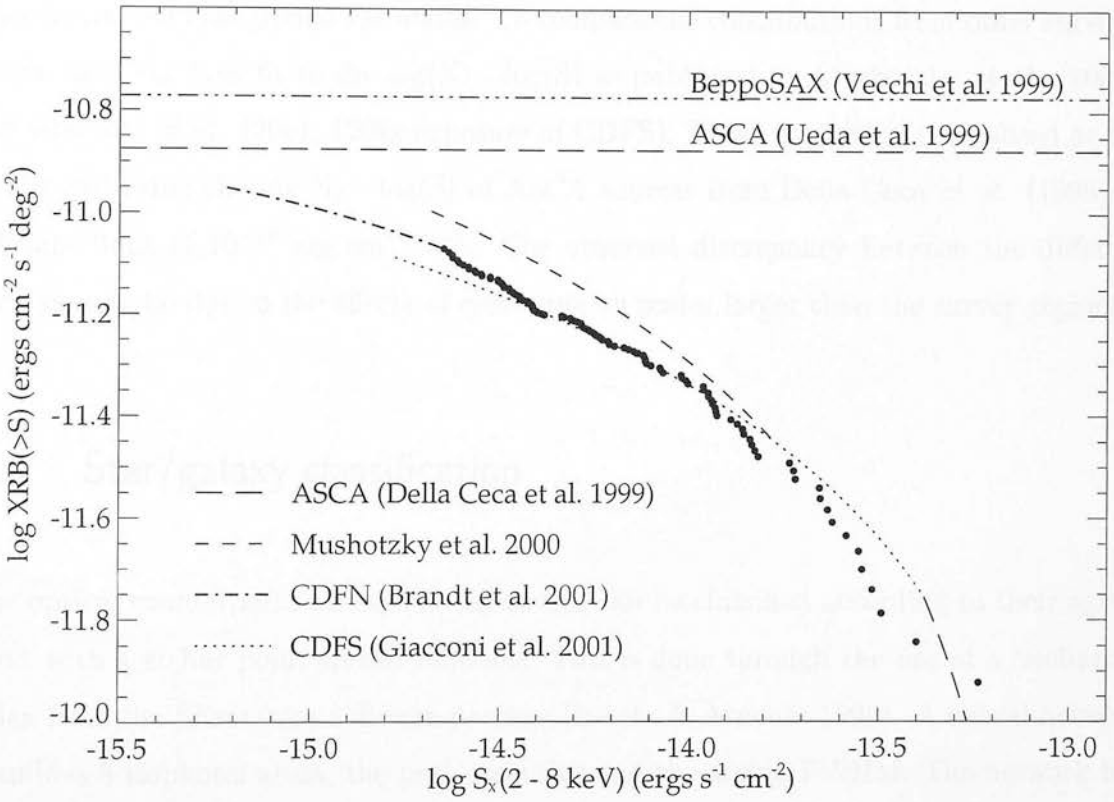

Figure 5.8: Contribution to the hard X-ray background. The integrated hard band flux for sources fainter than 1×10^{-13} erg cm^{-2} s^{-1} in this survey are plotted as filled circles. The contribution from other surveys are extrapolated from reported number count slopes. Plotted values for the total background exclude sources brighter than 1×10^{-13} erg cm^{-2} s^{-1}.

Figure 5.8 plots the integrated source flux for our survey (filled circles) for all sources with $S < 10^{-13}$ erg cm^{-2} s^{-1}. At the flux limit of $S_{2-8} = 2.2 \times 10^{-15}$ erg cm^{-2} s^{-1} the resolved flux amounts to 8.5 $\times 10^{-12}$ erg cm^{-2} s^{-1} deg^{-2}. This is equivalent to between 50 and 64% of the 2 - 8 keV background measured by Vecchi *et al.* (1999, Beppo-Sax) and Ueda *et al.* (1999, ASCA) respectively. To arrive at these values for the total background (as plotted in figure 5.8) the contribution from sources with $S > 10^{-13}$ erg cm^{-2} s^{-1}, as

observed by ASCA (Della Ceca *et al.* 1999), has been subtracted. The contribution to the background at fainter fluxes has been extrapolated from the log(N) - log(S) of the CDFN survey (Brandt *et al.* 2001). By combining the results of our survey with that of CDFN the contribution to the background within the flux range 10^{-13} - 6 $\times 10^{-16}$ erg cm^{-2} s^{-1} becomes 1.12 $\times 10^{-11}$ erg cm^{-2} s^{-1} deg^{-2}, equivalent to 66% and 84% of the aforementioned background estimates. To compare the contributions from other surveys, I have used the best fit to the log(N) - log(S) as published by Mushotzky *et al.* (2000), and Giacconi *et al.* (2001, 120ks exposure of CDFS). These have been normalised at the bright end using the log(N) - log(S) of ASCA sources from Della Ceca *et al.* (1999) to a bright limit of 10^{-13} erg cm^{-2} s^{-1}. The observed discrepancy between the different surveys may be due to the effects of clustering on scales larger than the survey regions.

5.6 Star/galaxy classification

The optical counterparts for each X-ray source can be classified according to their agreement with a stellar point spread function. This is done through the use of a 'stellarity' index from the SExtractor software package (Bertin & Arnouts 1996). A neural network examines 8 isophotal areas, the peak intensity and the seeing FWHM. The network has been trained to distinguish stars and galaxies by studying simulated images. The output parameter depends on the confidence with which the distinction can be made. A perfect PSF would be given a star/galaxy (s/g) classification of 1.0, while a significantly extended source would be given a classification of 0.0.

r′ band images have been obtained for both N1 and N2 to a depth of $\sim$ 26th magnitude. These have been used to classify the Chandra sources into those with galaxy-like and quasar-like optical counterparts (Gonzalez-Solares *et al.* 2002). The cut-off has been chosen at s/g = 0.8. A number of X-ray sources remain unclassified where they are associated with blank fields, gaps in the data, or are near to bright contaminating sources in the optical images. The cumulative soft-band source counts for each group have been

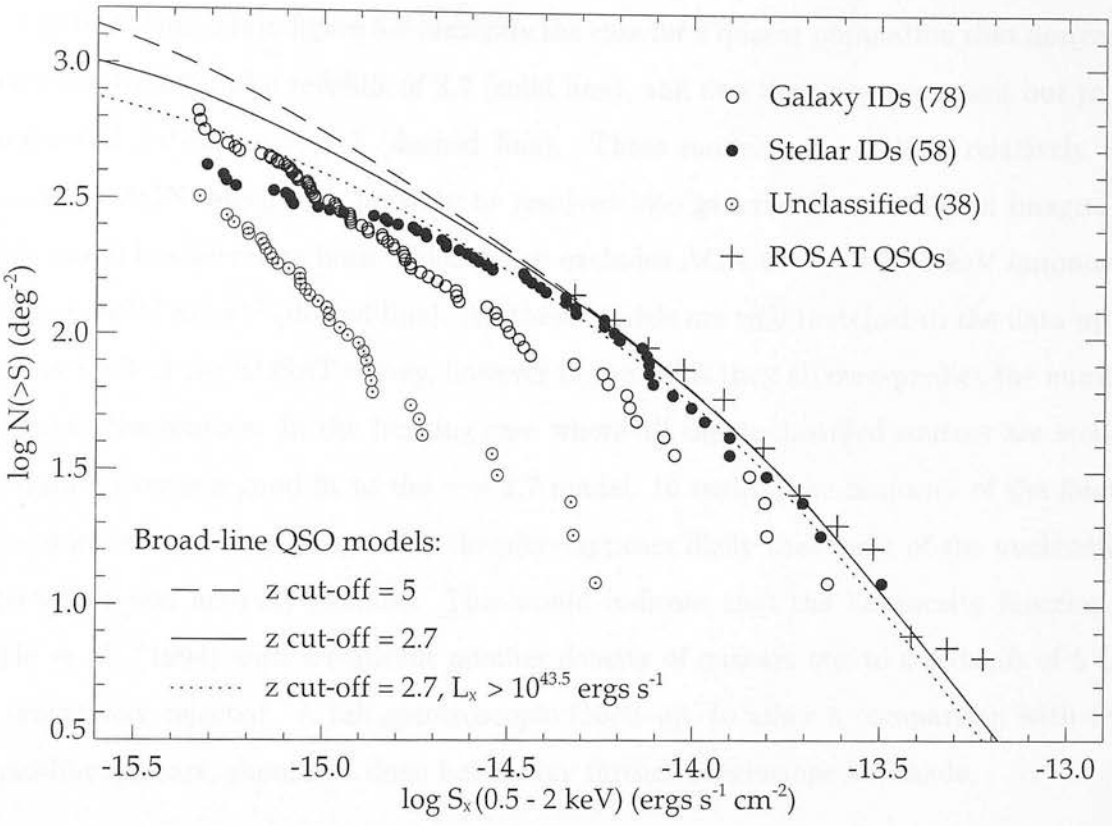

Figure 5.9: Soft band number counts split between quasar-like and galaxy-like optical counterparts. In comparison the QSOs observed with ROSAT (Boyle *et al.* 1994) and associated models for the QSO X-ray luminosity function are over-plotted.

calculated and are plotted in figure 5.9. At bright X-ray fluxes quasar-like sources are the most numerous, however their number counts flatten appreciably below a flux of $\sim 5 \times 10^{-15}$ erg cm^{-2} s^{-1}. At fainter fluxes the fraction of galaxy-like sources dramatically increases. At the flux limit of 4.6×10^{-16} erg cm^{-1} s^{-1} there are 35% more galaxy-like sources than quasar-like sources.

The X-ray luminosity function from Boyle *et al.* (1994), was used to obtain number count predictions for broad-line AGN. This was based on observations of 107 QSOs from a deep ROSAT survey. These QSOs reached a flux limit of $\sim 5 \times 10^{-15}$ erg cm^{-2} s^{-1} in the 0.5 - 2 keV band. I have used their best fitting models to construct predictions for the soft band QSO number counts (see section 3.5). These are over-plotted in figure 5.9 to compare with the cumulative number counts for sources with quasar-like optical IDs.

The first 2 models in figure 5.9 illustrate the case for a quasar population that decreases exponentially beyond a redshift of 2.7 (solid line), and one that stays constant out to an exponential cut-off at $z = 5$ (dashed line). These models also include relatively low luminosity AGN which may possibly be resolved into galaxies in our r′ band images. A third model has therefore been added which excludes AGN with a 0.5 - 2 keV luminosity less than $10^{43.5}$ erg s^{-1} (dotted line). All three models are well matched to the data up to the flux limit of the ROSAT survey, however beyond this they all over-predict the number of quasar-like sources. In the limiting case where all the unclassified sources are stellar, the data becomes a good fit to the $z = 2.7$ model. In reality, the majority of the fainter sources are classified as galaxies. It therefore appears likely that most of the unclassified objects are also actually galaxies. This would indicate that the luminosity function of Boyle *et al.* (1994) with a constant number density of quasars out to a redshift of 5 can be tentatively rejected. A full spectroscopic follow-up, to allow a comparison with true broad-line quasars, should be done before any further conclusions are made.

5.7 Extended sources

To search for X-ray sources on scales much larger than the PSF I have run the source detection algorithm WAVDETECT using wavelet scales of 16, $16\sqrt{2}$, 32, $32\sqrt{2}$, and 64 pixels (see section 5.3). Any sources found in addition to those already detected were checked by inspecting the adaptively smoothed Chandra images (figure 5.10).

No additional sources were detected in N1 and inspection of the smoothed image reveals no hint of large extended sources. In N2 there are 2 significant extended sources. The most significant of these is CXOEN2 J163637.3+410804 displayed in figure 5.11. The X-ray position (centred on the brightest component of the extended source) is at J2000 16:36:37.38 +41:08:04.9. There are 207 net source counts in the 0.5 - 2 keV band in an area corresponding to a factor 17.5 larger than the PSF. This extrapolates to a soft band flux of $1.46 \pm 0.15 \times 10^{-14}$ erg cm^{-2} s^{-1}, although this includes the flux from point source

Figure 5.10: Adaptively smoothed soft band (0.5 - 2 keV) Chandra images of regions N1 (top) & N2 (bottom). Extended sources can be clearly seen in the N2 image at the centre of the I1 chip (top corner), and at the edge of the I3 chip (upper left corner).

Figure 5.11: This 2.5x2.5 arcmin r′-band image displays a cluster of galaxies which coincide with the extended X-ray source CXOEN2 J163637.3+410804. The X-ray contours have been obtained by smoothing the Chandra data with a Gaussian of 10 arcsec. The X-ray position is centred on the brightest component of the extended source. (Figure courtesy of C. Willott.)

N2_101 (CXOEN2 J163633.8+410730) which lies within the extended source region at a distance of 52 arcsec from the core. The r′ band image of this region reveals the presence of a galaxy cluster.

The second extended X-ray source in N2 is also associated with a galaxy cluster. This source (shown in figure 5.12) is at the very edge of the Chandra image. Its position is approximately J2000 16:37:28.5 +41:00:13, although the centroid may in fact lie outside the area of the image. For this reason, the identification and properties of this source will not be reported here.

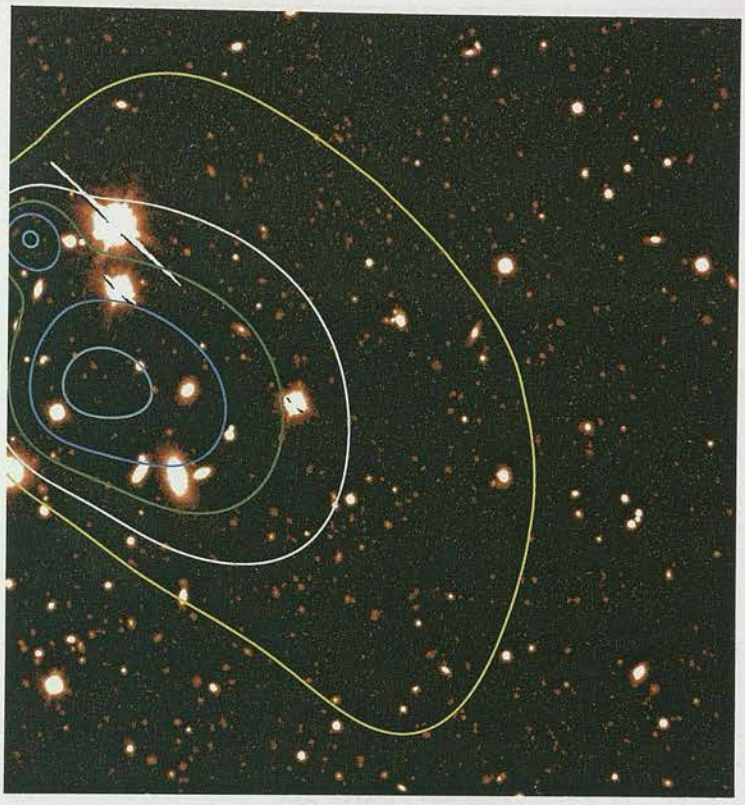

Figure 5.12: This 3x3 arcmin r'-band image displays a cluster of galaxies which coincide with an extended X-ray source very close to the edge of the N2 Chandra image. The X-ray contours have been obtained from an adaptively smoothed Chandra image and can only be used as an illustration due to edge effects. The centroid of the X-ray source is at approximately J2000 16:37:28.5 +41:00:13.

5.8 AGN contribution to 15μm surveys

Bottinelli *et al.* (2002), have cross-correlated the X-ray sources in N1 and N2 with the mid-infrared sources from the ELAIS survey. They find 3 extragalactic sources with 15μm fluxes > 1.5 mJy. Deeper studies of the Lockman Hole and the Hubble Deep Field North (HDFN) have been reported by Fadda *et al.* (2002). 218 square arcminutes in the Lockman region was observed by ISOCAM and XMM-Newton revealing 22 X-ray sources with a 15μm flux > 0.3 mJy. A smaller region in the HDFN (24.3 square arcminutes) was observed with deep Chandra and ISOCAM exposures revealing 20 X-ray sources with a 15μm flux > 0.05 mJy. These number counts have been plotted in figure 5.13 and are

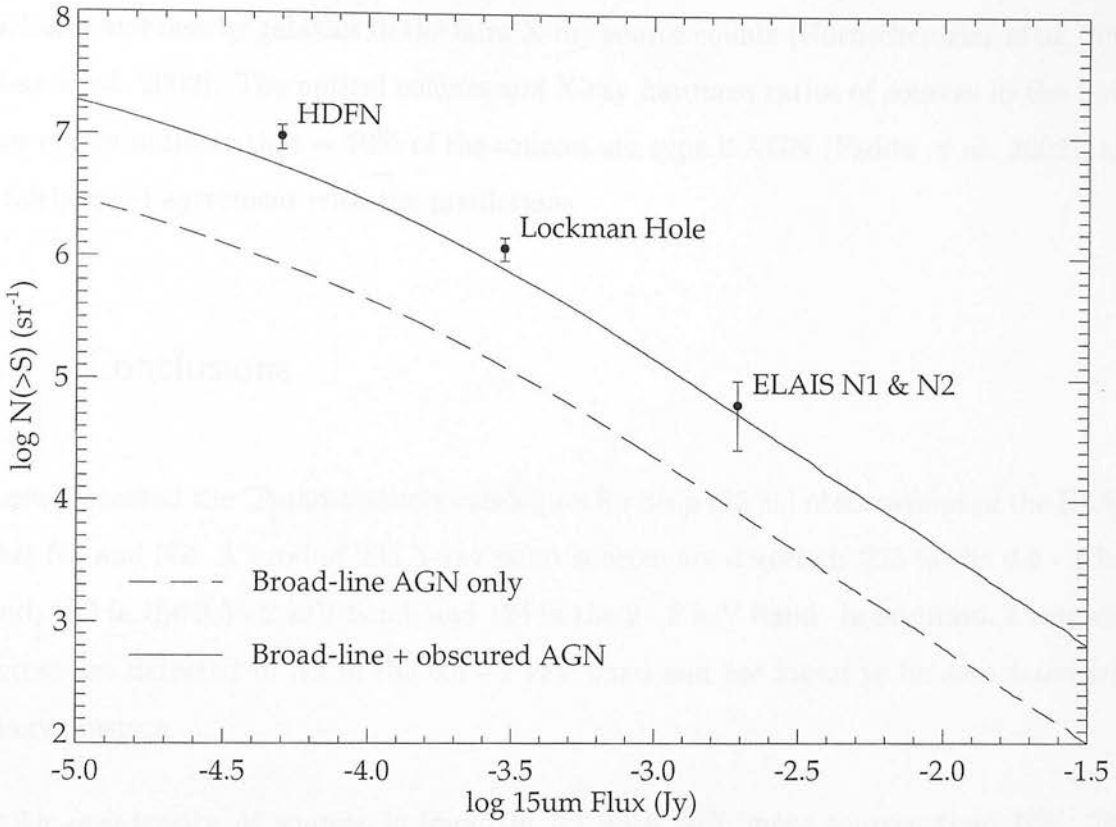

Figure 5.13: Observed number counts of sources displaying both 15μm and X-ray emission (with Poisson errors). These are compared with predictions for the AGN contribution developed in section 3.5. Values for the Lockman Hole and HDFN are taken from Fadda *et al.* (2002). Cross-correlations for the ELAIS regions are from Bottinelli *et al.* (2002).

compared with the predictions made in section 3.5 for the contribution of AGN to mid-infrared surveys. The predicted contribution of obscured AGN is based on the assumption that these sources are responsible for practically the entire hard X-ray background. This assumption has been supported by the the large fraction of the background that has been resolved in recent deep X-ray surveys (see section 5.5.3). The model uses a fit to the X-ray background from Comastri *et al.* (1995). This requires $\sim$ 84% of AGN to have X-ray absorbing columns greater than 10^{21} cm^{-2}.

The total number of predicted sources is well matched to the observed data in figure 5.13. Towards fainter fluxes there is a slight excess in the observed number of sources over the predicted AGN contribution. This may be expected due to the contribution of

starburst and nearby galaxies to the faint X-ray source counts (Hornschemeier *et al.* 2001, Elbaz *et al.* 2002). The optical colours and X-ray hardness ratios of sources in the Lockman region indicate that $\sim$ 70% of the sources are type 2 AGN (Fadda *et al.* 2002), also in fairly good agreement with the predictions.

5.9 Conclusions

I have presented the Chandra source catalogues for deep (75 ks) observations of the ELAIS fields N1 and N2. A total of 233 X-ray point sources are detected: 225 in the 0.5 - 8 keV band, 182 in the 0.5 - 2 keV band, and 124 in the 2 - 8 keV band. In addition, 2 extended sources are detected in N2 in the 0.5 - 2 keV band and are found to be associated with galaxy clusters.

An overdensity of sources is found in N1 with 30% more sources than N2. This difference is present in both the soft and hard band number counts. Log(N) - log(S) relations reveal a greater fraction of hard band over soft band sources as we move towards fainter fluxes. A similar trend is seen with the number of galaxy-like optical counterparts increasing towards fainter fluxes, suggesting the emergence of a population of obscured sources.

Chapter 6

Conclusions

This thesis has been primarily involved with the X-ray properties of AGN, based on the analysis of data from ROSAT and Chandra. In chapter 2, ROSAT data has been used to study the short-timescale X-ray variability properties of high redshift QSOs. In chapter 3, models are developed to determine the emission properties of an obscured population of AGN assumed to be the primary constituent of the hard X-ray background. These models are compared with Chandra observations of sources in the ELAIS deep X-ray survey in chapter 5. These sources are catalogued and an analysis of their statistical properties is also carried out in chapter 5. Here, I will outline the main conclusions that have been determined from this work.

6.1 The X-ray variability of high redshift QSOs

A sample of 156 radio-quiet quasars were taken from the ROSAT PSPC archive covering a redshift range of $0.1 < z < 4.1$. The amplitude of their short timescale X-ray variability (on the order of 1 week) was determined using a maximum likelihood method. Individual QSOs were combined in ensembles in order to identify correlations of variability amplitude with luminosity and redshift. The following results were obtained.

- Radio-quiet quasars over the entire sample display an average variability amplitude of 15% on a timescale of 1 week. This has been determined by measuring the maximum likelihood variability amplitude of an ensemble containing all 156 QSOs. Normalised $\sigma = 0.15 \pm 0.01$.

- For quasars at $z < 2$ there is a clear anti-correlation between quasar luminosity (L_X) and variability amplitude (σ). A power-law fit to the individual quasar variability estimates gives $\sigma \propto L_X^{-\beta}$ with $\beta = 0.27 \pm 0.05$.

- There is tentative evidence for an increase in QSO X-ray variability amplitude towards high redshifts ($z > 2$) in the sense that QSOs of the same X-ray luminosity are more variable at $z > 2$.

Possible explanations for a high-redshift upturn in variability have been discussed. The simplest explanation may be that high-redshift QSOs are accreting at a higher efficiency than local AGN.

6.2 Modelling the characteristics of a population of hidden AGN

Comastri *et al.* (1995) use the QSO X-ray luminosity function of Boyle *et al.* (1994) to determine the properties a population of obscured AGN would require in order to account for the spectral shape of the hard X-ray background. Using the ratios of X-ray absorbing columns given by Comastri *et al.*, and the observed broad band spectral energy distributions of quasars, I have estimated the characteristics of this population from submillimetre to ultraviolet wavelengths. The following results were obtained.

- The broad-band emission expected from a population of obscured AGN necessary to account for the entire hard X-ray background does not exceed the measured cosmic background from submillimetre to UV wavelengths.

- Predictions for the contribution of obscured AGN to mid-infrared surveys are a good fit to the number counts of sources displaying both 15μm and X-ray emission. Identification of a large proportion ($\sim$ 70%) of these sources as type 2 AGN (Fadda *et al.* 2002) also provides good agreement with the model.

These results support the hypothesis that the hard X-ray background is primarily composed of obscured AGN.

The QSO X-ray luminosity function from Boyle *et al.* (1994) used for construction of these models was also compared with the number counts of sources obtained from the ELAIS deep X-ray survey. The luminosity function undergoes pure luminosity evolution out to a redshift of 1.79 (z_{max}). The number density is then assumed to remain constant out to a redshift of 2.7, beyond which there is an exponential decline in the number density of quasars. For comparison, a second model was constructed with a constant number density of quasars out to a redshift of 5 before, again, an exponential decline. These models were compared with the observations.

- The QSO X-ray luminosity function from Boyle *et al.* (1994, model S) over-predicts the number of point-like X-ray sources at faint fluxes, if the number density of quasars is assumed to remain constant out to $z = 5$.
- A model for the luminosity function with an exponential decline in the number density beyond $z = 2.7$ may still be a good fit if point-like X-ray sources are associated with quasars of luminosity L(0.5 - 2 keV) $> 10^{43.5}$ erg s^{-1}.

6.3 Source statistics from the ELAIS deep X-ray survey

I have analysed source properties and statistics in two deep (75 ks) Chandra observations of the ELAIS fields N1 and N2. The catalogue is presented in appendix E. A total of 233 X-ray point sources are detected: 225 in the 0.5 - 8 keV band (S $> 1.1 \times 10^{-15}$ erg cm^{-1}

s^{-1}), 182 in the 0.5 - 2 keV band ($S > 4.6 \times 10^{-16}$ erg cm^{-1} s^{-1}), and 124 in the 2 - 8 keV band ($S > 2.2 \times 10^{-15}$ erg cm^{-1} s^{-1}). In addition, two extended sources are found in the N2 region (0.5 - 2 keV band) coincident with galaxy clusters seen in the optical images. Statistical analysis of source number counts reveals the following properties.

- Clustering of X-ray sources on scales comparable with the field size is evident from the overdensity of sources found in region N1 with 30% more sources than N2.
- The cumulative source counts for the hard X-ray band have a steeper slope than the soft band source counts. This leads to a higher fraction of hard band sources at fainter fluxes. A possible explanation is that obscuration is causing intrinsically bright, softer-spectrum AGN to appear as faint, hard X-ray sources.
- The majority of sources with bright X-ray fluxes have point-like optical counterparts. At fainter X-ray fluxes the fraction of galaxy-like optical counterparts dramatically increases. This may also be explained through the mechanism of obscuration where nuclear emission has been sufficiently obscured for the host galaxy to be resolved.
- Sources detected in the hard X-ray band to a flux limit of 2.2×10^{-15} erg cm^{-2} s^{-1} contribute 50 and 64% of the 2 - 8 keV cosmic background measured by Vecchi *et al.* (1999, Beppo-Sax) and Ueda *et al.* (1999, ASCA) respectively.

This survey has uncovered a population of faint, hard X-ray sources with galaxy-like optical identifications. This may be a population of obscured AGN as hypothesised by Comastri *et al.* (1995) and further modelled in this thesis. Spectroscopic identifications and multi-wavelength analysis will now be necessary to further test this theory.

6.4 Suggested follow-up research

It is now important to conclusively test whether enhanced X-ray variability is evident in the high-redshift quasar population. Data now appearing in the Chandra and XMM-Newton archives would allow a great improvement over the analysis detailed in this thesis. In particular, the Chandra Deep Field - South (Giacconi *et al.* 2001), the Chandra Deep Field - North (Brandt *et al.* 2001), and XMM-Newton observations of the Lockman Hole (Hasinger *et al.* 2001) would provide a large sample for which measurements of variability in individual quasars can be made. The serendipitous Chandra (ChaMP) and XMM-Newton (XMM-SSC) surveys would also be able to provide data for rare, high-redshift quasars. With these data it would be possible to break the degeneracy between luminosity and redshift and accurately determine the correlation between variability amplitude and redshift.

The models for the broad-band emission of an obscured AGN population, presented here, were limited by the accuracy of the assumptions that were made. The relationship between the gas and dust found in AGN is unclear and the absorbing regions may be physically distinct. The gas-to-dust ratio may well depend on luminosity and line of sight. The mean spectral energy distribution (SED) of AGN could also be luminosity dependent, while some features (such as the submillimetre spectrum) are possibly due to contributions from the surrounding galaxy (starburst component). Further work is needed to better define the AGN SED and its behaviour with luminosity and with redshift. It is also important to establish the relationship between X-ray and optical absorption. Chandra and XMM will enable the accurate measurement of N_H columns while spectroscopic follow-up can provide dust columns. Such a survey of gas-to-dust ratios may shed much light on the absorption properties of AGN.

Follow-up work for the ELAIS deep X-ray survey, characterising the multi-wavelength properties of the X-ray sources presented here, is already under way through the ELAIS collaboration. The nature of the sources that have now been found to make up virtually

the entire hard X-ray background, has still to be established. In the longer term it will be important to properly constrain the AGN X-ray luminosity function and its evolution at high redshift. However, this will require the combination of a number of surveys in order to fully sample the luminosity-redshift plane. With the vast amount of high-quality X-ray data now being returned from Chandra and XMM-Newton we will soon know a great deal more about the sources that inhabit the X-ray universe, and perhaps have a host of new questions to answer.

Appendix A

X-ray number count predictions

Equations used to generate the log N - log S relation for quasars in the soft X-ray band.

First I need to calculate the observed flux from an object at redshift z:

$$F_o(\nu_0) = F_e(\nu_1)/(1+z) \tag{A.1}$$

where the subscripts o & e signify the observed and emitted frames respectively. Flux is measured in erg s^{-1} cm^{-2} keV^{-1}.

A K-correction must then be applied to convert from the flux emitted at ν_0 to that emitted at ν_1. Quasar X-ray spectra can be modelled by a power law with $F(\nu) \propto \nu^{-\alpha_X}$. Therefore:

$$F_e(\nu_1) = F_e(\nu_0)/(1+z)^{\alpha_X} \tag{A.2}$$

combined with equation A.1 to give:

$$F_o(\nu_0) = F_e(\nu_0)/(1+z)^{1+\alpha_X} \tag{A.3}$$

$$= \frac{L(\nu_0)}{4\pi D^2 (1+z)^{1+\alpha_X}}$$

$$= \frac{L(\nu_0)(1+z)^{1-\alpha_X}}{4\pi d_L^2} \tag{A.4}$$

For a cosmology with $q_0 = 0$, the luminosity distance $d_L = cz(1 + \frac{z}{2})/H_0$. Therefore:

$$F_o(\nu_0) = \frac{L(\nu_0)H_0^2(1+z)^{1-\alpha_X}}{4\pi c^2 z^2(1+\frac{z}{2})^2} \tag{A.5}$$

I now need to integrate the total number of quasars over all space and a range of luminosities:

$$No. = \int_{L_X(z)_{MIN}}^{L_X(z)_{MAX}} \int_{AllSpace} \Phi_X(L_X, z) dL dV \tag{A.6}$$

where Φ is the luminosity function given in equation 3.1 and the comoving volume element dV is given by:

$$dV(z) = \frac{d_L^2 c dz d\Omega}{H_0(1+z)^3(1+2q_0 z)^{\frac{1}{2}}} \tag{A.7}$$

For $q_0 = 0$ this becomes:

$$dV(z) = \frac{c^3 z^2(1+\frac{z}{2})^2 dz d\Omega}{H_0^3(1+z)^3} \tag{A.8}$$

I can now integrate the total number of quasars as a function of luminosity and redshift:

$$No. = \left(\frac{c}{H_0}\right)^3 \int_{L_X(z)_{MIN}}^{L_X(z)_{MAX}} \int_{z=0}^{z_{MAX}} \frac{\Phi_X(L_X, z) z^2(1+\frac{z}{2})^2}{(1+z)^3} dz dL \int_{sq.deg} d\Omega \tag{A.9}$$

In practice this is done by creating a 2-dimensional array in luminosity and redshift and assigning a number density and observed flux to each element. To create the log N - log S plot, elements are added cumulatively down to a limiting observed flux, S. Note, that for the Boyle luminosity function luminosities are given for the wavelength range 0.3 - 3.5 keV. Therefore the observed fluxes derived from these equations will also be over this band.

Appendix B

15μm number count predictions

From the calculations in the previous section I have quasar number density as a function of redshift and X-ray luminosity, $L(0.3-3.5$ keV). I need to convert $L(0.3-3.5$ keV) to observed IR flux at 15μm. From Green *et al.* (1992), I take the mean X-ray to IR ratio for radio quiet quasars:

$$\log\left(\frac{L_X(0.5-4.5keV)}{L_{60\mu m}}\right) = -0.29 \pm 0.17 \tag{B.1}$$

where

$$L_X(0.5-4.5keV) = \frac{\int_{0.5}^{4.5} \nu^{-\alpha_X} d\nu}{\int_{0.3}^{3.5} \nu^{-\alpha_X} d\nu} L_X(0.3-3.5keV) \tag{B.2}$$

For an α_X of 0.7, this ratio is ~ 1. Therefore:

$$\begin{aligned} L_{60\mu m} &= L_X(0.3-3.5keV)/0.51 \quad \text{erg s}^{-1} \\ &= \frac{L_X(0.3-3.5keV)}{0.51}\frac{\nu_{1keV}}{\nu_{60\mu m}} \quad \text{erg s}^{-1}\ \text{keV}^{-1} \end{aligned} \tag{B.3}$$

Therefore the flux in the emitted frame at 60μm is just:

$$F_e(60\mu m) = \frac{L_{60\mu m}}{4\pi D^2} \quad \text{erg s}^{-1}\ \text{cm}^{-2}\ \text{keV}^{-1} \tag{B.4}$$

Green *et al.* (1992), also give a mean slope for the spectrum of radio quiet quasars in the infrared of $\alpha(12, 60) = 0.8 \pm 0.11$:

$$F_e(15\mu m) = \left(\frac{\nu_{15\mu m}}{\nu_{60\mu m}}\right)^{-0.8} F_e(60\mu m) = 4^{-0.8} F_e(60\mu m) \tag{B.5}$$

The observed flux is then calculated as in equation A.3. The slope appropriate for $\lambda < 15\mu$m is found by inspection of the SED shown in figure 3.1, to be $\alpha \sim 1.0$. Therefore:

$$F_o(15\mu m) = F_e(15\mu m)/(1+z)^2 \tag{B.6}$$

Combining equations B.3 to B.6 gives:

$$F_o(15\mu m) = \frac{L_X(0.3-3.5keV)\ \nu_{1keV}\ 4^{-0.8}}{0.51\ \nu_{60\mu m}\ 4\pi D^2(1+z)^2} \tag{B.7}$$

$$= \frac{L_X(0.3-3.5keV)\ \nu_{1keV}\ 4^{-0.8}}{0.51\ \nu_{60\mu m}\ 4\pi d_L^2}$$

$$= \frac{L_X(0.3-3.5keV)\ \nu_{1keV}\ 4^{-0.8} H_0^2}{0.51\ \nu_{60\mu m}\ 4\pi c^2 z^2 (1+\frac{z}{2})^2} \tag{B.8}$$

This is converted to flux in mJy (1 mJy = 0.242×10^{-8} erg s^{-1} cm^{-2} keV^{-1}). The dispersion in the ratios found by Green *et al.* (1992), are also included in the program by making use of a random number generator. The log N - log S relation is constructed in the same way as for the X-ray number counts.

Appendix C

Background calculation

The background contribution from AGN is calculated in a similar way to the number count estimates. Within the luminosity - redshift array, the number densities are multiplied by the derived flux and integrated over the entire range. The flux at any given wavelength is found as follows:

$$L_X(1keV) = \frac{L_X(0.3-3.5keV)}{\int_{0.3}^{3.5} \nu^{-\alpha_X} d\nu} \quad \text{(C.1)}$$

$$= L_X(0.3-3.5keV)/2.53 \quad \text{for } \alpha_X = 0.7 \quad \text{(C.2)}$$

Therefore:

$$F_e(1keV) = \frac{L_X(0.3-3.5keV)(1+z)^2}{2.53 \times 4\pi d_L^2} \quad \text{(C.3)}$$

$$= \frac{L_X(0.3-3.5keV)H_0^2(1+z)^2}{2.53 \times 4\pi c^2 z^2 (1+\frac{z}{2})^2} \quad \text{for } q_0 = 0 \quad \text{(C.4)}$$

This flux density in the emitted frame is then converted to flux density over the entire wavelength range from submillimetre through to X-ray using flux ratios (R_ν) from the SED of Elvis *et al.* (1994), where $F_e(\nu) = F_e(1keV) \times R_\nu$. This SED is modified when taking into account the contribution from absorbed sources. The k-correction $(1+z)^k$ also uses the whole SED. An additional factor of (1+z) from equation A.1 must be taken

into account to convert to flux in the observed frame, giving:

$$F_o(\nu) = \frac{L_X(0.3-3.5keV)H_0^2(1+z)}{2.53 \times 4\pi c^2 z^2 (1+\frac{z}{2})^2} \times R_\nu (1+z)^k \tag{C.5}$$

This is converted to flux in mJy as before.

Appendix D

Eddington bias calculation

Random errors in flux measurements can systematically alter the source counts measured above a given flux limit. This is known as the 'Eddington bias' (Eddington 1913). If the true differential number counts are increasing towards fainter fluxes, the measured number counts will be artificially increased. The two factors affecting the bias are the slope of the number counts, and the measurement error on the flux.

Peterson (1997, p162) derive the Eddington bias based on measurements of magnitude (m). They assume measurement errors are Gaussian distributed with width σ in magnitudes. They also assume the cumulative number counts can be described by the following equation:

$$N(< m) \propto 10^{km} \tag{D.1}$$

where k is a constant.

It is then possible to calculate the ratio of the true differential number counts, A(m), to the observed differential number counts A_{obs}(m), as follows:

$$\frac{A(m)}{A_{obs}(m)} \approx 1 - \frac{1}{2}\left(\frac{\sigma k}{\log e}\right)^2 \tag{D.2}$$

For sources in the ELAIS deep X-ray survey, measurements are in units of erg cm^{-2} s^{-1}. Equation D.1 can be rewritten:

$$\log N(>S) \propto C - 2.5k \log S \tag{D.3}$$

k can then be simply derived from the slope of the log(N) - log(S). For the full-band sources (equation 5.8), $k = 0.32$.

To calculate σ, the mean measurement error at the flux limit needs to be converted to an error in magnitudes:

$$\sigma = \Delta m = -2.5 \log \frac{S_{lim}}{S_{lim} + \Delta S} \tag{D.4}$$

Assuming a 40% error on measurements at the flux limit gives $\sigma = 0.37$ mag. Putting these values into equation D.2 gives:

$$\frac{A(m)}{A_{obs}(m)} = 0.96 \tag{D.5}$$

The measured differential counts are $\sim$ 4% higher than the true differential counts at the flux limit. However, this will only affect the counts within ΔS of the flux limit. Equation 5.8 can be used to estimate the number of affected sources. This gives $\sim$400 sources within ΔS of the full band flux limit, out of a total of $\sim$1600 per square degree. Therefore the number counts have been overestimated by 16 (4% of 400) counts out of a total of 1600, or 1% of the cumulative number count total.

Appendix E

The Chandra source catalogue

Here the full catalogue of Chandra sources detected in the ELAIS fields N1 and N2 is presented. The details of source detection and methods used in construction of the catalogue are given in chapter 5. Table E.1 lists the 130 sources detected in the ELAIS N1 field, and table E.2, the 103 sources detected in the ELAIS N2 field. Columns provide the following information: i) ID number; ii) official IAU source name (coordinates are truncated to the required accuracy); iii-iv) astrometrically corrected source coordinates (J2000 Equinox); v) positional error in arcseconds including contributions from centroid uncertainty and astrometric error; vi) net source counts in the 0.5 - 8 keV band (Note: where sources are only detected in the soft or hard bands, net counts are for that band only); vii) Signal-to-noise as defined in section 5.4, calculated in the same band as the net counts; viii-x) source flux in each band assuming a photon index of $\Gamma = 1.7$; xi) hardness ratio defined as (H-S)/(H+S), where H & S are net counts in the hard and soft bands respectively; xii) Vega r′ magnitude for the most likely optical counterpart (courtesy of E. Gonzalez-Solares); xiii) SExtractor 'stellarity' parameter as defined in section 5.6 (courtesy of E. Gonzalez-Solares).

Table E.1: Chandra sources in the ELAIS N1 field.

ID	CXOEN1	RA (J2000)	Dec (J2000)	Err (arcsec)	Net Cts	S/N	Flux ($\times 10^{-14}$ erg cm^{-2} s^{-1}) (0.5–8keV)	(0.5–2keV)	(2–8keV)	HR	r′	s/g
N1_1	J161121.8+543402	16:11:21.88	+54:34:02.7	0.65	76.3	17.4	1.24 ± 0.15	0.48 ± 0.07	< 0.41	-1.00 ± 0.00	> 25.20	—
N1_2	J161113.1+543748	16:11:13.10	+54:37:48.7	0.84	30.5	7.2	0.42 ± 0.09	0.12 ± 0.03	< 0.40	-1.00 ± 0.00	> 25.20	—
N1_3	J161104.3+543107	16:11:04.33	+54:31:07.2	0.63	31.9	8.8	0.43 ± 0.08	0.12 ± 0.03	0.32 ± 0.12	-0.19 ± 0.22	25.32	0.548
N1_4	J161059.5+543332	16:10:59.53	+54:33:32.4	0.45	122.5	31.6	1.62 ± 0.15	0.59 ± 0.06	1.13 ± 0.20	-0.35 ± 0.10	21.55	0.032
N1_5	J161058.1+543640	16:10:58.16	+54:36:40.7	0.47	60.6	18.5	0.81 ± 0.11	0.31 ± 0.05	0.58 ± 0.14	-0.37 ± 0.14	> 25.20	—
N1_6	J161055.7+543901	16:10:55.74	+54:39:01.0	0.47	195.6	43.7	2.64 ± 0.19	0.89 ± 0.08	2.23 ± 0.29	-0.23 ± 0.08	22.09	0.094
N1_8	J161055.5+543535	16:10:55.50	+54:35:35.6	0.44	125.9	34.8	1.72 ± 0.16	0.70 ± 0.07	0.96 ± 0.19	-0.49 ± 0.10	22.56	0.762
N1_9	J161055.0+543222	16:10:55.09	+54:32:22.3	0.50	56.6	16.2	0.74 ± 0.10	0.28 ± 0.04	0.52 ± 0.14	-0.36 ± 0.15	24.65	0.649
N1_10	J161052.3+542953	16:10:52.37	+54:29:53.8	0.63	12.6	4.1	0.17 ± 0.05	0.05 ± 0.02	< 0.28	-1.00 ± 0.00	22.45	0.909
N1_11	J161051.6+543600	16:10:51.68	+54:36:00.9	0.57	27.0	7.9	0.35 ± 0.07	0.11 ± 0.03	0.36 ± 0.12	-0.11 ± 0.21	> 25.20	—
N1_12	J161050.7+542953	16:10:50.73	+54:29:53.9	0.61	30.8	8.5	0.41 ± 0.08	0.07 ± 0.02	0.61 ± 0.15	0.35 ± 0.21	> 25.20	—
N1_13	J161050.8+543956	16:10:50.85	+54:39:56.6	0.54	113.8	27.3	1.54 ± 0.15	0.58 ± 0.07	1.30 ± 0.22	-0.28 ± 0.10	22.06	0.967
N1_14	J161050.2+543024	16:10:50.21	+54:30:24.1	0.44	119.6	34.4	1.96 ± 0.18	0.73 ± 0.08	1.40 ± 0.25	-0.35 ± 0.10	22.64	0.977
N1_15	J161048.6+543553	16:10:48.64	+54:35:53.2	0.46	83.0	23.0	1.06 ± 0.12	0.45 ± 0.06	0.50 ± 0.14	-0.57 ± 0.13	21.87	0.980
N1_16	J161047.6+542813	16:10:47.68	+54:28:13.0	0.66	10.4	3.7	0.15 ± 0.05	< 0.06	< 0.32	—	24.54	0.298
N1_17	J161047.5+543401	16:10:47.50	+54:34:01.9	0.66	12.4	4.0	0.16 ± 0.05	0.08 ± 0.02	< 0.24	-1.00 ± 0.00	13.10	0.710
N1_18	J161047.2+543134	16:10:47.25	+54:31:34.7	0.63	18.7	5.8	0.24 ± 0.06	0.07 ± 0.02	< 0.25	-1.00 ± 0.00	23.65	0.186
N1_19	J161047.0+543700	16:10:47.08	+54:37:00.8	0.52	50.9	14.1	0.66 ± 0.10	0.25 ± 0.04	0.40 ± 0.12	-0.44 ± 0.16	21.47	0.977
N1_20	J161046.5+543538	16:10:46.57	+54:35:38.8	0.69	18.2	5.4	0.23 ± 0.06	0.08 ± 0.03	< 0.24	-1.00 ± 0.00	19.81	1.000
N1_21	J161046.0+542328	16:10:46.03	+54:23:28.5	0.73	126.9	18.9	1.87 ± 0.19	0.66 ± 0.08	1.10 ± 0.25	-0.41 ± 0.11	23.31	0.203
N1_22	J161045.1+542952	16:10:45.18	+54:29:52.6	0.61	18.6	5.7	0.24 ± 0.06	< 0.05	0.54 ± 0.14	1.00 ± 0.00	> 25.20	—
N1_23	J161045.1+543612	16:10:45.15	+54:36:12.9	0.40	2826.1	569.9	36.00 ± 0.68	14.10 ± 0.31	22.46 ± 0.83	-0.43 ± 0.02	19.01	0.986
N1_24	J161044.1+542934	16:10:44.18	+54:29:34.1	0.70	18.9	5.5	0.24 ± 0.06	0.07 ± 0.02	< 0.26	-1.00 ± 0.00	> 25.20	—
N1_25	J161044.1+543601	16:10:44.14	+54:36:01.9	0.42	148.2	41.5	1.88 ± 0.16	0.68 ± 0.07	1.45 ± 0.22	-0.30 ± 0.09	25.36	0.650
N1_26	J161042.8+542710	16:10:42.87	+54:27:10.2	0.68	24.6	7.1	0.33 ± 0.07	0.13 ± 0.03	< 0.32	-1.00 ± 0.00	21.81	0.068
N1_27	J161041.6+542950	16:10:41.62	+54:29:50.1	0.69	19.9	6.2	0.30 ± 0.07	0.09 ± 0.03	< 0.30	-1.00 ± 0.00	24.24	0.289

ID	CXOEN1	RA (J2000)	Dec (J2000)	Err (arcsec)	Net Cts	S/N	Flux ($\times 10^{-14}$ erg cm^{-2} s^{-1}) (0.5–8keV)	(0.5–2keV)	(2–8keV)	HR	r′	s/g
N1_28	J161041.3+543428	16:10:41.33	+54:34:28.4	0.55	8.8	3.2	0.11 ± 0.04	0.05 ± 0.02	< 0.22	-1.00 ± 0.00	23.50	0.651
N1_29	J161040.2+543623	16:10:40.29	+54:36:23.3	0.48	25.9	8.7	0.33 ± 0.07	0.10 ± 0.03	0.36 ± 0.11	-0.04 ± 0.21	—	—
N1_30	J161040.1+544000	16:10:40.14	+54:40:00.9	0.54	70.9	18.7	0.95 ± 0.12	0.35 ± 0.05	0.77 ± 0.17	-0.29 ± 0.13	22.17	0.201
N1_31	J161039.1+543738	16:10:39.13	+54:37:38.5	0.48	61.2	17.1	0.78 ± 0.10	0.29 ± 0.05	0.49 ± 0.13	-0.41 ± 0.15	24.36	0.127
N1_32	J161038.1+543050	16:10:38.14	+54:30:50.3	0.49	15.5	5.5	0.19 ± 0.05	0.08 ± 0.02	< 0.23	-1.00 ± 0.00	> 25.20	—
N1_34	J161035.4+543250	16:10:35.40	+54:32:50.7	0.46	39.8	13.3	0.50 ± 0.08	0.19 ± 0.04	0.32 ± 0.10	-0.41 ± 0.18	23.71	0.977
N1_38	J161033.6+543129	16:10:33.67	+54:31:29.9	0.44	15.2	5.8	0.19 ± 0.05	< 0.04	0.32 ± 0.10	1.00 ± 0.00	22.76	0.032
N1_39	J161031.9+543204	16:10:31.97	+54:32:04.7	0.45	48.7	16.1	0.77 ± 0.11	0.23 ± 0.05	0.80 ± 0.18	-0.08 ± 0.15	24.09	0.954
N1_40	J161030.1+543142	16:10:30.12	+54:31:42.0	0.42	129.0	38.0	1.58 ± 0.14	0.57 ± 0.06	1.19 ± 0.19	-0.32 ± 0.09	23.37	0.137
N1_41	J161027.5+543022	16:10:27.59	+54:30:22.4	0.67	9.8	3.3	0.12 ± 0.04	< 0.04	0.25 ± 0.09	1.00 ± 0.00	—	—
N1_43	J161026.7+543408	16:10:26.78	+54:34:08.1	0.50	13.7	5.0	0.17 ± 0.05	0.08 ± 0.02	< 0.20	-1.00 ± 0.00	24.95	0.638
N1_45	J161023.2+543008	16:10:23.26	+54:30:08.7	0.50	45.3	13.6	0.59 ± 0.09	0.08 ± 0.02	1.00 ± 0.18	0.51 ± 0.18	> 25.20	—
N1_46	J161022.4+543149	16:10:22.45	+54:31:49.2	0.52	11.6	4.2	0.15 ± 0.05	< 0.04	0.24 ± 0.09	1.00 ± 0.00	24.55	0.592
N1_47	J161022.1+543850	16:10:22.13	+54:38:50.8	0.46	80.3	22.7	1.02 ± 0.12	0.36 ± 0.05	0.77 ± 0.16	-0.31 ± 0.12	20.15	0.058
N1_48	J161021.7+543104	16:10:21.76	+54:31:04.7	0.41	260.8	71.9	3.17 ± 0.20	1.25 ± 0.09	1.89 ± 0.24	-0.45 ± 0.07	19.92	0.988
N1_49	J161020.8+543900	16:10:20.88	+54:39:00.9	0.46	87.0	25.6	1.11 ± 0.12	0.10 ± 0.03	2.21 ± 0.27	0.68 ± 0.13	—	—
N1_50	J161020.3+543020	16:10:20.34	+54:30:20.0	0.41	434.6	112.8	5.36 ± 0.26	2.20 ± 0.12	2.81 ± 0.29	-0.52 ± 0.05	20.16	0.984
N1_51	J161020.2+542937	16:10:20.25	+54:29:37.2	0.64	13.9	4.7	0.19 ± 0.06	< 0.05	< 0.24	—	> 25.20	—
N1_52	J161019.9+544001	16:10:19.96	+54:40:01.8	0.68	23.1	6.8	0.32 ± 0.07	0.13 ± 0.03	< 0.31	-1.00 ± 0.00	—	—
N1_53	J161018.8+543229	16:10:18.81	+54:32:29.5	0.61	10.7	3.6	0.13 ± 0.04	< 0.04	< 0.19	—	> 25.20	—
N1_54	J161016.7+543136	16:10:16.78	+54:31:36.9	0.58	11.0	3.8	0.13 ± 0.05	< 0.04	< 0.20	—	> 25.20	—
N1_55	J161015.1+543546	16:10:15.12	+54:35:46.4	0.51	27.6	9.1	0.33 ± 0.07	0.13 ± 0.03	< 0.20	-1.00 ± 0.00	22.79	0.032
N1_56	J161014.6+542802	16:10:14.64	+54:28:02.2	0.63	25.0	7.4	0.32 ± 0.07	0.09 ± 0.03	0.37 ± 0.12	0.04 ± 0.22	> 25.20	—
N1_57	J161014.5+543754	16:10:14.57	+54:37:54.0	0.60	21.4	6.5	0.28 ± 0.07	0.09 ± 0.03	< 0.25	-1.00 ± 0.00	> 25.20	—
N1_58	J161013.0+543459	16:10:13.07	+54:34:59.6	0.72	9.0	3.1	0.11 ± 0.04	< 0.04	< 0.20	—	> 25.20	—
N1_59	J161012.8+542756	16:10:12.80	+54:27:56.5	0.43	219.2	53.6	2.84 ± 0.20	1.07 ± 0.09	1.91 ± 0.25	-0.38 ± 0.07	23.36	0.934

ID	CXOEN1	RA (J2000)	Dec (J2000)	Err (arcsec)	Net Cts	S/N	Flux ($\times 10^{-14}$ erg cm^{-2} s^{-1}) (0.5–8keV)	(0.5–2keV)	(2–8keV)	HR	r′	s/g
N1_60	J161012.3+543807	16:10:12.33	+54:38:07.9	0.60	21.0	6.6	0.28 ± 0.07	0.14 ± 0.03	< 0.26	-1.00 ± 0.00	—	—
N1_61	J161009.5+543245	16:10:09.59	+54:32:45.6	0.58	26.3	7.9	0.32 ± 0.07	0.12 ± 0.03	0.23 ± 0.09	-0.34 ± 0.22	23.64	0.363
N1_62	J161009.0+543350	16:10:09.05	+54:33:50.9	0.42	39.8	16.6	1.12 ± 0.18	0.48 ± 0.08	0.51 ± 0.20	-0.58 ± 0.19	22.49	0.982
N1_64	J161008.1+543307	16:10:08.12	+54:33:07.7	0.44	51.7	17.2	0.63 ± 0.09	0.29 ± 0.04	0.22 ± 0.09	-0.67 ± 0.17	22.74	0.946
N1_65	J161007.4+543006	16:10:07.45	+54:30:06.8	0.54	25.2	8.7	0.48 ± 0.10	0.12 ± 0.03	0.59 ± 0.18	0.12 ± 0.21	> 25.20	—
N1_66	J161007.1+543722	16:10:07.16	+54:37:22.8	0.65	15.2	4.8	0.19 ± 0.05	0.09 ± 0.02	< 0.24	-1.00 ± 0.00	> 25.20	—
N1_67	J161006.7+543243	16:10:06.77	+54:32:43.3	0.41	182.5	55.5	2.23 ± 0.17	0.88 ± 0.08	1.35 ± 0.20	-0.45 ± 0.08	21.98	0.975
N1_68	J161004.8+543513	16:10:04.88	+54:35:13.3	0.61	15.6	5.1	0.20 ± 0.06	0.08 ± 0.02	< 0.22	-1.00 ± 0.00	> 25.20	—
N1_69	J161003.1+543628	16:10:03.18	+54:36:28.4	0.41	481.9	116.3	5.95 ± 0.27	2.30 ± 0.12	3.98 ± 0.35	-0.40 ± 0.05	18.66	0.017
N1_71	J161002.0+542525	16:10:02.03	+54:25:25.5	0.61	107.2	21.2	1.59 ± 0.16	0.61 ± 0.07	0.84 ± 0.19	-0.49 ± 0.12	21.64	0.982
N1_72	J161001.2+543752	16:10:01.26	+54:37:52.4	0.66	16.2	5.2	0.20 ± 0.06	< 0.05	0.38 ± 0.12	1.00 ± 0.00	24.90	0.770
N1_73	J161000.8+543918	16:10:00.86	+54:39:18.9	0.70	22.3	6.7	0.32 ± 0.07	0.06 ± 0.02	0.36 ± 0.12	0.22 ± 0.26	23.59	0.027
N1_75	J160959.6+543315	16:09:59.65	+54:33:15.2	0.43	125.4	35.7	1.62 ± 0.15	0.63 ± 0.07	0.96 ± 0.18	-0.45 ± 0.10	20.75	0.983
N1_76	J160959.0+542754	16:09:59.08	+54:27:54.1	0.63	15.5	6.2	0.49 ± 0.13	0.14 ± 0.05	0.56 ± 0.22	-0.02 ± 0.26	24.54	0.458
N1_77	J160956.9+543444	16:09:56.92	+54:34:44.5	0.62	14.3	5.6	0.34 ± 0.09	0.13 ± 0.04	< 0.37	-1.00 ± 0.00	24.82	0.752
N1_78	J160956.7+543510	16:09:56.79	+54:35:10.3	0.47	26.6	8.8	0.38 ± 0.08	0.15 ± 0.03	0.26 ± 0.10	-0.39 ± 0.22	24.82	0.813
N1_79	J160956.0+543647	16:09:56.09	+54:36:47.4	0.55	14.0	4.8	0.18 ± 0.05	0.07 ± 0.02	< 0.25	-1.00 ± 0.00	19.70	0.985
N1_81	J160952.2+543538	16:09:52.23	+54:35:38.6	0.47	45.0	14.2	0.58 ± 0.09	0.24 ± 0.04	0.28 ± 0.10	-0.55 ± 0.18	22.15	0.983
N1_82	J160951.0+542801	16:09:51.05	+54:28:01.9	0.55	70.4	18.1	0.95 ± 0.12	0.35 ± 0.05	0.59 ± 0.15	-0.41 ± 0.14	22.83	0.942
N1_83	J160951.0+543618	16:09:51.02	+54:36:18.8	0.62	34.7	9.5	0.48 ± 0.09	0.10 ± 0.03	0.62 ± 0.15	0.20 ± 0.19	24.52	0.885
N1_84	J160948.6+544307	16:09:48.68	+54:43:07.3	0.59	304.1	39.6	4.29 ± 0.26	1.57 ± 0.11	2.86 ± 0.36	-0.37 ± 0.07	21.23	0.985
N1_85	J160947.4+543147	16:09:47.46	+54:31:47.0	0.61	13.0	4.4	0.17 ± 0.05	< 0.05	< 0.25	—	> 25.20	—
N1_86	J160943.8+543749	16:09:43.88	+54:37:49.3	0.71	28.8	7.6	0.38 ± 0.08	0.11 ± 0.03	0.39 ± 0.12	-0.06 ± 0.21	22.27	0.058
N1_87	J160941.0+544013	16:09:41.08	+54:40:13.1	0.58	147.1	26.0	1.99 ± 0.18	0.78 ± 0.08	1.18 ± 0.22	-0.45 ± 0.10	22.03	0.906
N1_89	J160937.2+544032	16:09:37.20	+54:40:32.6	0.51	307.8	47.6	4.31 ± 0.26	1.56 ± 0.11	3.22 ± 0.37	-0.32 ± 0.06	22.42	0.206
N1_90	J160936.2+543812	16:09:36.24	+54:38:12.5	0.58	80.9	18.2	1.08 ± 0.13	0.45 ± 0.06	0.49 ± 0.15	-0.58 ± 0.14	22.51	0.982

ID	CXOEN1	RA (J2000)	Dec (J2000)	Err (arcsec)	Net Cts	S/N	Flux ($\times 10^{-14}$ erg cm^{-2} s^{-1}) (0.5–8keV)	(0.5–2keV)	(2–8keV)	HR	r′	s/g
N1_92	J160933.9+543652	16:09:33.97	+54:36:52.3	0.58	47.1	12.5	0.62 ± 0.10	0.09 ± 0.03	1.13 ± 0.21	0.50 ± 0.18	22.03	0.027
N1_93	J160932.8+543210	16:09:32.83	+54:32:10.4	0.49	118.5	28.1	1.58 ± 0.15	0.58 ± 0.06	1.18 ± 0.21	-0.32 ± 0.10	22.88	0.982
N1_94	J160932.3+543155	16:09:32.31	+54:31:55.5	0.66	44.9	10.9	0.60 ± 0.10	0.21 ± 0.04	< 0.32	-1.00 ± 0.00	24.42	0.943
N1_95	J160916.3+543211	16:09:16.33	+54:32:11.1	0.79	44.7	9.7	0.63 ± 0.11	0.21 ± 0.04	< 0.43	-1.00 ± 0.00	23.27	0.508
N1_96	J161120.3+543508	16:11:20.30	+54:35:08.4	0.73	32.3	7.9	0.45 ± 0.09	< 0.07	1.16 ± 0.22	1.00 ± 0.00	17.19	0.029
N1_97	J161108.3+543250	16:11:08.38	+54:32:50.6	0.64	29.0	8.5	0.39 ± 0.08	0.18 ± 0.04	< 0.32	-1.00 ± 0.00	23.03	0.019
N1_98	J161107.0+543538	16:11:07.08	+54:35:38.6	0.71	16.2	5.2	0.22 ± 0.06	0.07 ± 0.02	< 0.32	-1.00 ± 0.00	> 25.20	—
N1_99	J161102.8+542959	16:11:02.81	+54:29:59.5	0.68	43.4	11.1	0.70 ± 0.12	0.14 ± 0.03	0.53 ± 0.16	-0.02 ± 0.20	> 25.20	—
N1_100	J161102.0+543826	16:11:02.02	+54:38:26.7	0.76	23.3	6.6	0.32 ± 0.07	0.12 ± 0.03	< 0.36	-1.00 ± 0.00	24.34	0.061
N1_101	J161051.9+543006	16:10:51.99	+54:30:06.9	0.66	12.7	4.2	0.17 ± 0.05	< 0.05	< 0.28	—	> 25.20	—
N1_102	J161051.6+543446	16:10:51.62	+54:34:46.9	0.69	14.3	4.6	0.18 ± 0.05	< 0.05	0.34 ± 0.11	1.00 ± 0.00	21.27	0.529
N1_103	J161048.2+542547	16:10:48.20	+54:25:47.9	0.87	24.8	6.0	0.35 ± 0.08	0.10 ± 0.03	< 0.40	-1.00 ± 0.00	> 25.20	—
N1_104	J161046.6+542437	16:10:46.63	+54:24:37.5	0.72	74.6	14.5	1.14 ± 0.15	0.48 ± 0.06	0.64 ± 0.19	-0.50 ± 0.14	22.66	0.087
N1_106	J161017.4+543149	16:10:17.40	+54:31:49.2	0.72	11.5	3.8	0.14 ± 0.05	< 0.04	< 0.20	—	25.01	0.618
N1_107	J161011.9+543352	16:10:11.98	+54:33:52.5	0.67	8.8	3.2	0.13 ± 0.05	< 0.05	< 0.22	—	> 25.20	—
N1_108	J161004.9+542636	16:10:04.99	+54:26:36.9	0.65	40.4	11.5	0.64 ± 0.11	0.23 ± 0.05	< 0.39	-1.00 ± 0.00	23.08	0.020
N1_110	J160951.7+543358	16:09:51.79	+54:33:58.1	0.75	10.8	3.6	0.14 ± 0.05	< 0.05	0.30 ± 0.10	1.00 ± 0.00	> 25.20	—
N1_111	J160948.7+542647	16:09:48.71	+54:26:47.1	0.61	28.6	8.8	0.40 ± 0.08	0.17 ± 0.04	< 0.37	-1.00 ± 0.00	> 25.20	—
N1_112	J160948.2+543611	16:09:48.20	+54:36:11.3	0.70	17.9	5.2	0.24 ± 0.06	< 0.05	0.47 ± 0.14	1.00 ± 0.00	22.45	0.036
N1_113	J161126.3+543528	16:11:26.36	+54:35:28.7	1.06	32.1	6.7	0.51 ± 0.11	0.15 ± 0.04	0.46 ± 0.16	-0.13 ± 0.22	24.23	0.243
N1_114	J161103.8+543303	16:11:03.83	+54:33:03.1	0.81	15.2	4.5	0.21 ± 0.06	< 0.06	< 0.31	—	21.36	0.029
N1_115	J161029.8+542401	16:10:29.86	+54:24:01.6	0.88	23.3	6.0	0.38 ± 0.09	0.16 ± 0.04	< 0.49	-1.00 ± 0.00	17.71	0.994
N1_116	J161021.6+542608	16:10:21.67	+54:26:08.0	0.89	11.4	3.7	0.17 ± 0.06	< 0.06	< 0.34	—	24.42	0.392
N1_117	J161018.4+542733	16:10:18.49	+54:27:33.4	0.77	18.5	5.3	0.24 ± 0.06	< 0.05	< 0.28	—	> 25.20	—
N1_118	J161005.2+543909	16:10:05.23	+54:39:09.7	0.85	13.6	4.1	0.17 ± 0.05	< 0.05	< 0.28	—	22.74	0.668
N1_119	J160953.7+543755	16:09:53.78	+54:37:55.6	0.68	12.8	4.3	0.17 ± 0.05	< 0.06	0.33 ± 0.12	1.00 ± 0.00	22.59	0.013

ID	CXOEN1	RA (J2000)	Dec (J2000)	Err (arcsec)	Net Cts	S/N	Flux ($\times 10^{-14}$ erg cm^{-2} s^{-1}) (0.5–8keV)	(0.5–2keV)	(2–8keV)	HR	r′	s/g
N1_121	J160932.6+543436	16:09:32.63	+54:34:36.9	0.78	13.1	4.2	0.18 ± 0.06	< 0.06	0.56 ± 0.15	1.00 ± 0.00	24.37	0.025
N1_123	J161137.0+542541	16:11:37.00	+54:25:41.6	0.99	136.6	12.4	2.11 ± 0.24	0.56 ± 0.08	2.81 ± 0.49	0.11 ± 0.12	—	—
N1_124	J161131.4+543706	16:11:31.40	+54:37:06.2	1.28	18.1	3.9	0.29 ± 0.09	0.15 ± 0.04	< 0.62	-1.00 ± 0.00	21.86	0.046
N1_125	J161123.7+542632	16:11:23.71	+54:26:32.7	0.99	85.2	9.7	1.22 ± 0.17	0.29 ± 0.06	1.74 ± 0.35	0.20 ± 0.15	23.83	0.013
N1_126	J161122.0+542217	16:11:22.00	+54:22:17.0	1.13	214.9	12.7	3.27 ± 0.33	1.14 ± 0.12	2.66 ± 0.53	-0.26 ± 0.10	> 25.20	—
N1_127	J161101.6+543030	16:11:01.64	+54:30:30.3	0.78	12.0	4.1	0.21 ± 0.07	0.09 ± 0.03	< 0.38	-1.00 ± 0.00	24.99	0.550
N1_128	J161043.4+543403	16:10:43.44	+54:34:03.9	0.72	12.8	4.0	0.16 ± 0.05	0.07 ± 0.02	< 0.23	-1.00 ± 0.00	> 25.20	—
N1_129	J161025.7+542328	16:10:25.78	+54:23:28.4	1.01	43.2	9.0	0.93 ± 0.17	0.47 ± 0.09	< 0.60	-1.00 ± 0.00	—	—
N1_131	J160943.6+543849	16:09:43.63	+54:38:49.9	0.80	14.1	4.4	0.19 ± 0.06	0.07 ± 0.02	< 0.34	-1.00 ± 0.00	> 25.20	—
N1_132	J160920.4+543103	16:09:20.49	+54:31:03.3	0.82	15.9	4.6	0.23 ± 0.07	0.06 ± 0.02	0.32 ± 0.13	0.13 ± 0.28	—	—
N1_133	J160916.9+542811	16:09:16.98	+54:28:11.1	0.99	33.5	6.5	0.51 ± 0.11	0.11 ± 0.03	0.68 ± 0.22	0.21 ± 0.24	25.04	0.767
N1_135	J161132.0+542309	16:11:32.03	+54:23:09.1	1.30	197.5	11.2	3.08 ± 0.34	1.27 ± 0.13	—	-1.00 ± 0.00	—	—
N1_136	J161007.7+543834	16:10:07.74	+54:38:34.4	0.79	16.1	4.8	0.22 ± 0.06	0.07 ± 0.03	< 0.28	-1.00 ± 0.00	20.39	0.019
N1_137	J161101.6+543422	16:11:01.64	+54:34:22.9	0.80	11.7	3.6	0.15 ± 0.05	< 0.05	0.31 ± 0.11	1.00 ± 0.00	> 25.20	—
N1_138	J161109.3+542035	16:11:09.31	+54:20:35.4	1.42	62.6	5.0	0.96 ± 0.22	0.40 ± 0.08	—	-1.00 ± 0.00	21.49	0.136
N1_139	J160942.5+542709	16:09:42.56	+54:27:09.1	0.97	17.4	4.7	0.24 ± 0.07	0.10 ± 0.03	< 0.38	-1.00 ± 0.00	23.53	0.270
N1_140	J161058.4+543852	16:10:58.45	+54:38:52.5	0.91	14.0	4.4	0.19 ± 0.06	0.08 ± 0.03	< 0.35	-1.00 ± 0.00	23.80	0.099
N1_141	J160943.1+544152	16:09:43.19	+54:41:52.3	1.20	18.4	4.0	0.26 ± 0.08	0.11 ± 0.03	< 0.48	-1.00 ± 0.00	23.95	0.965
N1_142	J161113.5+543612	16:11:13.53	+54:36:12.6	0.99	13.7	3.7	0.20 ± 0.06	0.07 ± 0.03	< 0.39	-1.00 ± 0.00	22.88	0.019
N1_143	J160940.1+543713	16:09:40.15	+54:37:13.5	0.82	11.2	3.6	0.15 ± 0.05	< 0.06	0.35 ± 0.12	1.00 ± 0.00	23.23	0.026
N1_144	J160941.8+543127	16:09:41.83	+54:31:27.5	0.77	10.1	3.4	0.14 ± 0.05	< 0.06	0.34 ± 0.12	1.00 ± 0.00	—	—
N1_145	J161048.8+543205	16:10:48.84	+54:32:05.9	0.78	9.5	3.1	0.12 ± 0.05	< 0.05	< 0.25	—	23.52	0.045
N1_146	J160946.1+543624	16:09:46.18	+54:36:24.5	0.74	12.0	3.8	0.15 ± 0.05	0.06 ± 0.02	< 0.27	-1.00 ± 0.00	—	—
N1_147	J160909.8+542841	16:09:09.89	+54:28:41.4	1.67	10.9	3.2	< 0.31	0.09 ± 0.03	< 0.66	-1.00 ± 0.00	—	—
N1_148	J161037.9+543336	16:10:37.92	+54:33:36.9	0.67	7.1	3.1	< 0.11	0.05 ± 0.02	< 0.21	-1.00 ± 0.00	—	—
N1_149	J160923.1+542810	16:09:23.15	+54:28:10.4	1.01	10.2	3.0	< 0.20	< 0.08	0.36 ± 0.14	1.00 ± 0.00	—	—

Table E.2: Chandra sources in the ELAIS N2 field.

ID	CXOEN2	RA (J2000)	Dec (J2000)	Err (arcsec)	Net Cts	S/N	Flux ($\times 10^{-14}$ erg cm^{-2} s^{-1}) (0.5–8keV)	(0.5–2keV)	(2–8keV)	HR	r′	s/g
N2_1	J163733.4+410309	16:37:33.41	+41:03:09.3	0.44	638.9	101.7	8.73 ± 0.35	3.20 ± 0.15	6.32 ± 0.48	-0.34 ± 0.04	21.69	0.103
N2_2	J163730.2+410049	16:37:30.27	+41:00:49.8	0.71	52.6	11.0	0.71 ± 0.11	0.16 ± 0.04	0.77 ± 0.18	0.08 ± 0.16	24.59	0.564
N2_4	J163720.5+410402	16:37:20.50	+41:04:02.2	0.59	11.6	4.2	0.17 ± 0.05	0.06 ± 0.02	< 0.32	-1.00 ± 0.00	22.84	0.358
N2_5	J163720.5+410626	16:37:20.58	+41:06:26.6	0.49	216.6	45.4	2.87 ± 0.20	0.99 ± 0.08	2.33 ± 0.29	-0.26 ± 0.07	20.97	1.000
N2_6	J163715.2+410443	16:37:15.24	+41:04:43.1	0.58	18.8	6.3	0.24 ± 0.06	0.08 ± 0.02	< 0.28	-1.00 ± 0.00	> 25.20	—
N2_7	J163712.3+410139	16:37:12.38	+41:01:39.2	0.43	94.0	29.6	1.29 ± 0.14	0.48 ± 0.06	0.99 ± 0.19	-0.32 ± 0.11	22.25	0.663
N2_8	J163712.3+410131	16:37:12.36	+41:01:31.7	0.54	15.6	5.6	0.21 ± 0.06	0.08 ± 0.02	< 0.26	-1.00 ± 0.00	22.65	0.608
N2_9	J163710.0+405643	16:37:10.04	+40:56:43.2	0.43	338.9	73.8	4.74 ± 0.26	1.97 ± 0.12	2.39 ± 0.30	-0.53 ± 0.06	19.97	0.985
N2_10	J163709.2+410457	16:37:09.20	+41:04:57.5	0.52	41.0	12.1	0.51 ± 0.09	0.21 ± 0.04	0.26 ± 0.10	-0.52 ± 0.19	22.53	0.381
N2_11	J163706.7+410501	16:37:06.72	+41:05:01.7	0.77	10.1	3.5	0.13 ± 0.05	< 0.05	< 0.25	—	24.71	0.650
N2_12	J163706.0+410054	16:37:06.00	+41:00:54.6	0.57	10.4	3.7	0.13 ± 0.04	< 0.05	< 0.23	—	22.22	0.032
N2_13	J163705.0+405749	16:37:05.03	+40:57:49.2	0.61	19.7	6.1	0.25 ± 0.06	< 0.05	0.57 ± 0.14	1.00 ± 0.00	—	—
N2_14	J163704.9+410509	16:37:04.94	+41:05:09.0	0.44	95.4	28.8	1.19 ± 0.12	0.29 ± 0.04	1.50 ± 0.22	0.12 ± 0.11	—	—
N2_15	J163704.4+405625	16:37:04.41	+40:56:25.1	0.63	15.6	5.2	0.22 ± 0.06	0.08 ± 0.03	< 0.31	-1.00 ± 0.00	24.66	0.772
N2_16	J163703.2+410103	16:37:03.27	+41:01:03.3	0.48	11.8	4.3	0.14 ± 0.05	0.06 ± 0.02	< 0.22	-1.00 ± 0.00	> 25.20	—
N2_17	J163703.1+405157	16:37:03.15	+40:51:57.0	0.66	180.1	25.0	2.57 ± 0.21	0.65 ± 0.07	3.04 ± 0.37	0.08 ± 0.08	21.03	0.354
N2_18	J163700.6+410555	16:37:00.64	+41:05:55.7	0.42	251.7	69.1	3.13 ± 0.20	1.25 ± 0.09	1.85 ± 0.24	-0.46 ± 0.07	20.03	0.984
N2_19	J163658.8+405727	16:36:58.82	+40:57:27.8	0.54	23.3	7.5	0.32 ± 0.07	0.09 ± 0.03	0.41 ± 0.12	0.10 ± 0.22	22.46	0.331
N2_20	J163658.3+410537	16:36:58.31	+41:05:37.1	0.49	31.2	9.9	0.38 ± 0.07	0.12 ± 0.03	0.41 ± 0.12	-0.07 ± 0.19	23.67	0.313
N2_21	J163658.0+405821	16:36:58.07	+40:58:21.1	0.41	175.2	52.2	2.15 ± 0.16	0.83 ± 0.07	1.39 ± 0.21	-0.41 ± 0.08	25.19	0.594
N2_22	J163656.6+410449	16:36:56.63	+41:04:49.7	0.47	34.4	11.1	0.42 ± 0.08	0.17 ± 0.03	0.24 ± 0.09	-0.48 ± 0.20	22.40	0.044
N2_23	J163656.0+410625	16:36:56.04	+41:06:25.1	0.67	11.1	3.8	0.15 ± 0.05	< 0.05	0.38 ± 0.12	1.00 ± 0.00	19.83	0.029
N2_24	J163655.7+405652	16:36:55.72	+40:56:52.4	0.46	97.2	25.9	1.27 ± 0.13	0.32 ± 0.05	1.53 ± 0.23	0.09 ± 0.11	21.86	0.026
N2_25	J163655.7+405910	16:36:55.79	+40:59:10.5	0.43	84.7	24.5	1.02 ± 0.11	0.21 ± 0.04	1.47 ± 0.21	0.26 ± 0.12	23.07	0.995
N2_26	J163655.5+410809	16:36:55.56	+41:08:09.9	0.61	49.2	13.2	0.63 ± 0.10	0.28 ± 0.04	< 0.30	-1.00 ± 0.00	19.95	0.984
N2_27	J163655.3+410714	16:36:55.37	+41:07:14.7	0.64	28.2	8.4	0.39 ± 0.08	0.14 ± 0.03	< 0.29	-1.00 ± 0.00	21.47	0.983

ID	CXOEN2	RA (J2000)	Dec (J2000)	Err (arcsec)	Net Cts	S/N	Flux ($\times 10^{-14}$ erg cm^{-2} s^{-1}) (0.5–8keV)	(0.5–2keV)	(2–8keV)	HR	r′	s/g
N2_28	J163655.2+405944	16:36:55.21	+40:59:44.1	0.47	32.1	11.0	0.38 ± 0.07	0.11 ± 0.03	0.38 ± 0.11	−0.05 ± 0.19	> 25.20	—
N2_29	J163655.1+410152	16:36:55.16	+41:01:52.4	0.55	14.2	4.9	0.17 ± 0.05	0.06 ± 0.02	< 0.20	−1.00 ± 0.00	> 25.20	—
N2_32	J163653.2+405917	16:36:53.26	+40:59:17.3	0.55	10.7	3.9	0.13 ± 0.04	< 0.04	0.28 ± 0.10	1.00 ± 0.00	22.59	0.058
N2_33	J163651.6+405600	16:36:51.69	+40:56:00.4	0.69	24.0	6.7	0.31 ± 0.07	< 0.05	0.52 ± 0.14	1.00 ± 0.00	19.54	0.029
N2_34	J163650.6+405840	16:36:50.63	+40:58:40.6	0.47	35.9	11.2	0.43 ± 0.08	0.14 ± 0.03	0.39 ± 0.11	−0.20 ± 0.18	> 25.20	—
N2_35	J163649.1+410324	16:36:49.18	+41:03:24.3	0.83	16.2	5.7	0.44 ± 0.12	< 0.09	< 0.39	—	24.50	0.623
N2_37	J163647.3+410659	16:36:47.30	+41:06:59.0	0.50	60.2	16.9	0.78 ± 0.10	0.17 ± 0.04	1.10 ± 0.19	0.22 ± 0.14	24.15	0.757
N2_38	J163647.1+410334	16:36:47.15	+41:03:34.8	0.42	142.6	41.1	1.79 ± 0.15	0.76 ± 0.07	0.85 ± 0.17	−0.56 ± 0.10	20.22	0.984
N2_39	J163646.5+405729	16:36:46.57	+40:57:29.1	0.53	21.4	6.9	0.26 ± 0.06	0.11 ± 0.03	< 0.23	−1.00 ± 0.00	> 25.20	—
N2_40	J163645.5+410313	16:36:45.51	+41:03:13.9	0.51	25.4	8.2	0.32 ± 0.07	0.09 ± 0.03	0.33 ± 0.11	−0.05 ± 0.21	24.93	0.483
N2_41	J163644.7+405540	16:36:44.73	+40:55:40.6	0.45	139.9	35.2	1.79 ± 0.16	0.76 ± 0.07	0.69 ± 0.16	−0.63 ± 0.10	21.87	0.980
N2_42	J163644.6+405643	16:36:44.68	+40:56:43.6	0.56	32.7	9.5	0.41 ± 0.08	0.17 ± 0.03	< 0.25	−1.00 ± 0.00	19.15	0.029
N2_43	J163642.7+405514	16:36:42.71	+40:55:14.9	0.58	46.7	12.8	0.60 ± 0.09	0.23 ± 0.04	< 0.29	−1.00 ± 0.00	—	—
N2_44	J163641.3+405550	16:36:41.35	+40:55:50.2	0.48	80.9	21.3	1.03 ± 0.12	0.35 ± 0.05	0.86 ± 0.17	−0.24 ± 0.12	20.75	0.924
N2_46	J163639.3+410259	16:36:39.34	+41:02:59.5	0.55	13.2	4.6	0.15 ± 0.05	0.05 ± 0.02	< 0.19	−1.00 ± 0.00	24.24	0.028
N2_47	J163636.2+410509	16:36:36.21	+41:05:09.5	0.46	31.5	10.3	0.38 ± 0.07	0.15 ± 0.03	0.27 ± 0.10	−0.37 ± 0.20	23.12	0.763
N2_48	J163633.6+410534	16:36:33.66	+41:05:34.3	0.45	76.6	22.0	0.93 ± 0.11	0.40 ± 0.05	0.52 ± 0.13	−0.51 ± 0.13	21.78	0.983
N2_51	J163630.5+405651	16:36:30.54	+40:56:51.8	0.44	291.5	72.1	6.09 ± 0.37	1.58 ± 0.14	7.54 ± 0.65	0.09 ± 0.06	23.81	0.595
N2_52	J163629.7+410222	16:36:29.71	+41:02:22.7	0.41	312.1	79.2	3.78 ± 0.22	1.42 ± 0.10	2.60 ± 0.28	−0.37 ± 0.06	15.86	0.029
N2_54	J163628.1+405527	16:36:28.13	+40:55:27.5	0.42	604.8	121.2	7.92 ± 0.33	2.93 ± 0.14	5.78 ± 0.44	−0.34 ± 0.04	20.96	0.771
N2_55	J163627.4+410615	16:36:27.47	+41:06:15.4	0.73	18.3	5.5	0.23 ± 0.06	< 0.05	0.34 ± 0.11	1.00 ± 0.00	21.99	0.411
N2_56	J163625.4+405741	16:36:25.46	+40:57:41.4	0.46	138.3	34.0	1.77 ± 0.16	0.75 ± 0.07	0.76 ± 0.16	−0.60 ± 0.10	21.30	0.983
N2_57	J163623.0+410015	16:36:23.07	+41:00:15.0	0.52	32.8	10.2	0.41 ± 0.08	0.17 ± 0.03	0.25 ± 0.09	−0.45 ± 0.20	19.61	0.030
N2_58	J163622.5+410641	16:36:22.54	+41:06:41.6	0.56	59.6	14.8	0.76 ± 0.11	0.39 ± 0.05	< 0.30	−1.00 ± 0.00	16.05	1.000
N2_59	J163622.4+410927	16:36:22.49	+41:09:27.7	0.61	104.7	20.0	1.39 ± 0.15	0.55 ± 0.06	0.74 ± 0.19	−0.50 ± 0.12	22.33	0.956
N2_60	J163619.2+410436	16:36:19.23	+41:04:36.9	0.52	51.0	14.2	0.65 ± 0.10	0.26 ± 0.04	< 0.28	−1.00 ± 0.00	23.43	0.966

ID	CXOEN2	RA (J2000)	Dec (J2000)	Err (arcsec)	Net Cts	S/N	Flux ($\times 10^{-14}$ erg cm^{-2} s^{-1}) (0.5–8keV)	(0.5–2keV)	(2–8keV)	HR	r′	s/g
N2_61	J163618.2+410038	16:36:18.23	+41:00:38.6	0.57	38.5	11.0	0.52 ± 0.09	0.18 ± 0.04	0.39 ± 0.12	-0.30 ± 0.18	24.19	0.921
N2_62	J163616.4+405748	16:36:16.42	+40:57:48.3	0.59	29.9	8.8	0.39 ± 0.08	0.16 ± 0.03	< 0.31	-1.00 ± 0.00	—	—
N2_63	J163615.6+405716	16:36:15.60	+40:57:16.6	0.71	20.3	6.1	0.27 ± 0.07	0.09 ± 0.03	< 0.32	-1.00 ± 0.00	17.05	0.029
N2_64	J163614.4+410349	16:36:14.46	+41:03:49.1	0.53	78.0	19.0	1.00 ± 0.12	0.37 ± 0.05	0.72 ± 0.16	-0.34 ± 0.13	22.87	0.939
N2_65	J163612.1+410242	16:36:12.16	+41:02:42.7	0.62	39.5	10.7	0.51 ± 0.09	0.20 ± 0.04	< 0.30	-1.00 ± 0.00	21.64	0.032
N2_66	J163606.7+410440	16:36:06.79	+41:04:40.0	0.71	79.4	15.0	1.17 ± 0.15	0.34 ± 0.05	1.15 ± 0.23	-0.08 ± 0.13	> 25.20	—
N2_67	J163555.7+410054	16:35:55.72	+41:00:54.5	0.95	53.1	8.9	0.79 ± 0.13	0.23 ± 0.05	0.53 ± 0.17	-0.26 ± 0.18	20.75	0.034
N2_68	J163725.2+410021	16:37:25.26	+41:00:21.1	0.69	17.5	5.3	0.23 ± 0.06	0.08 ± 0.03	< 0.33	-1.00 ± 0.00	23.70	0.964
N2_71	J163710.8+405402	16:37:10.81	+40:54:02.4	0.77	30.7	7.1	0.42 ± 0.09	0.13 ± 0.03	< 0.40	-1.00 ± 0.00	22.92	0.969
N2_72	J163657.7+410021	16:36:57.74	+41:00:21.5	0.73	11.9	3.7	0.15 ± 0.05	0.08 ± 0.02	< 0.21	-1.00 ± 0.00	23.38	0.012
N2_73	J163635.8+405325	16:36:35.86	+40:53:25.6	0.78	46.1	9.8	0.62 ± 0.10	0.19 ± 0.04	0.35 ± 0.13	-0.38 ± 0.19	22.97	0.038
N2_74	J163632.9+411111	16:36:32.95	+41:11:11.4	0.88	53.2	10.0	0.72 ± 0.11	0.29 ± 0.05	< 0.46	-1.00 ± 0.00	> 25.20	—
N2_75	J163632.7+410513	16:36:32.78	+41:05:13.7	0.69	20.4	6.2	0.25 ± 0.06	< 0.05	0.32 ± 0.11	1.00 ± 0.00	20.48	0.053
N2_76	J163632.6+410552	16:36:32.64	+41:05:52.7	0.65	12.7	4.2	0.15 ± 0.05	0.05 ± 0.02	< 0.25	-1.00 ± 0.00	> 25.20	—
N2_77	J163625.2+410228	16:36:25.25	+41:02:28.2	0.68	12.3	3.9	0.15 ± 0.05	< 0.05	0.31 ± 0.11	1.00 ± 0.00	24.16	0.132
N2_78	J163624.1+410821	16:36:24.12	+41:08:21.2	0.77	36.3	8.3	0.47 ± 0.09	0.17 ± 0.04	< 0.35	-1.00 ± 0.00	24.79	0.784
N2_79	J163620.6+405714	16:36:20.68	+40:57:14.8	0.75	24.7	7.1	0.32 ± 0.07	< 0.06	0.55 ± 0.14	1.00 ± 0.00	22.20	0.225
N2_80	J163617.9+405636	16:36:17.96	+40:56:36.5	0.72	30.1	8.0	0.40 ± 0.08	0.08 ± 0.03	0.39 ± 0.12	0.09 ± 0.22	23.58	0.326
N2_81	J163731.1+410410	16:37:31.15	+41:04:10.8	0.87	21.7	5.4	0.31 ± 0.08	0.09 ± 0.03	< 0.41	-1.00 ± 0.00	> 25.20	—
N2_82	J163718.1+410600	16:37:18.16	+41:06:00.1	0.72	11.0	3.7	0.14 ± 0.05	0.05 ± 0.02	< 0.32	-1.00 ± 0.00	24.08	0.233
N2_83	J163717.6+410324	16:37:17.66	+41:03:24.1	0.83	11.7	3.9	0.17 ± 0.06	0.09 ± 0.03	< 0.32	-1.00 ± 0.00	> 25.20	—
N2_84	J163708.3+410526	16:37:08.37	+41:05:26.0	0.72	11.2	3.9	0.15 ± 0.05	< 0.05	< 0.27	—	> 25.20	—
N2_85	J163648.0+410354	16:36:48.04	+41:03:54.9	0.71	10.8	3.6	0.14 ± 0.05	< 0.04	0.27 ± 0.10	1.00 ± 0.00	> 25.20	—
N2_86	J163633.7+411102	16:36:33.71	+41:11:02.4	0.83	42.6	9.0	0.61 ± 0.11	0.19 ± 0.04	0.76 ± 0.20	0.01 ± 0.17	23.38	0.135
N2_87	J163627.6+405416	16:36:27.62	+40:54:16.1	0.99	20.8	5.0	0.30 ± 0.08	0.10 ± 0.03	< 0.37	-1.00 ± 0.00	22.10	0.982
N2_88	J163616.0+405500	16:36:16.01	+40:55:00.9	0.82	57.2	11.9	0.94 ± 0.14	0.30 ± 0.06	0.62 ± 0.18	-0.32 ± 0.16	—	—

ID	CXOEN2	RA (J2000)	Dec (J2000)	Err (arcsec)	Net Cts	S/N	Flux ($\times 10^{-14}$ erg cm^{-2} s^{-1}) (0.5–8keV)	(0.5–2keV)	(2–8keV)	HR	r′	s/g
N2_89	J163615.0+405639	16:36:15.03	+40:56:39.3	0.81	18.5	5.3	0.26 ± 0.07	0.07 ± 0.02	< 0.36	-1.00 ± 0.00	21.39	0.038
N2_90	J163612.3+410731	16:36:12.34	+41:07:31.3	0.81	48.7	9.5	0.66 ± 0.11	0.18 ± 0.04	0.38 ± 0.13	-0.31 ± 0.19	22.39	0.776
N2_91	J163604.3+405646	16:36:04.31	+40:56:46.8	0.99	22.9	5.5	0.32 ± 0.08	0.09 ± 0.03	< 0.43	-1.00 ± 0.00	> 25.20	—
N2_92	J163559.3+410116	16:35:59.30	+41:01:16.0	0.73	14.7	4.3	0.21 ± 0.06	0.09 ± 0.03	< 0.43	-1.00 ± 0.00	23.43	0.022
N2_93	J163735.5+410448	16:37:35.54	+41:04:48.9	0.97	28.4	6.5	0.39 ± 0.09	0.13 ± 0.03	< 0.45	-1.00 ± 0.00	> 25.20	—
N2_94	J163734.5+405046	16:37:34.51	+40:50:46.7	0.95	395.9	22.4	5.92 ± 0.39	1.78 ± 0.14	5.54 ± 0.67	-0.13 ± 0.07	> 25.20	—
N2_96	J163608.4+410404	16:36:08.45	+41:04:04.1	0.73	13.3	4.2	0.19 ± 0.06	0.08 ± 0.02	< 0.36	-1.00 ± 0.00	19.35	0.611
N2_97	J163602.6+405927	16:36:02.66	+40:59:27.3	1.03	26.0	5.7	0.35 ± 0.08	< 0.07	< 0.39	—	> 25.20	—
N2_98	J163623.4+410859	16:36:23.47	+41:08:59.0	0.88	27.9	6.3	0.37 ± 0.08	0.06 ± 0.02	0.40 ± 0.13	0.22 ± 0.25	18.33	0.984
N2_99	J163734.5+405212	16:37:34.56	+40:52:12.8	1.12	108.3	8.5	1.53 ± 0.22	0.59 ± 0.08	—	-1.00 ± 0.00	15.03	0.060
N2_100	J163729.9+405349	16:37:29.99	+40:53:49.3	1.04	23.9	4.1	0.34 ± 0.10	0.20 ± 0.05	—	-1.00 ± 0.00	24.16	0.126
N2_101	J163633.8+410731	16:36:33.84	+41:07:31.0	0.86	15.4	4.7	0.21 ± 0.06	< 0.06	< 0.30	—	> 25.20	—
N2_102	J163725.6+405811	16:37:25.68	+40:58:11.0	0.83	12.4	4.9	0.47 ± 0.14	0.19 ± 0.06	< 0.69	-1.00 ± 0.00	22.73	0.969
N2_103	J163639.9+405322	16:36:39.97	+40:53:22.8	0.98	14.1	4.2	0.19 ± 0.06	< 0.06	< 0.38	—	23.55	0.940
N2_104	J163640.7+410449	16:36:40.77	+41:04:49.8	0.76	10.6	3.5	0.13 ± 0.05	< 0.05	< 0.22	—	22.87	0.120
N2_105	J163640.9+410840	16:36:40.90	+41:08:40.7	0.71	12.3	4.0	0.16 ± 0.05	< 0.06	< 0.31	—	20.70	0.129
N2_106	J163642.3+410520	16:36:42.33	+41:05:20.8	0.75	11.1	3.5	0.14 ± 0.05	0.05 ± 0.02	< 0.23	-1.00 ± 0.00	—	—
N2_107	J163608.4+410507	16:36:08.41	+41:05:07.0	0.86	12.1	3.4	0.18 ± 0.06	0.10 ± 0.03	< 0.39	-1.00 ± 0.00	17.60	0.035
N2_108	J163613.4+405806	16:36:13.45	+40:58:06.4	0.82	9.7	3.2	0.13 ± 0.05	< 0.06	< 0.32	—	> 25.20	—
N2_109	J163730.7+405152	16:37:30.77	+40:51:52.6	1.23	31.2	3.9	0.44 ± 0.13	—	—	—	17.20	0.029
N2_110	J163708.0+410840	16:37:08.04	+41:08:40.1	1.31	8.3	3.2	< 0.20	0.08 ± 0.03	< 0.48	-1.00 ± 0.00	—	—
N2_111	J163627.5+410228	16:36:27.50	+41:02:28.6	0.59	7.1	3.2	< 0.11	0.05 ± 0.02	< 0.23	-1.00 ± 0.00	—	—
N2_112	J163723.8+410133	16:37:23.83	+41:01:33.3	0.88	7.6	3.1	< 0.14	0.06 ± 0.02	< 0.32	-1.00 ± 0.00	—	—
N2_113	J163621.4+410049	16:36:21.42	+41:00:49.9	0.98	10.0	3.4	< 0.12	< 0.05	0.30 ± 0.11	1.00 ± 0.00	—	—
N2_114	J163631.8+410432	16:36:31.82	+41:04:32.7	0.59	7.6	3.1	< 0.12	< 0.05	0.24 ± 0.09	1.00 ± 0.00	—	—

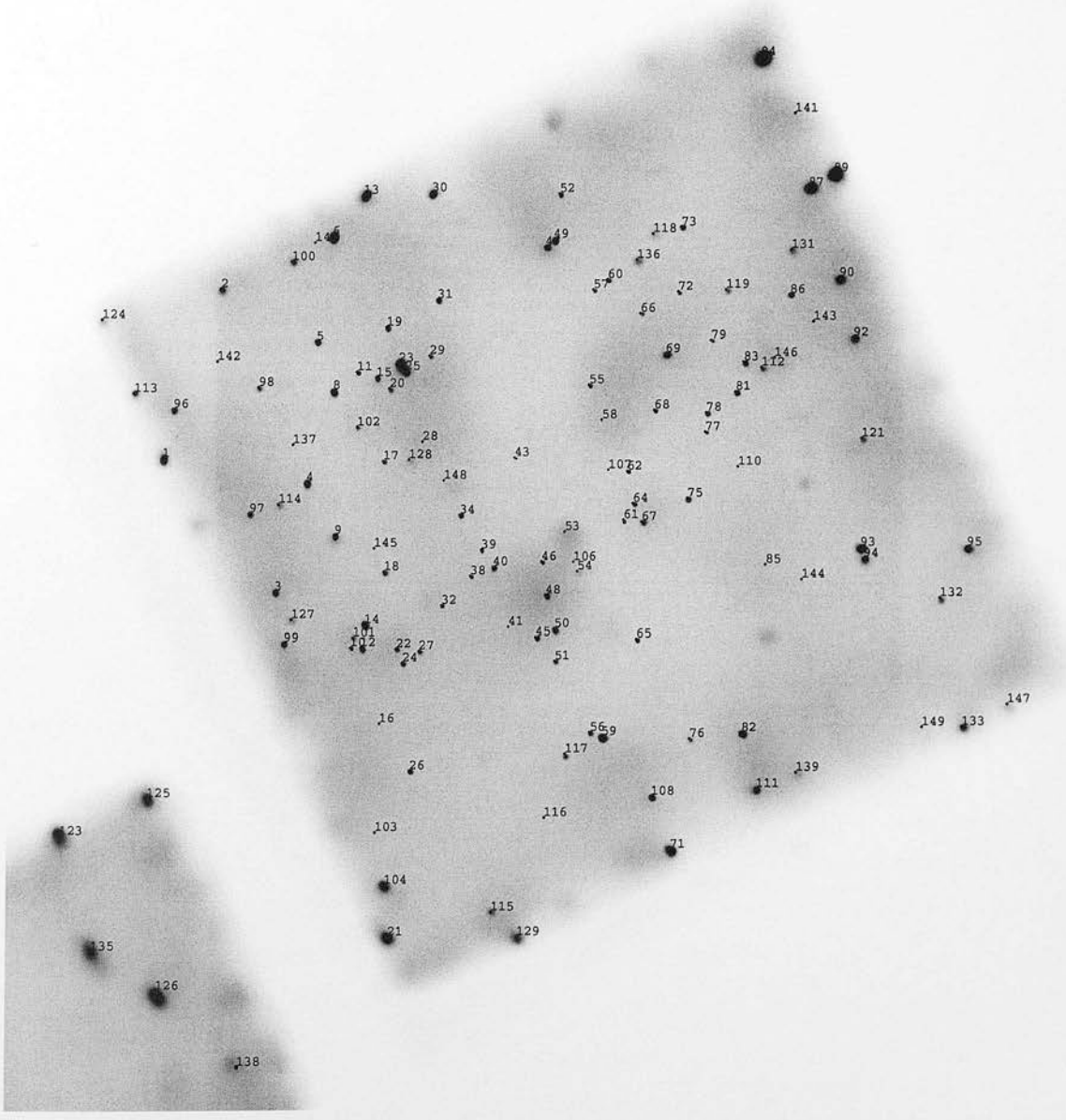

Figure E.1: Source positions in the Chandra image of region N1.

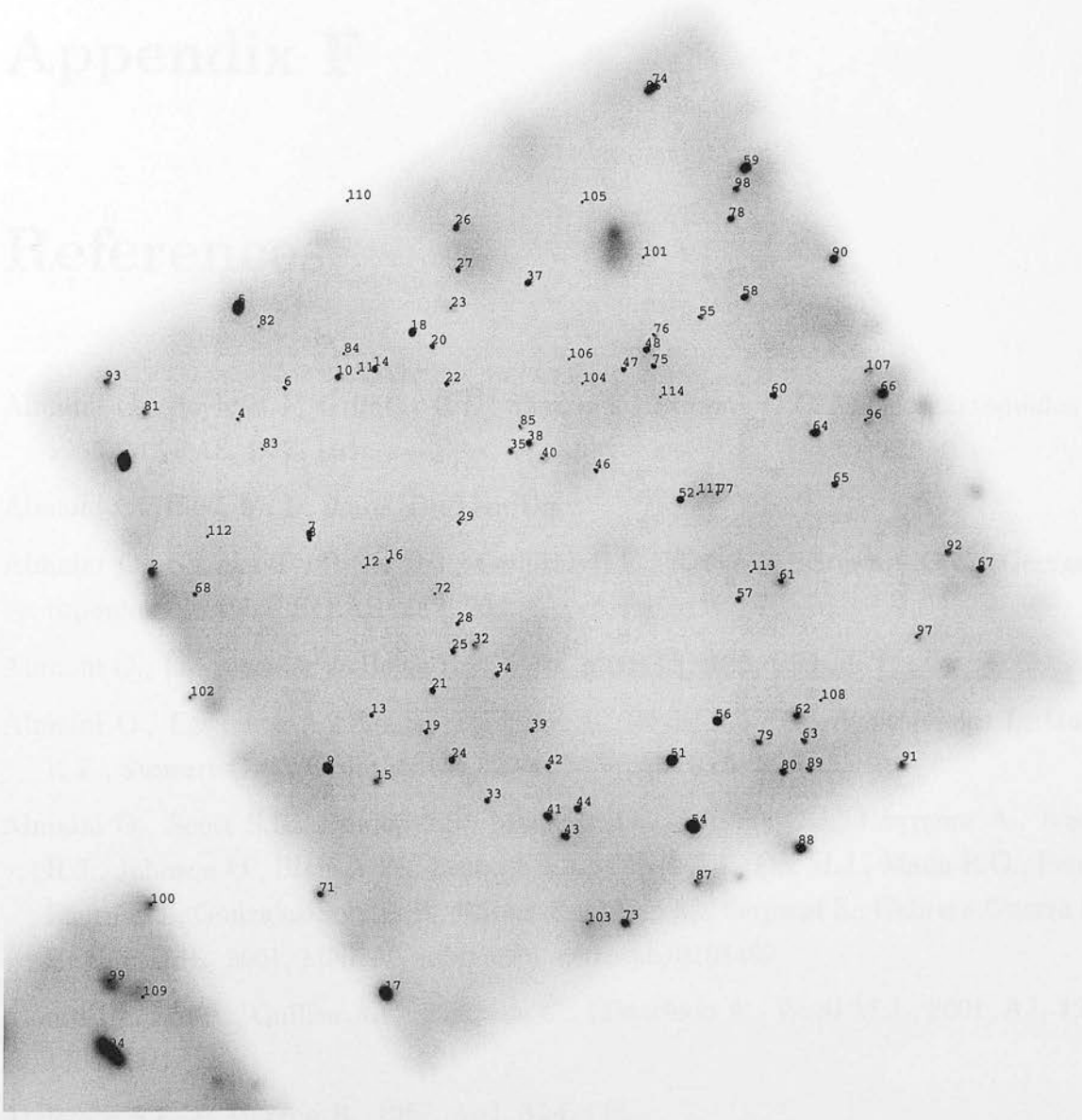

Figure E.2: Source positions in the Chandra image of region N2.

Appendix F

References

Almaini O., Boyle B.J., Griffiths R.E., Shanks T., Stewart G.C. & Georgantopoulos I., 1995, MNRAS, **277**, L31

Almaini O., 1996, *Ph.D. thesis*, Durham Univ.

Almaini O., Shanks T., Boyle B.J., Griffiths R.E., Roche N., Stewart G.C., Georgantopoulos I., 1996, MNRAS, **282**, 295

Almaini O., Lawrence A. & Boyle B.J., 1999, MNRAS, **305**, L59

Almaini O., Lawrence A., Shanks T., Edge A., Boyle B.J., Georgantopoulos I., Gunn K.F., Stewart G.C., Griffiths R.E., 2000, MNRAS, **315**, 325

Almaini O., Scott S.E., Dunlop J.S., Manners J.C., Willott C.J., Lawrence A., Ivison R.J., Johnson O., Blain A.W., Peacock J.A., Oliver S.J., Fox M.J., Mann R.G., Perez-Fournon I., Gonzalez-Solares E., Rowan-Robinson M., Serjeant S., Cabrera-Guerra F., Hughes D.H., 2001, MNRAS submitted, astro-ph/0108400

Alonso-Herrero A., Quillen A.C., Simpson C., Efstathiou A., Ward M.J., 2001, AJ, **121**, 1369

Anderson S.F. & Margon B., 1987, ApJ, **314**, 111

Angel J.R.P., 1979, ApJ, **233**, 364

Antonucci R., 1993, ARA&A, **31**, 473

Antonucci R.R.J. & Miller J.S., 1985, ApJ, **297**, 621

Archibald E.N., Dunlop J.S., Hughes D.H., Rawlings S., Eales S.A., Ivison R.J., 2001a, MNRAS, **323**, 417

Archibald E.N., Dunlop J.S., Jimenez R., Friaca A.C.S., McLure R.J., Hughes D.H., 2001b, ApJ submitted, astro-ph/0108122

Aschenbach B., 1985, Rep. Prog. Phys., **48**, 579

Barger A.J., Cowie L.L., Steffen A.T., Hornschemeier A.E., Brandt W.N., Garmire G.P., 2001, ApJ, **560**, L23

Begelman M.C., 1994, in ASP Conf. Ser. 54, *'The Physics of Active Galaxies'*, eds. G.V. Bicknell, M.A. Dopita, & P.J. Quinn (San Francisco: ASP), 51

Bertin E., Arnouts S., 1996, A&AS, **117**, 393

Bohlin R.C., Savage B.D. & Drake J.F., 1978, ApJ, **224**, 132

Boller T., Brandt W.N., Fink H., 1996, A&A, **305**, 53

Bottinelli S., *et al.* 2002, in preparation

Boyle B.J., Fong R., Shanks T., Peterson B.A., 1990, MNRAS, **243**, 1

Boyle B.J., Griffiths R.E., Shanks T., Stewart G.C., Georgantopoulos I., 1994, MNRAS, **271**, 639

Boyle B.J., Wilkes B.J. & Elvis M., 1997, MNRAS, **285**, 511

Boyle B.J., Almaini O., Georgantopoulos I., Blair A.J., Stewart G.C., Griffiths R.E., Shanks T., Gunn K.F., 1998, MNRAS, **297**, L53

Brandt W.N., Alexander D.M., Hornschemeier A.E., Garmire G.P., Schneider D.P., Barger A.J., Bauer F.E., Broos P.S., Cowie L.L., Townsley L.K., Burrows D.N., Chartas G., Feigelson E.D., Griffiths R.E., Nousek J.A., Sargent W.L.W., 2001, AJ, **122**, 2810

Burnight T.R., 1949, Phys. Rev., **76**, 165

Cardelli J.A., Clayton G.C. & Mathis J.S., 1989, ApJ, **345**, 245

Carlberg R.G., 1990, ApJ, **350**, 505

Chiang J., Reynolds C.S., Blaes O.M., Nowak M.A., Murray N., Madejski G., Marshall H.L., & Magdziarz P., 2000, ApJ, **528**, 292

Chokshi A. & Turner E., 1992, MNRAS, **259**, 421

Chubb T.A., Friedman H., Kreplin R.W., Blake R.L., & Unzicker A.E., 1961, Mem. R. Sci. Liege. 5th ser. IV, 235

Ciliegi P., McMahon R.G., Miley G., Gruppioni C., Rowan-Robinson M., Cesarsky C., Danese L., Franceschini A., Genzel R., Lawrence A., Lemke D., Oliver S., Puget J.L., Rocca-Volmerange B., 1999, MNRAS, **302**, 222

Clavel J., Wamsteker W., & Glass I.S., 1989, ApJ, **337**, 236

Collinge M., Brandt W.N., Kaspi S., Crenshaw D.M., Elvis M., Kraemer S.B., Reynolds C.S., Sambruna R.M., Wills B.J., 2001, ApJ, **557**, 2

Comastri A., 1992, *Ph.D. thesis*, Bologna Univ.

Comastri A., Setti G., Zamorani G. & Hasinger G., 1995, A&A, **296**, 1

Comastri A., 2000, proc. *'Stellar Endpoints, AGNs and the Diffuse X-ray Background'*, eds. N.E. White, G. Malaguti & G.G.C. Palumbo, AIP 599, astro-ph/0003437

Compton A.H., 1923, Phil. Mag., **45**, 1121

Cowie L.L., Garmire G.P., Bautz M.W., Barger A.J., Brandt W.N., Hornschemeier A.E., 2002, ApJ in press, astro-ph/0201186

Crenshaw D.M., Kraemer S.B., Boggess A., Maran S.P., Mushotzky R.F., & Wu C.-C., 1999, ApJ, **516**, 750

Della Ceca R., Zamorani G., Maccacaro T., Wolter A., Griffiths R., Stocke J.T., Setti G., 1994, ApJ, **430**, 533

Della Ceca R., Castelli G., Braito V., Cagnoni I., & Maccacaro T., 1999, ApJ, **524**, 674

Di Matteo T., Esin A., Fabian A.C., & Narayan R., 1999, MNRAS, **305**, L1

Dopita M.A., 1997, PASA, **14**, 230

Eddington A.S., 1913, MNRAS, **73**, 359

Edelson R. & Malkan M.A., 1987, ApJ, **323**, 516

Edelson R., Nandra K., 1999, ApJ, **514**, 682

Edelson R., Koratkar A., Nandra K., Goad M., Peterson B.M., Collier S., Krolik J., Malkan M., Maoz D., O'Brien P., Shull J.M., Vaughan S., Warwick R., 2000, ApJ, **534**, 180

Efstathiou A. & Rowan-Robinson M., 1995, MNRAS, **273**, 649

Elbaz D., Cesarsky C.J., Chanial P., Aussel H., Franceschini A., Fadda D., Chary R.R., 2002, A&A, **384**, 848

Elvis M., Wilkes B.J., McDowell J.C., Green R.F., Bechtold J., Willner S.P., Oey M.S., Polomski E., Cutri R., 1994, ApJS, **95**, 1

Fabian A.C., George I.M., Miyoshi S., & Rees M.J., 1990, MNRAS, **242**, 14

Fabian A.C., Barcons X., Almaini O., Iwasawa K., 1998, MNRAS, **297**, L11

Fabian A.C., 1998b, *'Theory of Black Hole Accretion Discs'*, Cambridge Univ. Press, eds. Abramowicz M.A., Bjornsson G., & Pringle J.E., p123

Fabian A.C., 1999, MNRAS, **308**, L39

Fabian A.C. & Iwasawa K., 1999, MNRAS, **303**, L34

Fadda D., Flores H., Hasinger G., Franceschini A., Altieri B., Cesarsky C.J., Elbaz D., Ferrando Ph., 2002, A&A, **383**, 838

Ferrarese L. & Merritt D., 2000, ApJ, **539**, L9

Fixsen D.J., Dwek E., Mather J.C., Bennett C.L., Shafer R.A., 1998, ApJ, **508**, 123

Fox M.J., Efstathiou A., Rowan-Robinson M., Dunlop J.S, Scott S., Serjeant S., Mann R.G., Oliver S., Ivison R.J., Blain A., Almaini O., Hughes D., Willott C.J., Longair M., Lawrence A., Peacock J.A., 2001, MNRAS accepted, astro-ph/0107585

Fraser G.W., 1989, *'X-ray detectors in astronomy'*, Cambridge Univ. Press

Fraser G.W., Ward M.J., Warwick R., Brunton A.N., Cole R.E., Watson M.G., O'Brien P., Priedhorsky W.C., Brumby S., Borozdin K., Vestrand T., White N.E., Jahoda K., Black K., Petre R., Hunter S., Zhang W., Fabian A.C., Nugent K., Peele A., 2000, Lobster-ISS proposal (www.src.le.ac.uk/lobster)

Freeman P.E., Kashyap V., Rosner R., Lamb D.Q., 2002, ApJS, **138**, 185

Galeev A.A., Rosner R., Vaiana G.S., 1979, ApJ, **229**, 318

Gebhardt K., Bender R., Bower G., Dressler A., Faber S.M., Filippenko A.V., Green R., Grillmair C., Ho L.C., Kormendy J., Lauer T.R., Magorrian J., Pinkney J., Richstone D., Tremaine S., 2000, ApJ, **539**, L13

Gehrels N., 1986, ApJ, **303**, 336

Georgantopoulos I., Almaini O., Shanks T., Stewart G.C., Griffiths R.E., Boyle B.J., Gunn K.F., 1999, MNRAS, **305**, 125

George I.M. & Fabian A.C., 1991, MNRAS, **249**, 352

Giacconi R. & Rossi B., 1960, J. Geophys. Res., **65**, 773

Giacconi R., Gursky H., Paolini F., & Rossi B., 1962, Phys.Rev.Lett, **9**, 439

Giacconi R., Rosati P., Tozzi P., Nonino M., Hasinger G., Norman C., Bergeron J., Borgani S., Gilli R., Gilmozzi R., Zheng W., 2001, ApJ, **551**, 624

Giacconi R., Zirm A., Wang J., Rosati P., Nonino M., Tozzi P., Gilli R., Mainieri V., Hasinger G., Kewley L., Bergeron J., Borgani S., Gilmozzi R., Grogin N., Koekemoer A., Schreier E., Zheng W., Norman C., 2002, ApJS accepted, astro-ph/0112184

Gioia I.M., Maccacaro T., Schild R.E., Giommi P., Stocke J.T., 1986, ApJ, **307**, 497

Gonzalez-Solares E., *et al.* 2002, in preparation

Gordon K.D. & Clayton G.C., 1998, ApJ, **500**, 816

Granato G.L. & Danese L., 1994, MNRAS, **268**, 235

Granato G.L., Danese L. & Franceschini A., 1997, ApJ, **486**, 147

Green A.R., McHardy I.M. & Lehto H.J. 1993, MNRAS, **265**, 664

Green P.J., Anderson S.F., Ward M.J., 1992, MNRAS, **254**, 30

Gruber D.E., 1992, proc. *'The X-ray background'*, ed. Barcons X. & Fabian A.C., Cambridge Univ. Press, p44

Gruber D.E., Matteson J.L., Peterson L.E., Jung G.V., 1999, ApJ, **520**, 124

Haas M., Chini R., Meisenheimer K., Stickel M., Lemke D., Klaas U., Kreysa E., 1998, ApJ, **503**, L109

Halpern J., 1982, *Ph.D. thesis*, Harvard Univ.

Hasinger G., 1992, proc. *'The X-ray background'*, ed. Barcons X. & Fabian A.C., Cambridge Univ. Press, p229

Hasinger G., Burg R., Giacconi R., Schmidt M., Trumper J., Zamorani G., 1998, A&A, **329**, 482

Hasinger G., 1998, Astron. Nachr., **319**, 37

Hasinger G., Altieri B., Arnaud M., Barcons X., Bergeron J., Brunner H., Dadina M., Dennerl K., Ferrando P., Finoguenov A., Griffiths R.E., Hashimoto Y., Jansen F.A., Lumb D.H., Mason K.O., Mateos S., McMahon R.G., Miyaji T., Paerels F., Page M.J., Ptak A.F., Sasseen T.P., Schartel N., Szokoly G.P., Trumper J., Turner M., Warwick R.S., Watson M.G., 2001, A&A, **365**, 45

Hauser M.G., Arendt R.G., Kelsall T., Dwek E., Odegard N., Weiland J.L., Freudenreich H.T., Reach W.T., Silverberg R.F., Moseley S.H., Pei Y.C., Lubin P., Mather J.C., Shafer R.A., Smoot G.F., Weiss R., Wilkinson D.T., Wright E.L., 1998, ApJ, **508**, 25

Hornschemeier A.E., Brandt W.N., Garmire G.P., Schneider D.P., Barger A.J., Broos P.S., Cowie L.L., Townsley L.K., Bautz M.W., Burrows D.N., Chartas G., Feigelson E.D., Griffiths R.E., Lumb D., Nousek J.A., Ramsey L.W., Sargent W.L.W., 2001, AJ, **554**, 742

Ivison R.J., Greve T.R., Smail I., Dunlop J.S., Roche N.D., Scott S.E., Page M.J., Stevens J.A., Almaini O., Blain A.W., Willott C.J., Fox M.J., Gilbank D.G., Serjeant S., Hughes D.H., 2002, MNRAS, **337**, 11

Iwasawa K., Fabian A.C., Brandt W.N., Kunieda H., Misaki K., Reynolds C.S. & Terashima Y., 1998, MNRAS, **295**, L20

Iwasawa K., Fabian A.C., Almaini O., Lira P., Lawrence A., Hayashida K. & Inoue H., 2000, MNRAS, **318**, 879

Janesick J.R., 2001, *'Scientific charge-coupled devices'*, SPIE Press

Jentzsch F., 1929, Phys. Z., **30**, 268

Kaastra J.S., Mewe R., Liedahl D.A., Komossa S., & Brinkman A.C., 2000, A&A, **354**, L83

Kaspi S., Brandt W.N., Netzer H., George I.M., Chartas G., Behar E., Sambruna R.M., Garmire G.P., Nousek J.A., 2001, ApJ, **554**, 216

Kembhavi A.K. & Narlika J.V., 1999, *'Quasars and Active Galactic Nuclei: An introduction'*, Cambridge Univ. Press

Kirkpatrick P. & Baez A.V., 1948a, Bull. Am. Phys. Soc., **23**, 10

Kirkpatrick P. & Baez A.V., 1948b, J. Opt. Soc. Am., **38**, 776

Komossa S. & Bohringer H., 1999, A&A, **344**, 755

Koratkar A. & Blaes O., 1999, PASP, **111**, 1

Krolik J.H. & Kriss G.A., 2001, ApJ, **561**, 684

Laor A. & Draine B.T., 1993, ApJ, **402**, 441

Lawrence A. & Elvis M., 1982, ApJ, **256**, 410

Lawrence A., 1991, MNRAS, **252**, 586

Lawrence A. & Papadakis I. 1993, ApJ, **414**, L85

Lawrence A., 1999, proc. *'The AGN/Normal Galaxy Connection'*, 32nd COSPAR Symposium, eds. Schmidt, Kinney & Ho, astro-ph/9902291

Lehmann I., Hasinger G., Schmidt M., Gunn J., Schneider D., Giacconi R., McCaughrean M., Trumper J., Zamorani G., 2000, A&A, **354**, 35

Leighly K.M., 1999, ApJS, **125**, 297

Madejski G.M., Zdziarski A.A., Turner T.J., Done C., Mushotzky R.F., Hartman R.C., Gehrels N., Connors A., Fabian A.C., Nandra K., Celotti A., Rees M.J., Johnson W.N., Grove J.E., Starr C.H., 1995, ApJ, **438**, 672

Magdziarz P., Blaes O., Zdziarski A.A., Johnson, W.N., & Smith D., 1998, MNRAS, **301**, 179

Magorrian J., Tremaine S., Richstone D., Bender R., Bower G., Dressler A., Faber S.M., Gebhardt K., Green R., Grillmair C., Kormendy J., Lauer T., 1998, AJ, **115**, 2285

Maiolino R., Salvati M., Bassani L., Dadina M., della Ceca R., Matt G., Risaliti G., Zamorani G., 1998, A&A, **338**, 781

Maiolino R., Marconi A., Salvati M., Risaliti G., Severgnini P., Oliva E., La Franca F., Vanzi L., 2001, A&A, **365**, 28

Makishima K., 1986, *'The Physics of Accretion onto Compact Objects'*, Springer-Verlag: Berlin, eds. K. Mason, M. Watson, & N. White, p249

Maraschi L. & Haardt F., 1996, proc. *'Accretion Phenomena and Related Outflows'*, eds. D. Wickramasinghe, L. Ferrario & G.Bicknell, astro-ph/9611048

Mathur S., Wilkes B., Elvis M., & Fiore F., 1994, ApJ, **434**, 493

McHardy I.M., Jones L.R., Merrifield M.R., Mason K.O., Newsam A.M., Abraham R.G., Dalton G.B., Carrera F., Smith P.J., Rowan-Robinson M., Abraham R.G., 1998, MNRAS, **295**, 641

McMahon R.G., Priddey R.S., Omont A., Snellen I. & Withington S., 1999, MNRAS, **309**, 1

Miyaji T., Hasinger G., & Schmidt M., 2000, A&A, **353**, 25

Mushotzky R.F., 1980, Adv. Sp. Res., **3**, 10

Mushotzky R.F., Done C., & Pounds K.A., 1993, ARA&A, **31**, 717

Mushotzky R.F., Cowie L.L., Barger A.J., & Arnaud K.A., 2000, Nature, **404**, 459

Nandra K., Pounds K.A., Stewart G.C., George I.M., Hayashida K., Makino F., Ohashi T., 1991, MNRAS, **248**, 760

Nandra K., George I.M., Mushotzky R.F., Turner T.J., Yaqoob T., 1997, ApJ, **476**, 70

Nandra K., Clavel J., Edelson R.A., George I.M., Malkan M.A., Mushotzky R.F., Peterson B.M., Turner T.J., 1998, ApJ, **505**, 594

Neugebauer G., Green R.F., Matthews K., Schmidt M., Soifer B.T., & Bennett J., 1987, ApJS, **63**, 615

Oliver S.J. *et al.* 2000, MNRAS, **316**, 749

Osmer P.S., Porter A.C. & Green R.F., 1994, ApJ, **436**, 678

Page M.J., Stevens J.A., Mittaz J.P.D., Carrera F.J., 2001, Science, **294**, 2516

Papadakis I.E. & Lawrence A., 1993, Nature, **361**, 250

Papadakis I.E. & Lawrence A., 1995, MNRAS, **272**, 161

Peterson B.M., 1997, *'Active Galactic Nuclei'*, Cambridge Univ. Press

Piccinotti G., Mushotzky R.F., Boldt E.A., Holt S.S., Marshall F.E., Serlemitsos P.J., Shafer R.A., 1982, ApJ, **253**, 485

Pier E.A. & Krolik J.H., 1992, ApJ, **401**, 99

Pier E.A. & Krolik J.H., 1993, ApJ, **418**, 673

Pietrini P. & Krolik J., 1995, ApJ, **447**, 526

Pounds K., Nandra K., Stewart G., George I., & Fabian, 1990, Nature, **344**, 132

Pounds K., Edelson R., Markowitz A., Vaughan S., 2001, ApJ, **550**, L15

Pounds K.A. & Reeves J.N., 2002, proc. *'New Visions of the X-ray Universe in the XMM-Newton and Chandra Era'*, ESA SP-488, ed. F. Jansen, astro-ph/0201436

Priedhorsky W.C., Peele A.G., Nugent K.A., 1996, MNRAS, **279**, 733

Ptak A., Yaqoob T., Mushotzky R., Serlemitsos P., Griffiths R., 1998, ApJ, **501**, L37

Rothschild R.E., Mushotzky R.F., Baity W.A., Gruber D.E., Matteson J.L., & Peterson L.E., 1983, ApJ, **269**, 423

Rowan-Robinson M., 1977, ApJ, **213**, 635

Rowan-Robinson M., 1995, MNRAS, **272**, 737

Rowan-Robinson M., 2001, NewAR, **377**, 631

Sanders D.B., Phinney E.S., Neugebauer G., Soifer B.T., & Matthews K., 1989, ApJ, **347**, 29

Schlickeiser R., Biermann P.L., & Crusius-Watzel A., 1991, A&A, **247**, 283

Schmidt M. & Green R.F., 1983, ApJ, **269**, 352

Schmidt M., Schneider D.P. & Gunn J.E., 1995, AJ, **110**, 68

Schmidt M., Hasinger G., Gunn J., Schneider D., Burg R., Giacconi R., Lehmann I., MacKenty J., Trumper J., Zamorani G., 1998, A&A, **329**, 495

Schmidt W.K.H., 1975, Nucl. Instrum. Meth., **127**, 285

Schneider D.P., Schmidt M., Gunn J.E., 1989, AJ, **98**, 1507

Scott S., Fox M., Dunlop J., Serjeant S., Peacock J., Ivison R., Oliver S., Mann R., Lawrence A., Efstathiou A., Rowan-Robinson M., Hughes D., Archibald E., Blain A., Longair M., 2001, MNRAS submitted, astro-ph/0107446

Serjeant S., Oliver S., Rowan-Robinson M., Crockett H., Missoulis V., Sumner T., Gruppioni C., Mann R.G., Eaton N., Elbaz D., Clements D.L., Baker A., Efstathiou A., Cesarsky C., Danese L., Franceschini A., Genzel R., Lawrence A., Lemke D., McMahon R.G., Miley G., Puget J.-L., Rocca-Volmerange B., 2000, MNRAS, **316**, 768

Setti G., 1992, *'X-ray emission from Active Galactic Nuclei and the Cosmic X-ray Background'*, eds. W. Brinkmann & J. Trumper, MPE Report 235, 414

Shanks T., Georgantopoulos I., Stewart G.C., Pounds K.A., Boyle B.J. & Griffiths R.E., 1991, Nature, **353**, 315

Silk J. & Rees M.J., 1998, A&A, **331**, L1

Simpson C.J., 1994, *Ph.D. thesis*, Oxford Univ.

Simpson C., Ward M. & Kotilainen J., 1994, MNRAS, **271**, 250

Simpson C., 1998, ApJ, **509**, 653

Soltan A., 1982, MNRAS, **200**, 115

Stern D., Moran E.C., Coil A.L., Connolly A., Davis M., Dawson S., Dey A., Eisenhardt P., Elston R., Graham J.R., Harrison F., Helfand D.J., Holden B., Mao P., Rosati P., Spinrad H., Stanford S.A., Tozzi P., Wu K.L., 2002, ApJ, **568**, 71

Tagliaferri G., Bao G., Israel G.L., Stella L., Treves A., 1996, ApJ, **465**, 181

Tozzi P., Rosati P., Nonino M., Bergeron J., Borgani S., Gilli R., Gilmozzi R., Hasinger G., Grogin N., Kewley L., Koekemoer A., Norman C., Schreier E., Szokoly G., Wang J.X., Zheng W., Zirm A., Giacconi R., 2001, ApJ, **562**, 42

Tripp T.M., Bechtold J. & Green R.F., 1994, ApJ, **433**, 533

Turner T.J., 1988, *Ph.D. thesis*, Leicester Univ.

Turner T.J., Weaver K.A., Mushotzky R.F., Holt S.S., & Madejski G.M., 1991, ApJ, **381**, 85

Ueda Y., Takahashi T., Inoue H., Tsuru T., Sakano M., Ishisaki Y., Ogasaka Y., Makishima K., Yamada T., Akiyama M., Ohta K., 1999, ApJ, **518**, 656

Ulrich M.H., 1989, A&A, **220**, 71

Ulrich M.H., Maraschi L., Urry C.M., 1997, ARA&A, **35**, 445

Underwood J.H., Milligan J.E., de Loach A.C., & Hoover R.C., 1977, Appl.Optics, **16**, 858

Vaiana G.S., Van Speybroeck L.P., Zombeck M.V., Krieger A.S., Silk J.K., & Timothy A.F., 1977, Space Sci. Instrum., **3**, 19

Vanden Berk D.E., *et al.* 2001, AJ, **122**, 549

Vecchi A., Molendi S., Guainazzi M., Fiore F., & Parmer A.N., 1999, A&A, **349**, L73

Veron-Cetty M.-P., Veron P., 1993, *ESO Scientific Report No.* 13

Veron-Cetty M.-P., Veron P., 2000, *ESO Scientific Report No.* 19

von Laue M., 1912, Proc. Bavarian Academy of Sciences

Walter R. & Fink H.H., 1993, A&A, **274**, 105

Wandel A., Peterson B.M., & Malkan M.A., 1999, ApJ, **526**, 579

Ward M.J., Elvis M., Fabbiano G., Carleton N.P., Willner S.P., Lawrence A., 1987, ApJ, **315**, 74

Warwick R.S., Smith D.A., Yaqoob T., Edelson R., Johnson W.N., 1996, ApJ, **470**, 349

Weedman D.W., 1985, ApJS, **57**, 523

Wilkes B.J., Hooper E.J., Mcleod K.K., Elvis M.S., Impey C.D., Lonsdale C.J., Malkan M.A., McDowell J.C., 1999, proc. *'The Universe as Seen by ISO'*, ed. M. Kessler, astro-ph/9902084

Wilkes B.J., 2001, NewAR, **45**, 641

Wolter H., 1952a, Ann. Phys. NY, **10**, 94

Wolter H., 1952b, Ann. Phys. NY, **10**, 286

Wright E.L., Mather J.C., Fixsen D.J., Kogut A., Shafer R.A., Bennett C.L., Boggess N.W., Cheng E.S., Silverberg R.F., Smoot G.F., Weiss R., 1994, ApJ, **420**, 450

Zamorani G., Mignoli M., Hasinger G., Burg R., Giacconi R., Schmidt M., Trumper J., Ciliegi P., Gruppioni C., Marano B., 1999, A&A, **346**, 731

Zdziarski A.A., Ghisellini G., George I.M., Svensson R., Fabian A.C., & Done C., 1990, ApJ, **363**, L1

Zdziarski A.A. & Coppi P., 1991, ApJ, **376**, 480

Zheng W., Kriss G.A., Telfer R.C., Grimes J.P., & Davidsen A.F., 1997, ApJ, **475**, 469